



Technical University of Munich
Department of Physics
Experimental Physics with Cosmic Particles

Master Thesis

**Optical Characterization of the Deep Pacific
Ocean: Development of an Optical Sensor
Array for a Future Neutrino Telescope**

Felix Henningsen

July 19, 2018

Matriculation No.: 03638473

Supervisor: Prof. Elisa Resconi
Second Assessor: Prof. Susanne Mertens

Multi-messenger astronomy combines the observation of astrophysical objects and processes via photons, cosmic rays, neutrinos and gravitational waves. Its ultimate task is to deduce complimentary pictures of the mechanisms and sources responsible for the highest energetic particles observed today. Especially the field of neutrino astronomy has made significant advances over the recent years and provides grounds for the exploration of potential new sites for neutrino telescopes.

This thesis will describe a newly developed optical sensor array which will enable the assessment of a deep-sea site in the Northern Pacific for its feasibility to host a new large-scale neutrino telescope. This *Strings for Absorption length in Water* (STRAW) detector will make use of a specific geometry hosting an array of light flashers and sensors to quantify optical properties of the deep-sea water at a depth of 2.6km in the *Cascadia Basin*, located several hundred miles off the shore of Vancouver Island in Canada. The primary focus of this experiment will be the characterization of absorption and scattering properties as well as background radiation from radioactivity and bioluminescence in the deep sea.

After an introduction to neutrino physics and neutrino astronomy, the scientific objectives of STRAW are outlined. Based on the latter, the spectral range of investigation and a detector geometry were defined which achieve feasible detector performance with expected water conditions. In the process, the optimization, calibration and characteristics of the instrumentation were investigated. The *Precision Optical Calibration Module* (POCAM) will act as the light emitter and was verified to show a very promising grade of isotropy of only a few percent deviation with significant light emission at nanosecond pulse widths. The newly developed *STRAW Digital Optical Module* (sDOM) will not only detect the POCAM flashes and thus is able to access the inherent properties of the sea water, but furthermore was calibrated in order to characterize present background radiation. Eventually, the deep-sea structure of the detector will be presented and the thesis will close with the successful deep-sea deployment of the detector and preliminary measurements of the very first operation.

Abstract	iii
Contents	vii
List of Figures	ix
List of Tables	xi
Acknowledgments	xiii
I Scientific Introduction	1
<hr/>	
1 Neutrino Physics	3
1.1 The Standard Model	3
1.1.1 Neutrino History	4
1.1.2 Beyond the Standard Model	4
1.2 Weak Interaction	4
1.2.1 Charged and Neutral Currents	5
1.2.2 Electroweak Theory	6
1.3 Neutrino Oscillation	6
1.3.1 In Vacuum	7
1.3.2 Matter Effects	8
1.3.3 Neutrino Mass Hierarchy	10
1.4 The Neutrino Universe	11
1.4.1 Solar Neutrinos	11
1.4.2 Supernova Neutrinos	11
1.4.3 Atmospheric Neutrinos	12
1.4.4 Cosmogenic Neutrinos	14
1.4.5 Relic Neutrinos	14
2 Large Scale Neutrino Telescopes	15
2.1 High-Energy Neutrino Detection	15
2.1.1 Neutrino Interactions	15
2.1.2 The Cherenkov Effect	15
2.1.3 Detector Principles	16
2.1.4 Neutrino Signatures	17
2.2 Active Neutrino Telescopes	18
2.2.1 Pioneer Experiments	18
2.2.2 IceCube	19
2.2.3 Baikal GVD	20
2.2.4 KM3NeT	20
2.3 Future Prospect of Neutrino Astronomy	21

3	STRAW Concept	25
3.1	Experimental Objectives	25
3.1.1	Absorption- & Scattering Length	25
3.1.2	Light Background	26
3.2	Optical Prerequisites	26
3.2.1	Cherenkov Spectrum	27
3.2.2	Sea Water	27
3.2.3	Module Characteristics	28
3.3	Detector Geometry	29
4	Precision Optical Calibration Module	33
4.1	Design	33
4.1.1	Concept	33
4.1.2	Housing	34
4.1.3	Flasher Circuit	34
4.1.4	Integrating Sphere	35
4.1.5	Photosensors	37
4.1.6	Electronics	37
4.1.7	Internal Mounting	37
4.2	Prototype in Baikal	38
4.3	Light Emission Characteristics in STRAW	39
4.3.1	Flasher Circuit Configuration	39
4.3.2	LED Selection	40
4.3.3	Light Pulse	42
4.3.4	Isotropy	45
4.3.5	In-situ Calibration	49
4.4	Summary	52
5	STRAW Digital Optical Module	53
5.1	Design	53
5.1.1	Concept	53
5.1.2	Housing	53
5.1.3	Photosensor	54
5.1.4	Optical Gel	54
5.1.5	Read-Out Electronics	55
5.1.6	Internal Mounting & Heat Dissipation	55
5.2	Light Detection Characteristics in STRAW	56
5.2.1	PMT Characterization	56
5.2.2	Optical Properties	60
5.2.3	TDC Read-Out	60
5.3	Summary	61
6	The STRAW Detector	63
6.1	Deep-Sea Infrastructure	63
6.2	Qualification & On-site Testing	64
6.3	Deployment	65
6.4	First Light	66

III Summary & Conclusions	69
<hr/>	
7 Summary & Conclusions	71
IV Appendix	73
<hr/>	
A STRAW	75
A.1 SiPM Response	75
B POCAM	77
B.1 sDOM in Test Tank	77
C sDOM	79
C.1 Complete STRAW Detector Concept	79
C.2 Deployment	80
C.3 ROV Inspection	81
Bibliography	88

List of Figures

1.1	Graphical depiction of the Standard Model of particle physics.	4
1.2	Examples for charged and neutral current processes of the weak interaction. . .	5
1.3	All-particle energy spectrum of high-energy cosmic rays from various experiments.	12
1.4	Cosmic neutrino fluxes as a function of energy.	14
2.1	Qualitative summary of the Cherenkov effect.	16
2.2	High-energy neutrino signatures in the IceCube detector.	18
2.3	The IceCube detector and its photosensor module.	19
2.4	GVD Detector concept.	20
2.5	KM3NeT layout and its new photosensor.	20
2.6	Cascadia Basin location.	21
3.1	Example of a bioluminescent organism.	26
3.2	Number of emitted Cherenkov photons per travelled distance.	27
3.3	Spectral transmission of sea water according to Smith and Baker [108].	28
3.4	Spectral properties of the STRAW detector.	29
3.5	Geometry illustration of the STRAW detector.	30
3.6	Photon number estimate of the STRAW detector geometry.	31
4.1	Timeline of the POCAM design evolution.	33
4.2	Current POCAM design.	34
4.3	Kapustinsky flasher schematic.	35
4.4	Prototype LED layout.	35
4.5	Integrating sphere geometry.	36
4.6	Internal mounting, shadow and photosensors.	37
4.7	POCAM prototype in GVD	38
4.8	Exemplary Kapustinsky behavior with different capacities C and inductances L .	39
4.9	Selection measurements of possible POCAM LEDs for STRAW.	41
4.10	STRAW flasher LED layout.	41
4.11	Photodiode response to a picosecond laser pulse.	42
4.12	Pulse shapes of POCAM LEDs.	43
4.13	Full width half maxima of the POCAM LED flashes.	44
4.14	Frequency stability of the POCAM flasher.	45
4.15	Isotropy scan coordinate system.	46
4.16	Point source validation measurement.	46
4.17	Isotropy scan coordinate system.	47
4.18	Isotropy scan of a POCAM integrating sphere.	47
4.19	Polar isotropy of the integrating sphere.	48
4.20	Integrating sphere light emission visualized in 3D.	48
4.21	Preliminary POCAM hemisphere emission profile in air.	49
4.22	Exemplary output of the internal POCAM photosensors.	49
4.23	Amplitude extraction from internal SiPM signals.	50
4.24	Exemplary POCAM calibration plot.	51

4.25	Long exposure of an illuminated POCAM hemisphere.	52
4.26	Finished POCAM module for STRAW.	52
5.1	The sDOM design.	53
5.2	sDOM PMT and its high-voltage base.	54
5.3	Concept of the TDC sampling of a PMT pulse.	55
5.4	The internal sDOM mounting design.	55
5.5	Exemplary linearity measurement of an sDOM PMT.	56
5.6	Exemplary single-photon amplitude spectrum of an sDOM PMT.	57
5.7	Exemplary Δt histogram of peak-detected noise pulses from an sDOM PMT.	58
5.8	Exemplary $\log_{10}(\Delta t)$ histogram of an sDOM PMT at 25°C.	59
5.9	Exemplary sDOM PMT dark rate dependence on temperature and voltage.	59
5.10	Optical properties of sDOM components.	60
5.11	Preliminary TDC read-out of an sDOM PMT.	60
5.12	Early sDOM hemisphere assembly prototype.	61
5.13	sDOM instruments prior to shipment to Canada.	61
6.1	Mechanical concept of the STRAW strings.	63
6.2	Spooling system of a STRAW string.	64
6.3	STRAW assembly submerged in ONC test tank.	65
6.4	STRAW string during deployment.	65
6.5	ROV view of an sDOM on a STRAW string in 2625m depth.	66
6.6	STRAW first light.	67
B.1	sDOM being submerged in the test tank.	77
C.1	Complete STRAW detector concept.	79
C.2	On-deck unspooling of a STRAW string.	80
C.3	On-deck mJB mounting to a STRAW string.	80
C.4	ROV inspection: POCAM.	81
C.5	ROV inspection: sDOM.	81
C.6	ROV inspection: mini junction box.	82
C.7	ROV rotating anchor.	82

List of Tables

1.1	Summary of the fundamental forces in the Standard Model of particle physics. . .	3
1.2	Current best-fit parameters of the weak mixing properties.	11
4.1	Final selection of POCAM LEDs for STRAW.	42

Acknowledgments

The project of designing, building and eventually deploying the STRAW detector was by far one of the most crazy but rewarding projects in my scientific life. I want to take this opportunity to thank everyone on the team: First and foremost my professor, Elisa Resconi, for creating and enabling a warm and familiar atmosphere in the group even during the most exhausting times. It is her vision of scientific progress that enables impactful projects like STRAW and makes the group thrive in the process. Evenly, I want to thank the team members of STRAW for their dedication, patience, endurance and professionalism during this project, that is, M. Boehmer, R. Gernhäuser, L. Papp, C. Fruck, I.C. Rea, A. Gärtner, C. Spannfellner, K. Holzapfel and S. Hiller as well as K. Leissmüller – without them, none of this would have been possible.

Secondly, I want to speak out my gratitude to the team of Ocean Networks Canada. Led by A. Round and B. Pirenne, their teams have supported us with invaluable deep-sea, database and engineering expertise as well as hospitality during our visits. They eventually successfully deployed and connected the STRAW deep-sea detector and it was this crucial step that eventually made it succeed.

Lastly, I want to be grateful for my family, my loving girlfriend and my friends who have been supporting me from the start of my studies and were understanding during the exhausting and time-expensive months of the STRAW project. Without them I would not be who I am today.

– Felix Henningsen

I

Scientific Introduction

I have done a terrible thing, I have postulated a particle that cannot be detected.

Wolfgang Pauli, [41]

1

The goal of *neutrino telescopes* is to make use of neutrinos as messenger particles for astrophysical observations despite of their low interaction rate in matter at high energies. Before introducing the scale and conditions necessary for their successful operation, theoretical aspects of neutrino theory will be outlined in this chapter. Commencing with a description of neutrinos in the Standard Model, it will further introduce neutrino oscillations, matter effects and the mass hierarchy, before closing with a brief summary of neutrino sources in the universe.

1.1 The Standard Model

The Standard Model (SM) of particle physics is the theoretical framework of elementary particles and their interactions. It combines the three known generations of fermions with the five gauge bosons mediating the strong, weak and electromagnetic force as well as the Higgs boson, which is responsible for generating mass. The gravitational force is not included.

In gauge symmetries it is usually expressed as

$$G_{\text{SM}} = \text{SU}(3) \times \text{SU}(2) \times \text{U}(1) \quad (1.1)$$

with the strong, weak and electromagnetic symmetry group respectively.

Each particle generation of the SM hosts a pair of quarks and leptons. While all the quarks carry electric charge, among leptons, only the electron (e^\pm), the muon (μ^\pm) and the tau (τ^\pm) do. The corresponding neutrinos (ν_e, ν_μ, ν_τ) are neutral spin 1/2 particles and carry neither electric nor color charge. Each particle further has a corresponding anti-particle in the SM.

The mediators of interactions are the gluon (strong), the massive Z^0 and W^\pm (weak) and the photon (electromagnetic). Whereas the electromagnetic interaction couples to electric and the strong to color charge, the weak interaction couples to the flavor of particles. The name weak originates in the strong suppression caused by its massive gauge bosons which makes it orders of magnitude weaker than its counterparts. A qualitative summary of the fundamental forces is given in table 1.1, an illustration of the SM in fig. 1.1.

Interaction	Mediator	Mass (GeV/c ²)	Charge Source	Affected Fermions	Effective Range (m)	Coupling Strength
strong	8 Gluons (g)	0	color	q	10^{-15}	~ 1
electrom.	γ	0	charge	q, e, μ, τ	∞	$\sim 1/137$
weak	W^\pm, Z^0	$\sim 80, 91$	flavor	q, e, μ, τ, ν	10^{-18}	$\sim 10^{-5}$

Table 1.1: Summary of the fundamental forces in the Standard Model of particle physics. Listed are selected characteristics of the strong, weak and electromagnetic force. [115, p. 576]

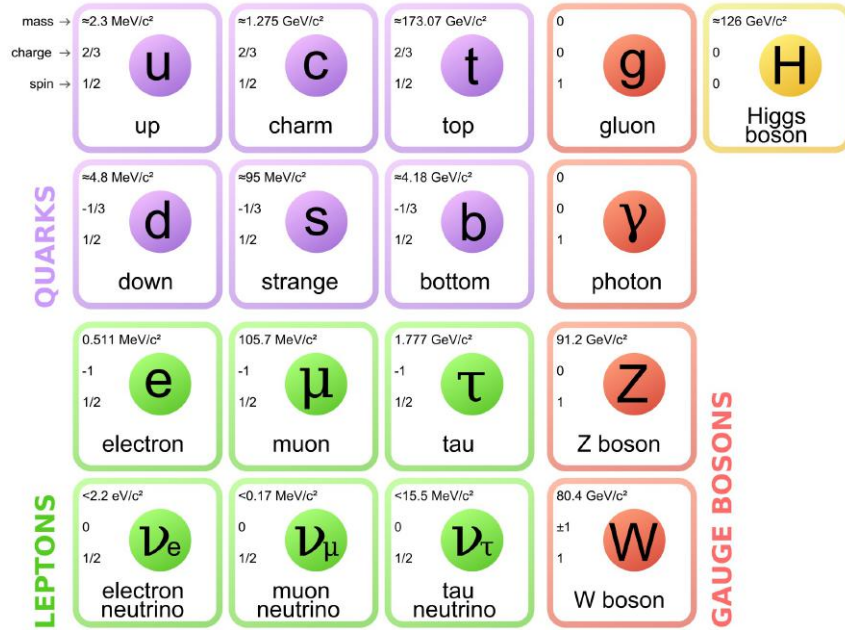


Figure 1.1: Graphical depiction of the Standard Model of particle physics. Shown are quarks (purple), leptons (green), gauge bosons (red) and the Higgs boson (yellow). In addition, every constituent's mass, charge and spin is noted. Figure taken from [57].

1.1.1 Neutrino History

After the postulation of the neutrino by Wolfgang Pauli in 1930 in order to explain the puzzling observation of a continuous spectrum of β -decay electrons, it was not until 1956 that the electron anti-neutrino ($\bar{\nu}_e$) was experimentally observed by Cowan and Reines. Six years later, the rumors of a second neutrino flavor were confirmed by Schwartz, Lederman and Steinberger with experimental evidence for the muon neutrino (ν_μ). [46] After the observation of the tau lepton in 1975 [95] and more than two decades of research later, the tau neutrino (ν_τ) was finally discovered by the *DONUT* experiment in 2000 [79].

1.1.2 Beyond the Standard Model

Even though the Standard Model has been the successful and accurate theoretical backbone of a large number of scientific fields in particle physics, observations of the more recent past have shown that it is still incomplete [116]. Among these missing aspects, the observation of, both solar and atmospheric, neutrino oscillations [19, 30] has proven that neutrinos have a non-zero mass that is not accounted for in the SM.

It remains the major objective of theoretical physics in the twenty-first century to formulate a unified theory that incorporates all fundamental forces and observations into what is often called a *grand unified theory* [e.g. 101].

1.2 Weak Interaction

The weak interaction is one of the four known, fundamental forces in elementary particle physics. It is mediated through very massive gauge bosons, namely the W^\pm and the Z^0 with masses of $80.385 \pm 0.015 \text{ GeV}/c^2$ and $91.188 \pm 0.002 \text{ GeV}/c^2$ respectively [94]. These massive bosons cause a strong suppression in comparison to its electromagnetic or strong analogues.

However, albeit it being strongly suppressed, the weak interaction takes a unique role as it couples to a particle's flavor and hence allows for interactions containing all fermionic members of the Standard Model. Furthermore, the weak force plays the key role in β -decays and provides the only known interaction channel for neutrinos.

1.2.1 Charged and Neutral Currents

Weak processes are most commonly categorized by the mediating gauge bosons. Interactions involving the mediation of a W^\pm boson are denoted *charged currents* (CC), interactions involving the exchange of a Z^0 boson are called *neutral currents* (NC). Depending on the fermions involved, they are sometimes further divided into leptonic, semi-leptonic and hadronic processes. Exemplary weak interactions are illustrated in fig. 1.2 using the corresponding Feynman diagrams.

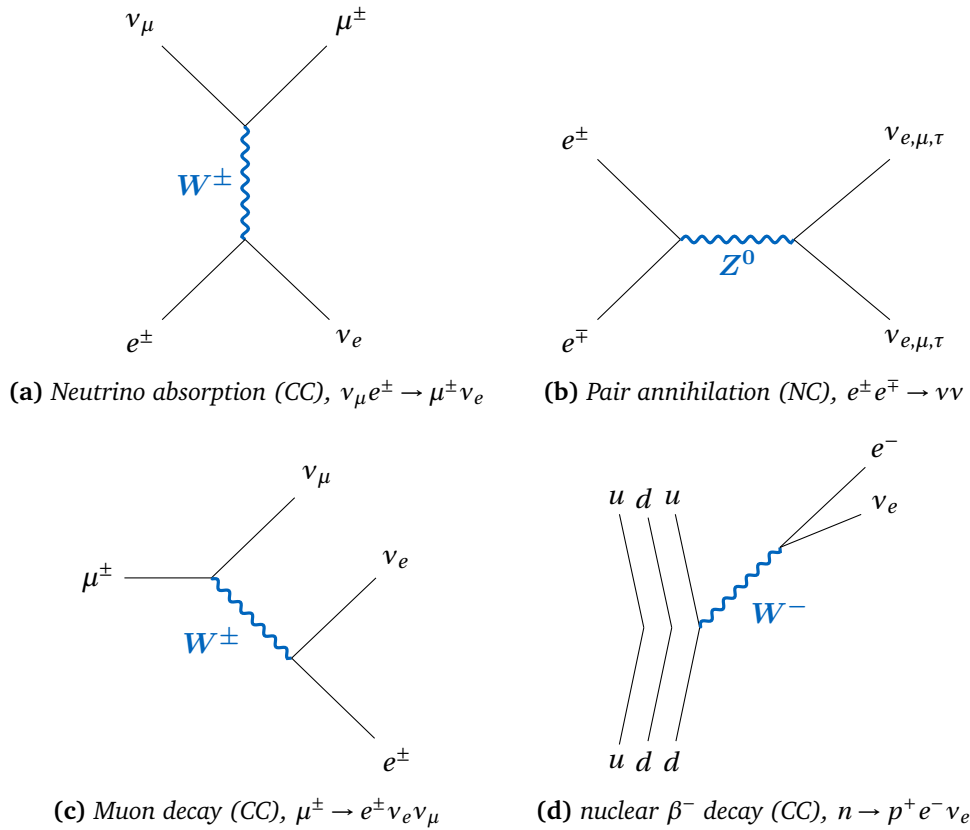


Figure 1.2: Examples for charged and neutral current processes of the weak interaction.

For a specific flavor α , the respective Lagrangians for charged and neutral leptonic weak interactions are proportional to

$$-\mathcal{L}_{\text{CC}} \sim g \cdot \left(W_\mu^+ \bar{\nu}_\alpha \gamma^\mu (1 - \gamma^5) l_\alpha^- \right) + \text{h.c.} \quad (1.2)$$

$$-\mathcal{L}_{\text{NC}} \sim \frac{g}{\cos(\theta_W)} \cdot \left(\frac{1}{2} \bar{f}_\alpha \gamma^\mu (1 - \gamma^5) f_\alpha + \sin^2(\theta_W) \left(\bar{l}_\alpha \gamma^\mu l_\alpha \right) \right) Z_\mu \quad (1.3)$$

with the weak coupling constant g , Weinberg angle θ_W , gamma matrices γ^μ , $\gamma^5 = i\gamma^0\gamma^1\gamma^2\gamma^3$, fermion-, neutrino- and lepton fields f , ν and l as well as the weak boson fields W_μ^\pm and Z_μ .

In eqs. (1.2) and (1.3) it is apparent that neutral currents interact with both left- and right-handed fermions, while charged currents only interact with left-handed ones.¹ All of which holds with reversed chiralities for anti-particles. The consequence is *charge conjugation* (C) and *parity* (P) *violation* for both, charged and neutral current processes. While P -violation was experimentally confirmed as early as 1957 by the well-known Wu Experiment [122], it was further observed in the decay of kaons that also CP is violated [94].

The suppression in comparison to the strong and electromagnetic processes results from the fact that the non-zero mass term of the mediating bosons enters in the denominator of the propagator. In the end, this notably suppresses their cross sections via *Fermi's golden rule*

$$\sigma_{i \rightarrow f} \sim |\mathcal{M}_{fi}|^2 \sim \left(\frac{g}{|q|^2 + M_{Z,W}^2} \right)^2 \quad (1.4)$$

and hence also the interaction rates. All of which makes the experimental observation of weak processes so challenging.

1.2.2 Electroweak Theory

Contrary to the strong force and the associated *quantum chromodynamics*, the weak interaction is best understood theoretically when combined with the electromagnetic force, forming the so called *electroweak force*. For this combined theory of two fundamental forces, Glashow, Weinberg and Salam were awarded the nobel prize in physics 1979 for their contributions.

While the detailed theory shall not be discussed here, it should be noted that the theoretical unification of the $SU(2)_W$ and $U(1)_Y$ gauge groups, in combination with the Higgs mechanism and the requirement of gauge invariance, naturally results in three massive gauge bosons (identified with the W^\pm and the Z^0) and the massless photon. Predictions of this theory also match remarkably well with experimental observations. [96, 99]

The simplified background of the electroweak formalism is the postulated conservation of the third component of the *weak isospin* T . This quantum number, identified with the weak force, now justifies the notation of doublets and singlets as a basis of its associated $SU(2)$ symmetry. Left-handed leptons carry $T = 1/2$ and form a weak doublet with $T_3 = \pm 1/2$ for neutrinos and charged leptons, respectively; right-handed leptons form a singlet and carry $T = T_3 = 0$.

The existence of neutral and charged currents requires the mediating gauge bosons to form a triplet under the weak isospin. All of them carry $T = 1$, while the third component is $T_3 = \pm 1$ for W^\pm and $T_3 = 0$ for Z^0 .

1.3 Neutrino Oscillation

In weak interactions, neutrinos are identified by the corresponding *flavor eigenstates*, however, their propagation is governed by the Hamiltonian and hence by *mass eigenstates*. Neutrino oscillations emerge since mass eigenstates are a composition of flavor eigenstates and transitions of one flavor into another can occur during propagation – a process which would obviously violate lepton number conservation.

In the Standard Model, neutrinos are massless due to the exclusion of right-handed neutrinos, without which, no Dirac mass term can be formed. While the observation of neutrino oscillations [19, 30] has proven that neutrinos have a non-zero mass, as of today, the exact mechanism generating these masses is not well understood.

¹The operator $P_L = \frac{1-\gamma^5}{2}$ projects out the left-handed component of a spinor field, i.e. $P_L \phi = \phi_L$

So far, both terrestrial and cosmological experiments, probing the scale of neutrino masses, were only able to set upper limits [82, 92]. However, they have been found to be orders of magnitude lighter than corresponding charged leptons or quarks. For instance, the current electron neutrino mass upper limit reads $m_{\nu_e} < 2 \text{ eV}$ [94]. Theoretical explanation attempts, of this mass and its seemingly unnatural smallness require physics beyond the Standard Model [58].

1.3.1 In Vacuum

Starting with a weakly produced neutrino ν_α of flavor α in vacuum, generally the flavor and mass eigenstates will be related by a unitary transformation

$$|\nu_\alpha\rangle = \sum_k U_{\alpha k} |\nu_k\rangle \quad (1.5)$$

$$|\nu_k\rangle = \sum_\alpha U_{\alpha k}^* |\nu_\alpha\rangle \quad (1.6)$$

which is commonly called the *Pontecorvo-Maki-Nakagawa-Sakata (PMNS) matrix* [84, 100].

In the three-generation picture, it is 3×3 and commonly parametrized by three mixing angles and a complex phase

$$U = \begin{pmatrix} 1 & 0 & 0 \\ 0 & c_{23} & s_{23} \\ 0 & -s_{23} & c_{23} \end{pmatrix} \begin{pmatrix} c_{13} & 0 & s_{13}e^{-i\delta} \\ 0 & 1 & 0 \\ -s_{13}e^{-i\delta} & 0 & c_{13} \end{pmatrix} \begin{pmatrix} c_{12} & s_{12} & 0 \\ -s_{12} & c_{12} & 0 \\ 0 & 0 & 1 \end{pmatrix} \quad (1.7)$$

with the sine and cosine of the *weak mixing angle* θ_{ij} , represented by s_{ij} and c_{ij} respectively, and the *CP violating phase* δ . Furthermore, if neutrinos are Majorana fermions, that is, their own anti-particles, two additional complex phases, usually denoted α_1 and α_2 , are introduced but remain irrelevant in the scope of vacuum neutrino oscillations. [58, 94]

Should experiments show that unitarity of this matrix does not hold in the scope of three generations, physics beyond the Standard Model would be indicated. A possible, minimal extension is the postulation of right-handed neutrinos that do not interact weakly and consequently are called *sterile neutrinos* [48].

However, the neutrino mass eigenstate propagation in vacuum is described by its Hamiltonian $H = H_0$ and the *time-dependent Schrödinger equation*

$$i\hbar \frac{\partial}{\partial t} |\nu_k(t)\rangle = H_0 |\nu_k\rangle \quad \text{and} \quad |\nu_k\rangle := |\nu_k(t=0)\rangle \quad (1.8)$$

which is a common, quantum mechanical differential equation and solved by

$$|\nu_k(t)\rangle = e^{-\frac{i}{\hbar} E_k t} |\nu_k\rangle \quad (1.9)$$

in which the neutrino masses m_k enter via the energy-momentum relation

$$E_k = \sqrt{p_k^2 c^2 + m_k^2 c^4} \quad (1.10)$$

Now, using the Taylor expansion

$$\sqrt{1+x} = 1 + \frac{x}{2} + \mathcal{O}(x^2) \quad (1.11)$$

and assuming that the neutrino was produced with a total energy E much larger than the neutrino mass, i.e. $E \gg m_k$, then eq. (1.10) can be well approximated by

$$E_k \approx E + \phi_k \quad \text{and} \quad \phi_k := \frac{m_k^2 c^4}{2E} \quad (1.12)$$

This yields the additional, mass-dependent phase ϕ_k in eq. (1.9)

$$|\nu_k(t)\rangle = e^{-\frac{i}{\hbar}pct} e^{-\frac{i}{\hbar}\phi_k t} |\nu_k\rangle \quad (1.13)$$

Consequently, transforming eq. (1.13) to flavor basis using eq. (1.5)

$$\begin{aligned} |\nu_\alpha(t)\rangle &= \sum_k U_{\alpha k} |\nu_k(t)\rangle \\ &= e^{-\frac{i}{\hbar}pct} \sum_k U_{\alpha k} e^{-\frac{i}{\hbar}\phi_k t} |\nu_k\rangle \end{aligned} \quad (1.14)$$

and the orthogonality of eigenstates

$$\langle \nu_j | \nu_k \rangle = \delta_{jk} \quad (1.15)$$

allows formulating the transition amplitude of flavor $\alpha \rightarrow \beta$, after time t , as

$$\begin{aligned} \langle \nu_\beta(t) | \nu_\alpha \rangle &= e^{\frac{i}{\hbar}pct} \sum_{j,k} U_{\beta j}^* U_{\alpha k} e^{\frac{i}{\hbar}\phi_j t} \langle \nu_j | \nu_k \rangle \\ &= e^{\frac{i}{\hbar}pct} \sum_k U_{\beta k}^* U_{\alpha k} e^{\frac{i}{\hbar}\phi_k t} \end{aligned} \quad (1.16)$$

Finally, eq. (1.16) allows the determination of the transition probability of $\nu_\alpha \rightarrow \nu_\beta$, after a travelled distance of $L = ct$, as [58, p. 154]

$$\begin{aligned} P_{\alpha \rightarrow \beta} &= |\langle \nu_\beta(t) | \nu_\alpha \rangle|^2 \\ &= \delta_{\alpha\beta} \\ &\quad - 4 \sum_{i>j} \Re \left(U_{\beta j}^* U_{\alpha j} U_{\beta i} U_{\alpha i}^* \right) \sin^2 \left(\frac{\Delta m_{ij}^2 L}{4E} \right) \\ &\quad + 2 \sum_{i>j} \Im \left(U_{\beta j}^* U_{\alpha j} U_{\beta i} U_{\alpha i}^* \right) \sin \left(\frac{\Delta m_{ij}^2 L}{2E} \right) \end{aligned} \quad (1.17)$$

with $\hbar = c = 1$ and $\Delta m_{ij}^2 \equiv m_i^2 - m_j^2$, the squared mass differences of neutrino mass eigenstates.

Now, eq. (1.17) makes it apparent, if the masses of the neutrino mass eigenstates are non-zero and unequal, the oscillatory terms give rise to probabilities of observing a different neutrino flavor after propagation, with respect to the one that was produced. The mass-dependent phase ϕ_k influences the frequencies of the propagating neutrino mass eigenstates. With unequal masses, different frequencies lead to changes of the flavor composition during propagation. This is called *neutrino oscillation*.

In contrast to the strong *CKM mixing*, experimental observations suggest that neutrino mixing is not small [94]. The current best-fit values of the weak mixing properties are included in table 1.2.

1.3.2 Matter Effects

So far, only the vacuum oscillations have been outlined theoretically and the question remains, if matter can effectively change the oscillation behavior of neutrinos. The major effects will be outlined using the qualitative, theoretical aspects of matter oscillations.

Theoretical Background

With respect to vacuum, the propagation through matter is governed by an altered Hamiltonian

$$H = H_0 + V \quad (1.18)$$

in which the potential is caused by the presence of electrons in matter.

In contrast to the neutral currents which are present for all flavors, these electrons provide a charged current scattering channel for the electron flavor fraction of the propagating mass eigenstates and hence affect their propagation. The effective potential in matter becomes

$$V = V_e - V_x = \sqrt{2} G_F n_e \quad (1.19)$$

with the *Fermi coupling constant* G_F , the electron number density in the medium n_e and the flavors without charged current channel in matter $x = \{\mu, \tau\}$ [107].

Most importantly, it will change the equation of motion eq. (1.8) for neutrino mass eigenstates. In flavor basis, this will lead to the non-trivial differential equation [21]

$$i \frac{\partial}{\partial t} \begin{pmatrix} \nu_e \\ \nu_\mu \\ \nu_\tau \end{pmatrix} = \left[\frac{1}{2E} U \begin{pmatrix} m_1^2 & 0 & 0 \\ 0 & m_2^2 & 0 \\ 0 & 0 & m_3^2 \end{pmatrix} U^\dagger + \begin{pmatrix} V & 0 & 0 \\ 0 & 0 & 0 \\ 0 & 0 & 0 \end{pmatrix} \right] \begin{pmatrix} \nu_e \\ \nu_\mu \\ \nu_\tau \end{pmatrix} \quad (1.20)$$

the detailed treatment of which, would exceed the scope of this work.

Instead, a two-flavor approximation is sufficient to extract the major, qualitative effects of matter on neutrino oscillations. Here, the vacuum mixing parameters will be replaced by their matter analogues, $\theta \rightarrow \theta_m$ and $\Delta m^2 \rightarrow \Delta m_m^2$, via diagonalizing the effective¹ Hamiltonian of the equation of motion

$$i \frac{\partial}{\partial t} \begin{pmatrix} \nu_e \\ \nu_x \end{pmatrix} = \begin{pmatrix} -\frac{\Delta m^2}{4E} \cos(2\theta) + V & \frac{\Delta m^2}{4E} \sin(2\theta) \\ \frac{\Delta m^2}{4E} \sin(2\theta) & \frac{\Delta m^2}{4E} \cos(2\theta) \end{pmatrix} \begin{pmatrix} \nu_e \\ \nu_x \end{pmatrix} \quad (1.21)$$

In the simple case of constant density, this results in an oscillation probability of [89]

$$P_{e \rightarrow x} = \sin^2(2\theta_m) \sin^2\left(\frac{\Delta m_m^2 L}{4E}\right) \quad (1.22)$$

which is identical to the vacuum case only with altered mixing parameters.

The mixing parameters in matter become

$$\sin^2(2\theta_m) = \frac{\sin^2(2\theta)}{\left(\cos(2\theta) - \frac{2E}{\Delta m^2} V\right)^2 + \sin^2(2\theta)} \quad (1.23)$$

$$\Delta m_m^2 = \Delta m^2 \sqrt{\left(\cos(2\theta) - \frac{2E}{\Delta m^2} V\right)^2 + \sin^2(2\theta)} \quad (1.24)$$

which will both return to their vacuum analogue for $V \rightarrow 0$.

In the case of non-constant electron density, the theoretical framework will get more complicated. Usually, a time-dependent analysis of eq. (1.20) is treated numerically [21]. For more detailed derivations of eqs. (1.19) to (1.24), see for example [21, 58, 63, 70, 89].

¹Common terms in diagonal components will not result in phase differences for neutrino mass eigenstates, hence do not contribute to oscillations and can be omitted

Mikheyev-Smirnov-Wolfenstein Effect

The Mikheyev-Smirnov-Wolfenstein (MSW) effect is a resonant change of oscillation probability during propagation through matter, i.e. electron density profiles.

The so called MSW resonance condition is already present in eq. (1.23)

$$\frac{\Delta m^2}{2E} \cos(2\theta) = V = \sqrt{2} G_F n_e \quad (1.25)$$

which implies maximal mixing ($\theta_m = 45^\circ$) is possible in matter, even if the vacuum mixing angle is small.

Furthermore, the MSW resonance depends on the sign of Δm^2 . This means, it will affect either neutrinos ($V > 0$) or anti-neutrinos ($V < 0$) and hence, a precise measurement of its matter effect, has access to the mass ordering of eigenstates. This ordering, generally called *neutrino mass hierarchy*, is usually part of the main objectives of neutrino experiments at low to medium energies, that is, of orders up to a few MeV. [21]

One example application is the *solar neutrino problem*, an observational deficit in *solar neutrino flux* of ν_e [29]. Among others, this was confirmed by e.g. the *Kamiokande Experiment* [10] and *SNO* [78] and can be explained using the MSW effect in combination with the density profile of the sun. [107]

Parametric Resonance

Propagating neutrinos can undergo *parametric resonance* if the density profile along their path matches a certain periodicity. This can greatly enhance their oscillation probability, even if vacuum mixing is small. [58]

Since a detailed theoretical treatment would require a more extensive framework it will be omitted at this point. A detailed derivation of the effect can be found in [e.g. 22].

1.3.3 Neutrino Mass Hierarchy

While neutrino oscillations provide experimental access to parameters like the weak mixing angles and the squared mass differences, they are insensitive to the absolute mass scales m_k of the neutrino mass eigenstates. The pre-dominant problem arising from this is the determination of the neutrino mass hierarchy.

The magnitudes of the squared neutrino mass differences have been measured by numerous experiments including e.g. *Super Kamiokande* [56], *KamLAND* [11], *Double Chooz* [12] and *Daya Bay* [24]. The best-fit parameters are summarized in table 1.2.

However, while the sign of the solar mass splitting has been determined using matter effects of the earth [58], the determination of the neutrino mass hierarchy, that is, the ordering of mass eigenstates, remains unknown to date. The determination of a *normal* (NH) or *inverted* (IH) neutrino mass hierarchy, i.e.

$$m_1 < m_2 < m_3 \quad (\text{NH})$$

$$m_3 < m_1 < m_2 \quad (\text{IH})$$

poses one of the major goals of current and future neutrino experiments operating with low to medium neutrino energies.

Parameter	Best-Fit $\pm 3\sigma$	
	NH	IH
Δm_{21}^2 [10^{-5} eV 2]	7.37 $^{+0.60}_{-0.44}$	
$ \Delta m^2 $ [10^{-3} eV 2]	2.50 $^{+0.13}_{-0.13}$	2.46 $^{+0.14}_{-0.13}$
$\sin(\theta_{12})$	0.297 $^{+0.57}_{-0.47}$	
$\sin(\theta_{23})$	0.437 $^{+0.179}_{-0.58}$	0.569 $^{+0.68}_{-0.186}$
$\sin(\theta_{13})$	0.0214 $^{+0.0032}_{-0.0029}$	0.0218 $^{+0.0030}_{-0.0032}$
δ/π	1.35 $^{+0.64}_{-0.43}$	1.32 $^{+0.67}_{-0.49}$

Table 1.2: Current best-fit parameters of the weak mixing properties for normal (NH) and inverted (IH) neutrino mass hierarchy – here, it is $\Delta m^2 = m_3^2 - (m_2^2 + m_1^2)/2$. Values taken from [94].

1.4 The Neutrino Universe

The universe is constantly permeated by a neutrino flux of various energy spectra and astrophysical origins. Due to their weak nature, they are able to escape almost any environment effectively undisturbed and hence offer the unique possibility to observe otherwise inaccessible processes. At the end of this section, fig. 1.4 shows a summary of different neutrino fluxes.

1.4.1 Solar Neutrinos

For a long time in history, the physics necessary to explain the energy generation of active stars, specifically the sun, were not well understood [46]. It was the pioneer observation of the solar neutrino flux in the *Homestake experiment* [51] in 1970 that started the era of solar neutrino experiments and was later joined by e.g. *Kamiokande*, *GALLEX*, *SAGE* and *SNO*.

Active stars, like the sun, produce energy by fusing light elements in their cores. As such, they are powerful electron neutrino generators since, naturally, protons will have to convert to neutrons to form heavier elements. The weak process governing all these fusion reactions is

$$p \rightarrow n + e^+ + \nu_e \quad (1.26)$$

which produces neutrinos of various energies depending the constituents. In the sun, the mean neutrino energies range from 0.4 – 15 MeV and result mainly from the *pp-chain*. [62]

Today, the major objective of solar neutrino research is the precise determination of neutrino properties and mixing parameters. However, the study of solar neutrinos has already surfaced two major contributions. For one, the postulated thermonuclear fusion process of stars was confirmed and provided the framework for the current *Standard Solar Model*. Secondly, the discovery of the solar neutrino problem led to the confirmation of neutrino oscillations and their matter effects. [62] The latter has already been briefly discussed in section 1.3.2.

1.4.2 Supernova Neutrinos

When the core of a massive star runs out of elements to fuse, it becomes unstable and eventually collapses. This collapse is immediately followed by an explosion with a colossal energy release which dismantles the star and expels its outer shells in a violent blast. Depending on the initial mass of the star, the remnant is either a *neutron star* or a *black hole*. This so called *core collapse* represents the more common of two main supernova mechanisms.

Neutrinos generated from such a core collapse are predicted to carry away up to 99% of the explosion energy [62] and offer the unique possibility to access internal conditions of such an event. Their emission is expected in bursts of seconds with energies of order 10 MeV, both of which varies in time and for different initial conditions of the core collapse. [73] It is also expected that the entirety of cosmological supernovae in the universe form a *diffuse supernova neutrino background* (DSNB) flux, however, this has not been observed yet.

The only supernova detected in neutrinos to date was *SN1987A*. In the three detectors of *Kamiokande II*, *IMB* and *Baksan*, an unusual neutrino burst was observed in a time window of around twelve seconds in 1987. The observed neutrino signature also matches remarkably well with predictions from theory and was the first milestone of *neutrino astronomy*. [62]

1.4.3 Atmospheric Neutrinos

Atmospheric neutrinos are the result of incident hadronic particles on the earth's atmosphere. These hadrons, traversing the whole universe, are called *cosmic rays* and can potentially reach ultra-high energies. To better understand the generation mechanism and signatures of atmospheric neutrinos, cosmic ray phenomenology will be outlined first.

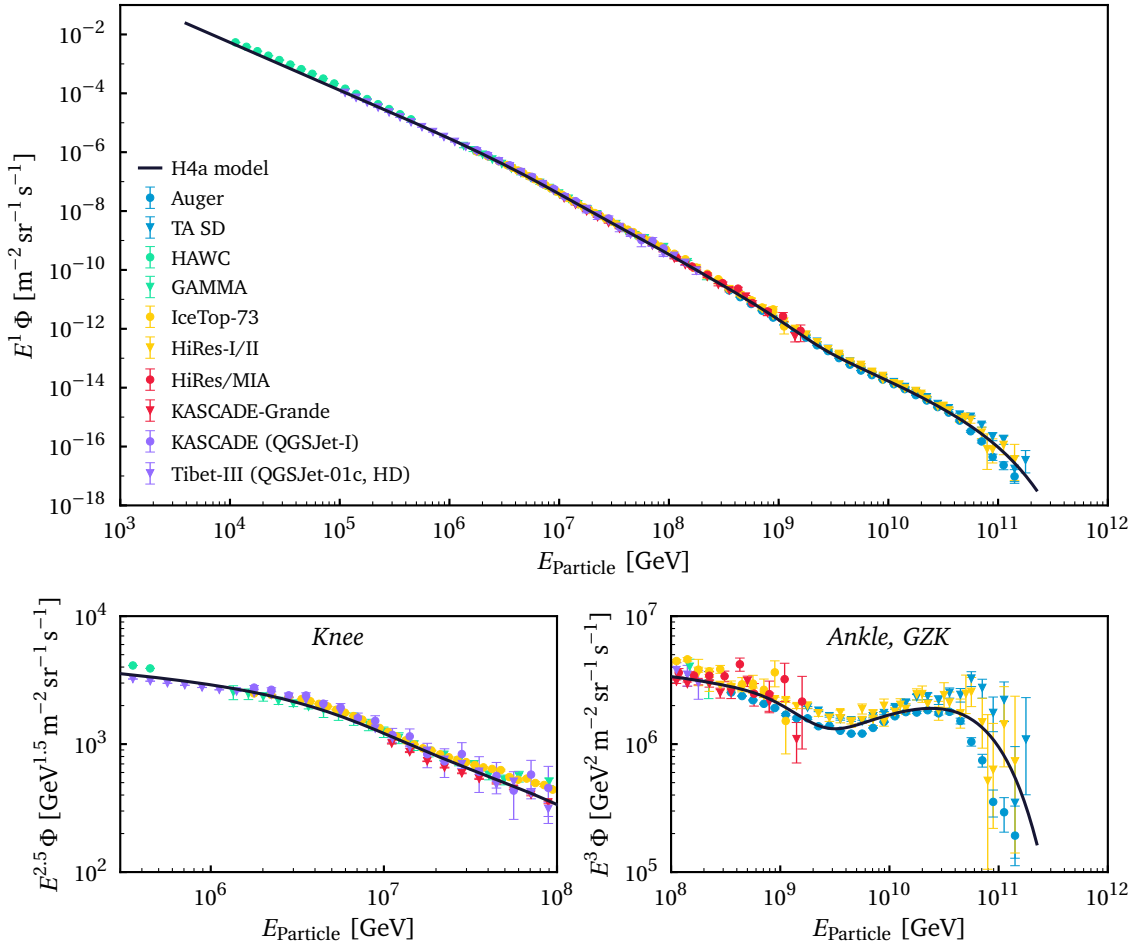


Figure 1.3: All-particle energy spectrum of high-energy cosmic rays from various experiments. The full high-energy spectrum (top) and enhanced views of distinct spectral features (bottom) are displayed. For an explanation of theoretical backgrounds on the latter, refer to the text. Data courtesy of T. Gaisser, R. Engel, E. Resconi [58] and K. Krings.

Unlike neutrinos, cosmic rays are charged particles and hence largely affected by the conditions present along their path. They are not only deflected in magnetic fields of e.g. galaxies, but can also be scattered from interstellar medium [53] and even annihilate with photons of the *cosmic microwave background* (CMB) at very high energies [120]. All of which makes it so challenging to determine the sources and mechanisms responsible for their vast energies.

In fig. 1.3, the characteristic *all-particle* energy spectrum of high-energy cosmic rays is shown. Here, the kink between $10^6 - 10^7$ GeV is the so-called *knee*. It is argued to represent the maximum energy reached by most of the galactic accelerators. The *ankle*, at roughly 10^{10} GeV, is theorized to be caused by one population of cosmic rays being overtaken by a higher energy one. For instance, the extragalactic flux dominating over the galactic one. [94] Lastly, the ultra-high-energy cutoff is usually explained via the annihilation of extragalactic cosmic rays with photons of the CMB. This is called the *Greisen-Zatsepin-Kuzmin (GZK) effect* [65, 126]

$$p + \gamma_{\text{CMB}} \rightarrow \Delta^+ \rightarrow \begin{cases} p + \pi^0 \\ n + \pi^+ \end{cases} \quad (1.27)$$

which effectively provides an upper limit on the travel distance of cosmic rays. Together with the observed conditions present in the universe, this could explain the steep decrease of the cosmic ray flux at $\sim 10^{11}$ GeV. [120] However, current high-energy models are strongly parameter-dependent and also vary in the underlying theoretical assumptions. [58]

The cosmic ray nuclear abundance is dominated by protons, but most elements up to Iron are found in non-vanishing quantities. While energies up to the ankle are mainly populated by protons, the composition of the high-energy end of the cosmic ray spectrum is still an active field of research. Current models predict the high-energy end to be dominated by heavier nuclei [58], but experimental observations are controversial. Results of *Hi-Res* [8] suggest a mainly light composition above 10^{18} GeV, however, the *Pierre Auger Observatory* data [114] indicates the composition becoming heavier after around 2×10^{18} GeV. Further research and experiments are necessary to better resolve the ultra-high-energy composition of cosmic rays.

While their sources have not been identified yet, there are numerous models and theories predicting various types of processes to be responsible for different energies of cosmic rays, these assumptions remain to be confirmed. Current astrophysical candidates generating ultra-high-energy cosmic rays are, for example, *active galactic nuclei* [60], *tidal disruption events* [67] or *gamma ray bursts* [61].

Coming back to atmospheric neutrinos, cosmic rays incident on the earth are likely to collide with nuclei in the atmosphere. These collisions are deeply inelastic for high-energy cosmic rays and induce cascades of secondary particles in forward direction. In turn, those can either interact with further nuclei in the atmosphere or decay. Both of which fuels a cascade of particles that will go on until the available energy is depleted and the shower will disperse. These cascades are usually called *air showers* and produce a variety of particles, including neutrinos. Air showers can be created not only by cosmic rays, but also gamma rays. However, their specific signatures are dependent on the type and energy of the incident particle.

The main sources of atmospheric neutrinos are the decays of pions and muons

$$\begin{aligned} \pi^\pm &\rightarrow \mu^\pm + \nu_\mu \\ &\hookrightarrow e^\pm + \nu_\mu + \nu_e \end{aligned} \quad (1.28)$$

with kaons contributing significantly to their production only at higher energies. [62]

The flux of atmospheric neutrinos, created from the decay of pions, kaons and the resulting muons, is usually called *conventional neutrino flux*. Neutrinos resulting from the rapid decay of heavier, charmed or bottom mesons on the other hand, are called *prompt neutrino flux*.

Observations of *IceCube* [1], *AMANDA* [9], *ANTARES* [27] and *Fréjus* [50] suggest, their energy distribution usually peaks in the GeV regime and continues following an approximate power law to higher energies. [62] However, so far only the conventional component has been experimentally observed [5]. Measurements and current models are included in fig. 1.4.

1.4.4 Cosmogenic Neutrinos

High-energy cosmic rays can interact with the cosmic background radiation and produce secondary particles. The primary process for high energies is the GZK effect, secondary processes are only relevant for lower energies ($< 10^{15}$ eV). [23]

These interactions result in the production of pions, ref eq. (1.27), that will decay and create further decaying muons and subsequently neutrinos. Neutrinos of that origin are called *cosmogenic neutrinos* and can reach potentially extreme energies available from cosmic rays.

1.4.5 Relic Neutrinos

After the big bang, the universe was filled with plasma. As it began to expand and cool down, weak interaction rates dropped and neutrinos decoupled from thermal equilibrium. This *cosmic neutrino background* (or *CνB*) was relativistic when decoupling but, due to expansion, has a temperature of around 1.95K today. These relic neutrinos would offer an invaluable insight into the very early universe, but remain undetected to date. [62]

To finish this section, a complementary collection of models and experimental results for all mentioned neutrino spectra is given in fig. 1.4.

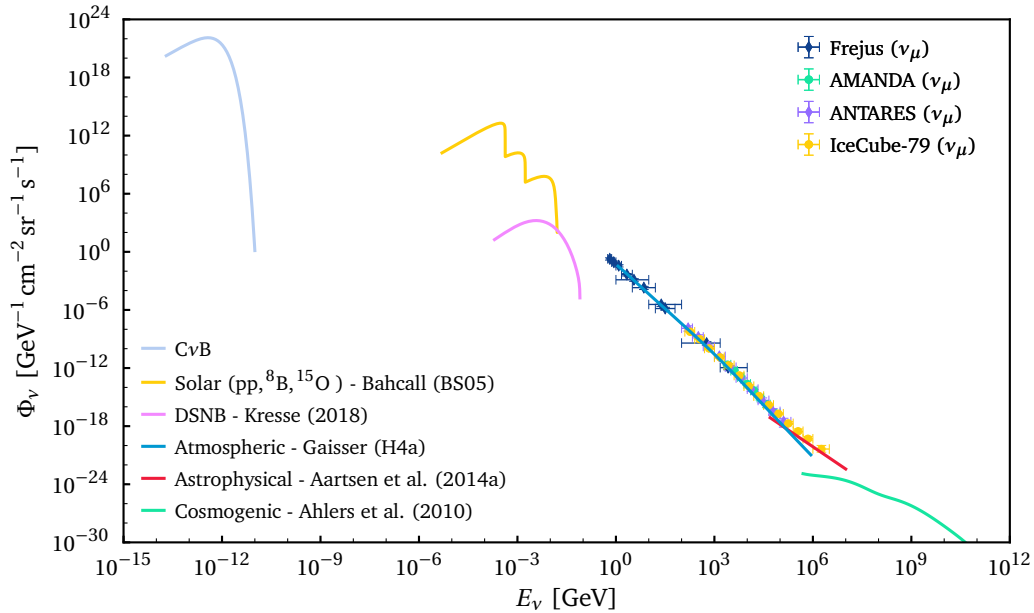


Figure 1.4: Cosmic neutrino fluxes as a function of energy. Experimental data is from *Fréjus* [50], *AMANDA* [9], *ANTARES* [27] and *IceCube* [1]. Exemplary all-flavor model assumptions for solar, DSNB, atmospheric, astrophysical and cosmogenic neutrino flux are based on Bahcall [37–39], Kresse [81], Gaisser [54, 59], Aartsen et al. [6, 125] and Ahlers [18], respectively. Especial gratitude goes to M. Ahlers, D. Kresse, S. Meighen-Berger and K. Krings for invaluable input.

2

Large Scale Neutrino Telescopes

Neutrinos are weak interacting particles and thus challenging to detect. In this chapter, the main physical principles for high-energy neutrino observation will be summarized. Additionally, the techniques, infrastructure and problems of existing neutrino telescopes will be outlined. The chapter will then close with possible future prospects of neutrino astronomy and an introduction to the exploration of a potential new neutrino telescope site.

2.1 High-Energy Neutrino Detection

Large scale neutrino detectors aim for the detection of high-energy neutrinos far above the GeV regime, by observing neutrino-induced secondary particles. The major goal of these observations is to enable *neutrino astronomy*, that is, the observation of high-energy neutrino sources in the universe and the investigation of their underlying astrophysical objects and mechanisms.

2.1.1 Neutrino Interactions

When neutrinos travel through matter, they can scatter off of nuclei via weak interactions. At high energies, these scatters are usually deeply inelastic and produce showers of secondary particles which can carry significant energies. Possible charged and neutral currents are

$$\nu_\alpha + N \rightarrow l_\alpha + X \quad (\text{CC}) \quad (2.1)$$

$$\nu + N \rightarrow \nu + X \quad (\text{NC}) \quad (2.2)$$

with nuclei N , neutrinos and leptons of flavor $\alpha = \{e, \mu, \tau\}$ and hadrons X .

In neutral current events, the scattered neutrino will usually keep most of its energy. Only a fraction is deposited in induced hadronic showers. Charged currents on the other hand, will transfer most of the neutrino energy to the induced lepton. [58]

Secondary particles can carry away significant energies from the neutrino interaction. As such, processes are available to them that result in the creation of photons. Hadronic showers create variety of particles, some of which can create photons by decay (e.g. π^0), bremsstrahlung, ionization, pair production or further processes. With enough energy available, this can cause an electromagnetic cascade in matter, producing further photons in the process. At high energies, the *Cherenkov effect* will significantly contribute to the photon production, it will be discussed hereafter. In fact, the detection of Cherenkov photons is the most common technique used to detect neutrinos in neutrino telescopes and the reason for their operation in large and optically transparent media, like water or ice.

2.1.2 The Cherenkov Effect

When high-energy neutrinos in matter interact via charged currents, they produce a charged lepton carrying away most of the energy of the neutrino. As such, these leptons will traverse the detector with extreme velocities possibly larger than the speed of light in the detector medium.

In the case of the latter, the charged particle will induce photon emission along its path, which is called the *Cherenkov effect*. Of course, this is also possible for charged high-energy particles in induced hadronic or electromagnetic cascades.

A dielectric medium with refractive index n , has a local speed of light of

$$c_n = \frac{c}{n} \quad (2.3)$$

If a charged particle traverses this medium, it will cause local polarization of charges. If its velocity is smaller than the speed of light in that medium, i.e. $v < c_n$, then this local disturbance will be symmetric and annihilate. However, should the particle exceed local speed of light, i.e. $v \geq c_n$, it will have left before polarization could relax back to equilibrium. This will leave behind asymmetrically polarized matter, the relaxation of which will no longer annihilate but instead result in the emission of electromagnetic waves, i.e. Cherenkov radiation.

The origin of this emission will follow the trajectory, however, the photons will be emitted with an angle θ relative to it which is specific to the particle's velocity and the medium. From geometrical arguments of the particle trajectory, it is

$$\cos(\theta) = \frac{1}{\beta n} \quad (2.4)$$

with the refractive index n and the velocity ratio of the particle $\beta = v/c$. A phenomenological depiction of the Cherenkov effect is also shown in fig. 2.1.

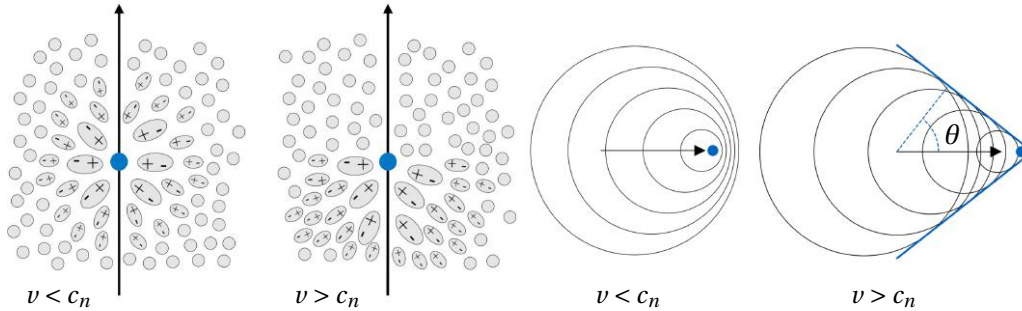


Figure 2.1: Qualitative summary of the Cherenkov effect. Left and right panels show the polarization behaviour of the medium and its relaxation wavefronts for particles with velocities smaller and larger than the local speed of light c_n . Left figure is from [52] and was modified.

Analytically, the photon yield per traveled distance and wavelength for Cherenkov radiation is related to the particles charge $q = z \cdot e$ and velocity as well as the refractive index of the medium. It takes the form

$$\frac{d^2 N}{dx d\lambda} = \frac{2\pi\alpha z^2}{\lambda^2} \left(1 - \frac{1}{\beta^2 n^2(\lambda)} \right) \quad (2.5)$$

which is dominant towards smaller wavelengths. As will be seen later, it shows significant light output in the visible regime between 300 – 600nm in water and ice.

2.1.3 Detector Principles

For reasonable performance, a neutrino telescope has to unify various key characteristics. First and foremost, it has to encompass a large mass and volume to be able to detect neutrinos at an acceptable rate and enable resolution of high-energy particles. Secondly, the detector material has to be optically clear to allow for undisturbed detection of neutrino induced photons. Lastly, its infrastructure and site have to allow for long-term stability and cost efficiency.

Nonetheless, all existing neutrino telescopes follow the same general detection principle for high-energy neutrinos, that is, the instrumentation of a large optical detector volume with a photosensor array. To then sufficiently detect neutrinos of extreme energies, the dimensions of such a detector body have to be of the order of at least kilometers. Furthermore, it has to be located far below the surface so that adequate shielding from atmospheric particles and radiation allows detection of small fluxes with extreme energies. The optical material of choice is water or ice, which is already present in nature and can be instrumented in great depths.

The focus of the array is then the detection of the previously explained secondary photons induced by neutrino interactions. Since the most commonly used sensors detect visible light, the observation of induced Cherenkov radiation is the focus of the array. The goal is then to reconstruct the neutrino energy and direction by accurately measuring the amount of Cherenkov light and its time distribution at various sensor positions within the array.

Nevertheless, the optical properties of specific sites should be investigated before construction, as they are essential to the detector performance. The key characteristics of the detector are its resolution in direction and energy and are affected by the optical properties of the medium. For both, absorption and scattering should ideally be minimal. The key characteristics quoted in relation to neutrino telescopes are the *absorption* and *scattering length*. Both describe the distance after which the probability that a photon has not been absorbed or scattered, is $1/e$. Further details on optical properties will follow at a later point.

2.1.4 Neutrino Signatures

Neutrino interactions of different flavors should in theory produce distinct signatures in neutrino detectors. However, limited resolution and systematical effects lessen the potential of the detector to actually resolve them. In the following, the theoretical imprint of different interactions will be summarized.

Charged Currents

A neutrino undergoing a charged current interaction in matter will produce a charged lepton via exchange of a W^\pm boson. At high energies, these interactions will be deeply inelastic and the leptons show little deviation from the incident neutrino direction. Additionally, secondary particles are produced from the hadronic fraction taking part in the interaction.

In the case of an electron neutrino, the electron will initiate a forward electromagnetic cascade producing radiation including Cherenkov light. The hadronic components will also contribute to the photon production by the Cherenkov effect of high-energy charged particles. Depending the optical properties of the medium, cascades usually lose most of the directional information upon interaction due to particles being emitted in various directions. While in such a case the energy can be well reconstructed, directional information is challenging to deduce.

Muon neutrinos show a different signature. The minimum-ionizing muon will traverse the detector volume on a track while emitting Cherenkov light. However, above a critical energy, also radiative and hadronic energy losses become significant [58]. While these tracks are ideal for the reconstruction of the incident neutrino direction, to infer the neutrino energy is difficult. The reason is mainly that usually only a fraction of the track is contained in the detector volume and various energy losses at higher energies have to be determined statistically.

The most distinct signature stems from tau neutrino interactions. Upon interaction, a first hadronic shower is initiated and a tau lepton is produced. The tau carries most of the incident neutrino energy but decays quickly due to its short lifetime of only 2.9×10^{-13} s [94]. However, it will emit Cherenkov radiation on a track similar to the muon before decaying into hadrons

or lighter leptons creating another cascade. It is only at energies of the order of PeV where both vertices can usually be separated, this scenario is then called a *double bang*. [58] As of today, no definitive high-energy tau double bang has been identified.

Neutral Currents

Neutral currents of incident neutrinos are effectively them scattering off of nuclei by the exchange of a Z^0 boson. At high energies, these collisions are deeply-inelastic and will usually produce hadronic showers, however, most of the energy stays with the scattered neutrino.

As for the detector signature, a hadronic shower resembles an electromagnetic cascade. It will produce a mostly spherical deposition of light with little directional information.

Currently, detectors are usually only able to differentiate between muon tracks and cascades. Furthermore, the true origin of a cascade usually remains unknown. The present optical properties of the medium also greatly influence the actual signature of different event types and so, are a crucial point of investigation for precise observations. It is the task and intention of new telescopes and upgrades of existing ones that should ultimately enable to further disentangle observed events.

Pioneered by IceCube, it is common in this field to portray events in the grid of photosensors to infer the a complementary picture for each event. These event views are shown exemplary for the IceCube detector in fig. 2.2.

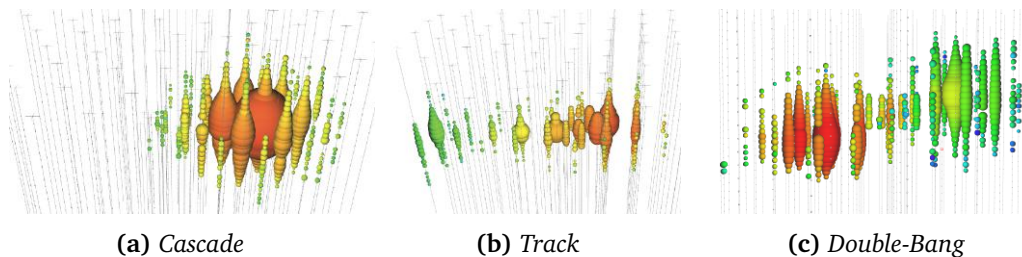


Figure 2.2: High-energy neutrino signatures in the IceCube detector. The visible dots represent photosensors, the lines are columns of the sensor array. The size of a dot resembles the amount of light it detected, the color its arrival time from early (red) to late (blue). For reference, the vertical spacing of bulk sensors in IceCube is 17 meters. Figures taken from [71].

2.2 Active Neutrino Telescopes

In the relatively young past of active neutrino telescopes, only a few were sufficiently funded and eventually finished construction. In this section, three of the currently pursued projects will be introduced. Starting with the finished and running IceCube detector, two telescopes under construction, namely *Baikal GVD* and *KM3NeT*, will be discussed.

2.2.1 Pioneer Experiments

Before the rise of neutrino astronomy and the instrumentation of large optical media to detect high-energy neutrinos, the *DUMAND* experiment [35, 44] pioneered exploring the theoretical idea of using large-area photosensors to do so in the 1970s. Although being never realized, it paved the way for the successful pioneer experiments *Baikal* [43], *AMANDA* [26] and *ANTARES* [16], all of which confirmed the feasibility of the technique and provided key scientific contributions to neutrino astrophysics. It were achievements like these which ultimately enabled the realization of further and more advanced neutrino telescopes.

2.2.2 IceCube

The IceCube neutrino telescope is operating since 2010 and is located at the South Pole as the successor of the AMANDA detector. As seen in fig. 2.3, it instruments a volume of almost one cubic kilometer of antarctic ice with an array of 5160 photosensors located on 86 *strings*. The latter are vertical lines providing electrical connection and mechanical support. The photosensors are called *digital optical modules* (DOMs) and consist of a large 10" downward-facing photomultiplier tube (PMT) and read-out electronics encapsulated in a glass pressure sphere. Its design allows detection of neutrinos between approximately $100 - 10^9$ GeV [76].

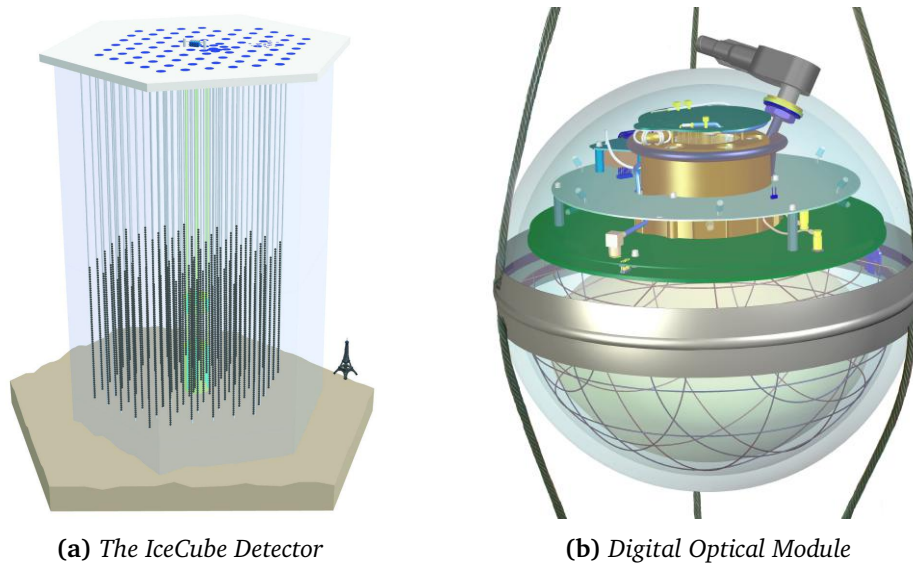


Figure 2.3: (a) The IceCube detector array. The ice is instrumented with photosensors from a depth of 1.5 to 2.5 km. The marked volume in the array is DeepCore, a denser instrumented region for lower energies. IceTop on the surface is primarily used for atmospheric measurements. (b) An IceCube sensor module. Visible is the large 10" PMT, its electronics, the pressure sphere, the electrical penetrator and the harness. Images are a courtesy of the IceCube collaboration.

The antarctic ice has proven to be exceptionally clear for radiation of 300 – 600 nm [13, 31]. With average absorption lengths of the order of 100 m, only the scattering length with around 25 m, is of real concern. However, systematic uncertainties still pose the major challenge for the performance of IceCube. For one, the optical properties of the ice volume can only be determined with an uncertainty of at least 10% [4]. This includes also the refrozen ice in the drill holes surrounding the DOMs [104]. Secondly, the individual DOM efficiency and angular acceptance is another major contributor to systematic uncertainties. Current means leave room for more precise calibration and new methods and instrumentations are subject of ongoing studies.

IceCube is among the most successful neutrino telescopes and has made key contributions to neutrino astrophysics. Most recently, it made the breakthrough-observation of the first potential neutrino point-source in the universe [93, 112, 113]. Additionally, it has significantly contributed to observations of both atmospheric [e.g. 1, 5] and astrophysical [e.g. 6] neutrinos and detected the highest-energetic neutrinos to date with energies above 1 PeV [2].

The future prospects of IceCube are further upgrades. Most importantly, *IceCube-Gen2* [3] and *PINGU* [4]. The former would include a volume increase from approximately 1 to 10 km³, the latter is a planned extension of the low-energy instrumentation in the core of IceCube. However, at this time, the funding situation of these upgrades remains to be solved.

2.2.3 Baikal GVD

Among the first neutrino telescopes to start construction was the *Baikal Neutrino Telescope* in 1984. After site surveys and first string deployments, its first stage, *NT200*, started operation in the spring of 1998 with a configuration of eight strings and 192 optical modules in a depth of 1.1 km of lake Baikal. The photosensors were PMTs encapsulated in a glass pressure sphere. In 2005 it was upgraded for higher energies. [28, 34]

With the dimensions necessary for the detection of high-energy neutrinos, the Baikal collaboration started pursuing the *Gigaton Volume Detector* (GVD) project. The planned final geometry of this telescope should contain a total of eighteen clusters similar to the one of NT200. Each cluster should host 288 photosensors on eight strings of 520 m length, operated in the depth of the Baikal lake. Phase-1 in fig. 2.4 will host eight clusters and is planned to be finished 2020/21. The second and final phase will eventually exceed a volume of one cubic kilometer. [110] As of today, three clusters have successfully finished construction.

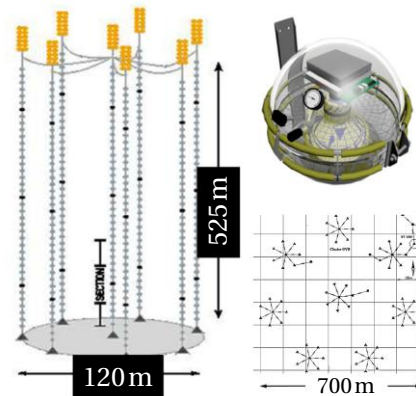


Figure 2.4: GVD cluster, photosensor and Phase-1 layout. Image courtesy of B. Soibonov from the GVD collaboration.

The potential of the finished GVD neutrino telescope with its large volume is evident, however, the Baikal water quality poses the main challenge for the collaboration. Here, an expected absorption length of 20 – 24 m at 480 nm [28, 40] impacts the light yield of Cherenkov photons within the detector volume and with it its performance. Nevertheless, promising results of the existing clusters have been presented in 2017 [33].

2.2.4 KM3NeT

The possibility of a deep-sea neutrino telescope initiated by DUMAND was further explored by the projects *NESTOR* [25], *ANTARES* [32] and *NEMO* [105] for sites in the Mediterranean Sea. It was *ANTARES* that succeeded in deploying the first deep-sea neutrino telescope in 2008. The detector design contains twelve strings with 25 *storeys* (levels) of three photosensors each. Again, the photosensors are PMTs operated within glass pressure spheres. The telescope is operating to this day and proves the feasibility of such a deep-sea infrastructure.

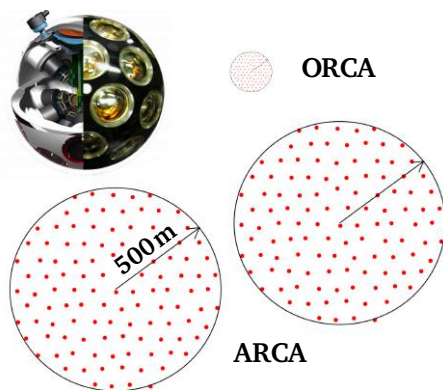


Figure 2.5: KM3NeT layout and its new photosensor. Figures from [15, 85, 110].

During the time of IceCube construction, the *High Energy Neutrino Astronomy Panel* concluded in its report of 2002 that a cubic kilometer neutrino telescope should be built in the northern hemisphere to complement IceCube in the South. As a result, the Mediterranean groups have started the *KM3NeT* (km^3 Neutrino Telescope) collaboration with marine science groups and experts from deep-sea technology to build a new cubic kilometer neutrino observatory. [77]

The KM3NeT detector will be located at three different sites throughout the Mediterranean Sea in depths of 2.5 – 4.5 km and is currently under construction. Two sites will act as a unit called *ARCA* (Astroparticle Research with Cosmics in the Abyss) and will be used complementary for astroparticle physics and high-energy neutrino detection. Each *building block* will encompass 115 strings with 18 photosensors each, installed in a volume of almost

half a cubic kilometer. The third site will host what is called *ORCA* (Oscillation Research with Cosmics in the Abyss) which will be smaller but equally instrumented for the investigation of low-energy effects, especially neutrino oscillations. Furthermore, a new generation photosensor module was developed in the scope of the KM3NeT project. It hosts 31 small instead of one large PMT and hence offers more photosensitive area and better hit-differentiation due to the possibility to check direct local coincidences. [15, 36] Both, the detector layout as well as the design of its potential new photosensor module are shown in fig. 2.5.

Lastly, the water properties present in deep waters at the locations of the KM3NeT sites have also been investigated and are very convincing. With absorption lengths of $\sim 20 - 70\text{m}$ [36, 102] and scattering lengths of $\sim 120 - 300\text{m}$ [36] for radiation in the range of $375 - 550\text{nm}$, the sites prove well-suited for Cherenkov light propagation and therefore neutrino detection.

Even though the KM3NeT collaboration has faced some issues deploying the first parts of the deep-sea infrastructure, with the funding becoming available, the future of this neutrino telescopes is promising. Once finished, it could provide a complementary all-sky coverage in combination with IceCube and furthermore, could prove essential in contributing towards the discovery of high-energy neutrino point-sources in the universe and neutrino mixing. [15]

2.3 Future Prospect of Neutrino Astronomy

While the rise of neutrino astronomy of recent years has spawned an exciting number of projects in the field, as of today, progress is stagnating. All telescope collaborations face challenges, however, are putting in immense effort to resolve them. While the IceCube detector is limited by systematics of the ice, the collaboration is attempting to resolve the funding situation for its upgrades. The funding for the full GVD detector is also not guaranteed yet. Furthermore, the optical properties of the Baikal water are not ideal. Lastly, the KM3NeT collaboration faces the complexity of deep-sea infrastructure deployment and maintenance but its detectors incorporate immense scientific potential.

As science evolves, this eventually resulted in opportunities to reach out and investigate further possible sites for new neutrino telescopes. Following up preliminary discussion with Claude Vallee and Stefan Schönert, it were the groups around Prof. Grant from the University of Alberta and Prof. Resconi from the Technical University Munich that initiated the thought of exploring a possible new site. It was the *Cascadia Basin* in the Northern Pacific which is located off to the shore of Vancouver Island and brings the benefit of already having an electrical and optical deep-sea infrastructure in place and is maintained by experts.



Figure 2.6: *Cascadia Basin location. Figure from [64].*

The Cascadia Basin is an abyssal plane in the North Pacific with a depth of around 2.7 km. It is part of the oceanic infrastructure constructed, deployed and maintained by *Ocean Networks Canada* (ONC) [91], a Canadian facility of the University of Victoria. ONC provides the infrastructure and with it access to the deep-sea for scientific instruments of all fields from physics to geology. The current main activities include marine and oceanic science as well as biological and global warming research. The main idea is to provide deep-sea infrastructure and marine expertise to deploy and operate instruments provided by scientific groups from all over the world. Furthermore, it offers the possibility to work with experts on the difficult subject of deep-sea deployment, operation and maintenance.

Large Scale Neutrino Telescopes

This work will cover the realization and process of designing, building and calibrating a prototype detector that will be deployed at the Cascadia Basin the summer of 2018. The major task of which will be to characterize the optical properties of the deep-sea water, monitor their seasonal variation and ultimately enable judgement of the feasibility of the site for a large scale neutrino telescope.

II

STRAW

Strings for Absorption Length in Water

The focus of the *Strings for Absorption Length in Water* (STRAW) project is to investigate the Cascadia Basin for its feasibility as a possible new large scale neutrino telescope site. The major objective of this work was to design, build and help deploy a deep-sea detector able to characterize the deep waters of this site in terms of optical properties and their seasonal variation. The timeline of this process was eight months.

The STRAW project aims for the investigation of a possible new large scale neutrino telescope site in the deep sea of the Northern Pacific. As such, this chapter will start with a presentation of the experimental objectives and the necessary instrumentation to achieve them. Then, optical prerequisites of the site and instruments will be discussed with the goal of defining the wavelength range to be probed as well as the detector geometry.

3.1 Experimental Objectives

The scientific task of the STRAW project is the determination of optical properties of water present in the deep sea of the Cascadia Basin. The dominant quantities of an optical medium to enable light detection are absorption and scattering as well as background radiation. All of which are important as they primarily determine the performance of a possible neutrino telescope. In second order, the seasonal variations of these optical properties should be monitored.

3.1.1 Absorption- & Scattering Length

Light propagation in optical media is predominantly affected by absorption and scattering. While absorption processes cause photons to be absorbed by the medium itself, scattering can occur both on molecules (*Rayleigh scattering*) and on present matter particles (*Mie scattering*). Other processes are possible but usually less dominant in water [36].

It is common to characterize an optical medium according to the *absorption-, scattering- or attenuation length*. They define the path length after which an initial light intensity is reduced by a factor of $1/e$ via absorption, scattering or both. That is,

$$I_x(\lambda, r) = I_0 \exp(-x \cdot r) \quad (3.1)$$

where the coefficient x can describe absorption ($x = a$), scattering ($x = b$) or both as attenuation ($x = c = a + b$). The characteristic length is then defined as $L_x = 1/x$. While the precise determination of the scattering coefficient requires knowledge of the volumetric scattering function [36, 102], often an *effective scattering coefficient* is defined instead which makes use of an averaged scattering angle ϑ and results in

$$b^{\text{eff}} = \frac{1 - \langle \cos(\vartheta) \rangle}{L_b(\lambda)} \quad (3.2)$$

$$c^{\text{eff}} = a + b^{\text{eff}} \quad (3.3)$$

Furthermore, for isotropic sources this is also affected by the volumetric spread of the light and eq. (3.1) becomes related to the *transmission length* L_T , the volumetric analogue to the attenuation length

$$I(\lambda, r) = \frac{I_0}{4\pi r^2} \exp\left(-\frac{r}{L_T(\lambda)}\right) \quad (3.4)$$

However, the extraction of the attenuation length from the transmission length also requires knowledge of the volumetric scattering function. The latter is usually treated in the scope of simulations in combination with experiments measuring transmission lengths [e.g. 17, 36] and also enables extraction of absorption and scattering lengths.

The STRAW detector will provide transmission lengths measurements for a variety of wavelengths using numerous different distances between an isotropic light emitter and various light sensors. The experimental transmission length data will then be used together with dedicated simulations to deduce absorption, scattering and attenuation lengths of the Cascadia Basin site. Eventually, this will allow assessment of the site about its potential hosting a new large-scale neutrino telescope.

3.1.2 Light Background

Neutrino telescopes commonly use PMTs to detect Cherenkov photons created in optical media. As such, not only the direct optical properties of the medium are important for the telescope performance but also its present background radiation. That includes the remaining cosmic and atmospheric radiation of dominantly muons, radioactivity in the direct environment of the sensor producing Cherenkov and scintillation light as well as biological radiation caused by a variety of different organisms.

Radioactivity in sea water poses a constant and isotropic emission of highly energetic charged particles and thus of Cherenkov light. The main source of this radioactivity is potassium-40 (^{40}K) and is directly proportional to the salinity of the sea water [36]. As such, the influence on photosensors has been observed to change together with the seasonal variation of salinity.



Figure 3.1: *Bioluminescent jelly fish.* Picture is a courtesy of [69].

Biological luminescence (or *bioluminescence*) can be caused by various organisms present in deep waters and is usually emitted in blue to green wavelengths [68], exemplary seen in fig. 3.1. While the obvious, candidates bacteria and plankton, can cause a low but steady background light within the whole telescope with seasonal variation, there are also bigger deep-sea animals emitting light, like fishes, jellyfishes or octopi [86]. The latter should in general only disturb sensors for short times and in local volumes, however, then with much higher intensities.

While the depth of almost 2.7km already provides significant shielding against muons [45], the present radioactive and biological background can still cause disturbances on PMTs and will result in a presumably seasonally varying dark rate. In the worst case, seasonal biological luminescence could be severe enough to significantly limit the possible detector performance. In the scope of STRAW, also the seasonal variation of this background radiation will be monitored in order to allow feasibility checks of the site for a large scale detector.

3.2 Optical Prerequisites

The optical characterization in view of a neutrino telescope leads first to an investigation of the optical regime relevant for Cherenkov light production. As such, this section will not only treat the former but also the expected properties of the deep-sea water. Furthermore, the available spectral ranges introduced by various instrument components will be reviewed in order to define a reasonable wavelength range of operation for the STRAW detector.

3.2.1 Cherenkov Spectrum

First and foremost the Cherenkov spectrum will be reviewed. As evident from eq. (2.5), the photon yield increases towards smaller wavelengths. Upon integration in λ and assuming a high-energy charged lepton ($\beta = z = 1$) traveling through a medium of constant refractive index n , one finds

$$\frac{dN}{dx} = 2\pi\alpha \left(1 - \frac{1}{n^2}\right) \left(\frac{1}{\lambda_1} - \frac{1}{\lambda_2}\right) \quad (3.5)$$

which now relates the number of photons emitted per travelled distance in a wavelength bin of $[\lambda_1, \lambda_2]$ to the refractive index of the medium. This is visualized in fig. 3.2 and confirms the expectation of an increasing photon output towards smaller wavelengths. Furthermore, it justifies an upper limit of around 600 nm on the wavelength range to be investigated.

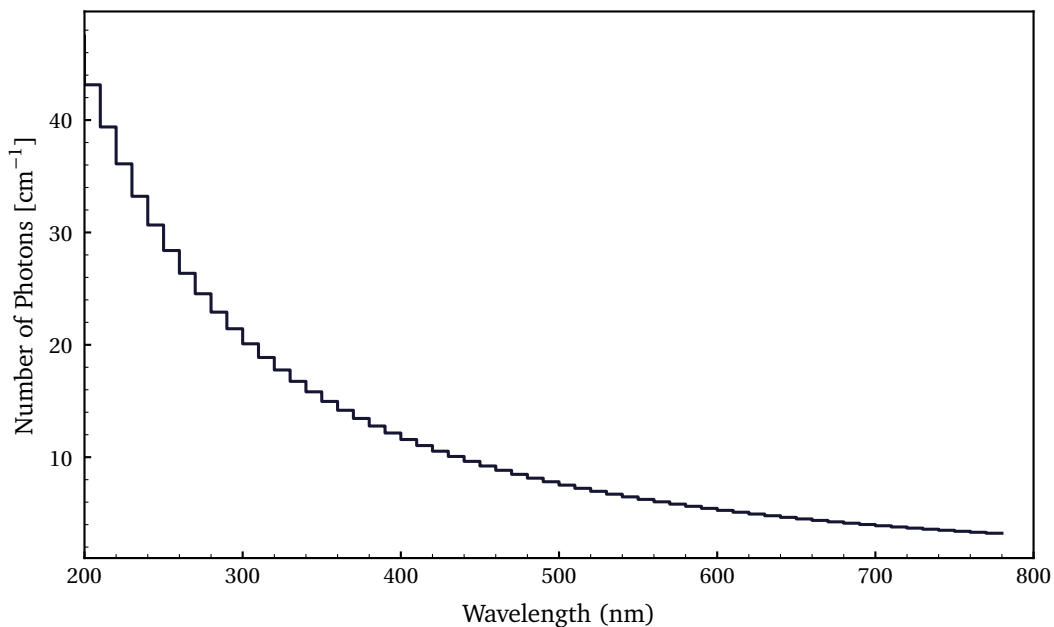


Figure 3.2: Number of emitted Cherenkov photons per distance. The histogram visualizes the number of emitted photons per centimeter in 10 nm bins obtained from eq. (3.5) for a charged particle with $\beta = z = 1$ and water as an optical medium estimated with constant $n = 1.33$.

3.2.2 Sea Water

The second aspect influencing the available spectral range is the sea water itself. While the objective of the STRAW project is the sea water characterization, previous experiments in the Mediterranean Sea [36, 102] have revealed that the expected attenuation lengths in Mediterranean deep waters are expected in the range of 40 – 60 m for blue light. Furthermore, they verified that the theoretical model of Smith and Baker [108] describes experimental observations of deep ocean waters reasonably well and it was expected to find similar conditions in the deep sea of the Pacific.

Using their model, the resulting spectral transmission curves are displayed in fig. 3.3 for various path lengths through water and further justify the upper limit of 600 nm. In fact, they also suggest a lower limit between 300 – 350 nm, which however was ultimately defined by the instruments. The detailed reasons for the latter can be found in chapters 4 and 5 but will also be outlined hereafter.

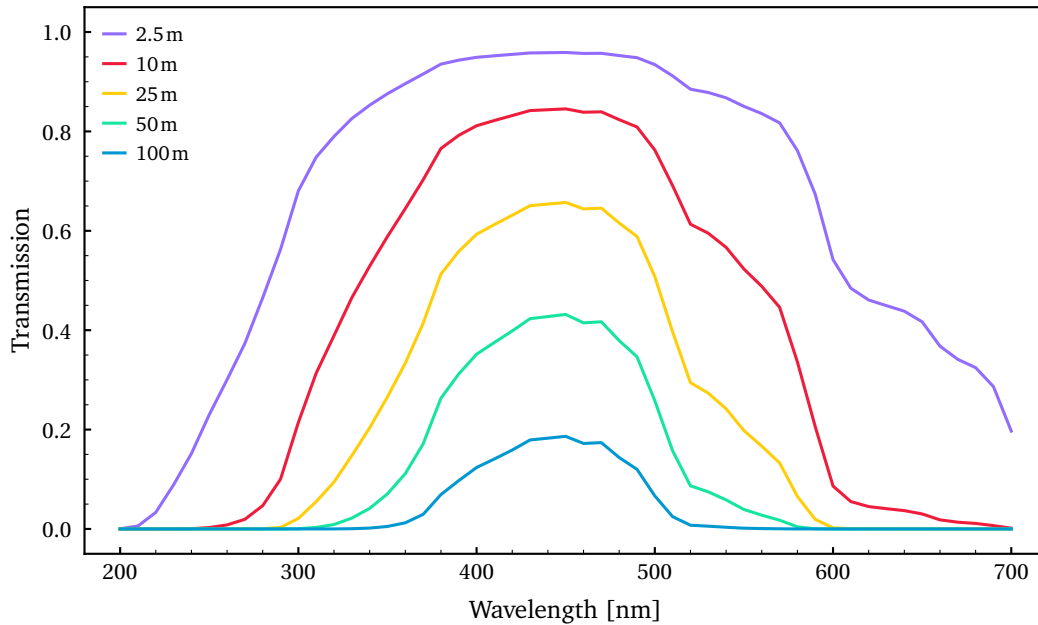


Figure 3.3: Spectral transmission of sea water according to Smith and Baker [108]. The different curves illustrate the remaining fraction of light after traveling different distances through clear ocean water. As can be seen, only wavelengths around 400 – 500nm can traverse far.

3.2.3 Module Characteristics

The instrumentation of the STRAW detector will consist of light emitters and light sensors. The light emitter is the successfully tested and deployed *Precision Optical Calibration Module* (POCAM) and acts as an approximately isotropic light source. The light sensor will be the *STRAW Digital Optical Module* (sDOM) which is a newly developed module for the STRAW project based on the design of the existing POCAM and will use 3" photomultipliers for light detection. Both modules will be described in the following chapters 4 and 5, respectively. In total, three POCAMs and five sDOMS were available for construction of the STRAW detector.

The wavelength range that can be investigated is severely dependent on the used instruments. For one, the pressure housing of both POCAM and sDOM use a glass hemisphere on each end to allow light emission or detection. As such, the optical properties of the glass will significantly influence possible wavelengths. Furthermore, the sDOM uses a PMT and its photocathode is only sensitive to photons of a certain wavelength range. Additionally, the PMT is optically coupled to the glass using optical gel which can disturb transmission especially towards the UV regime.

All of the instrument related properties are displayed in the upper graph of fig. 3.4 and suggest that reasonable transmission through the pressure housing glass and eventual detection is feasible from wavelengths upwards of 300nm. However, the detection efficiency of the sDOM will be affected by all of the mentioned components as well as the sea water itself. As such, the convolution of all sensitivities is visualized in the lower part of fig. 3.4. As of the latter and since an absorption length of the order of 50m is expected, the wavelength range was defined to be

$$350 \text{ nm} \leq \lambda \leq 600 \text{ nm} \quad (3.6)$$

with a focus on the UV and blue regime. This should enable feasible light detection of all sDOMs even when relatively large distances need to be covered.

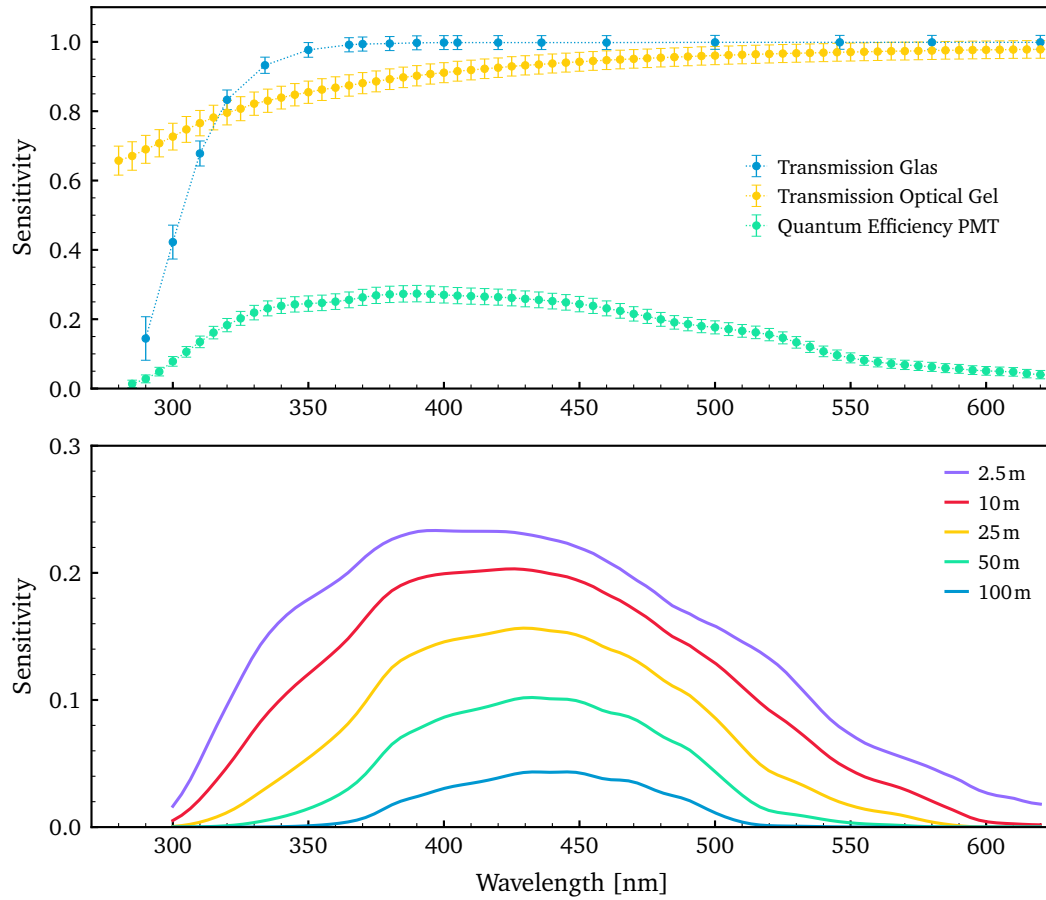


Figure 3.4: Spectral properties of the STRAW detector and its components. The upper graphic displays the spectral transmission of the pressure housing glass and the optical gel as well as the average quantum efficiency of the sDOM PMT. The lower plot shows the total sensitivity, i.e. convolution of all component sensitivities as well as expected water transmission for different distances. Additionally, the spectral ranges of the used LEDs in the POCAM are indicated. Data for the glass is from [106] and for the PMT from [20]. For the gel, samples have been measured using a UVVIS spectrophotometer. Details on the sDOM components can be found in chapter 5.

3.3 Detector Geometry

In total, three POCAMs and five sDOMs were available to act as light emitters and light sensors, respectively. As a result, a two-string geometry was chosen with four instruments each. This geometry does not only allow coverage of a potentially wide range of distances between modules but furthermore its symmetry allows for cross-checks and more importantly the option to perform relative measurements.

Nevertheless, the positioning of the instruments and the distance between both strings still required further investigation. First of all, the former was decided to be kept as equal as possible in order to keep the symmetry introduced by a two-string design. Additionally, since attenuation lengths of the order of 50 m are expected, ideally the following distance range would be covered from the instrument positioning

$$15\text{ m} \leq r \leq 100\text{ m} \quad (3.7)$$

which however would also be dependent on the distance of both strings.

As the timeline of STRAW did not allow for extensive design studies, the expected performance was estimated analytically. As discussed in chapter 4, the POCAM light emission is highly isotropic, especially for polar angles of $|\theta| \leq 60^\circ$. By assuming ideal isotropy and azimuthal symmetry, one can estimate the number of arriving photons at different sensor positions within the detector array, namely

$$N(r, \lambda) = \frac{N_0}{4\pi r^2} \exp\left(-\frac{r}{L_T(\lambda)}\right) A_{\text{active}} \quad (3.8)$$

with the total number of photons N_0 , the transmission length L_T and the active area of the sensor A_{active} . Simulations are currently underway which will not only inject the measured emission and acceptance profiles of the instruments but further will allow extraction of absorption and scattering lengths from the measured transmission lengths.

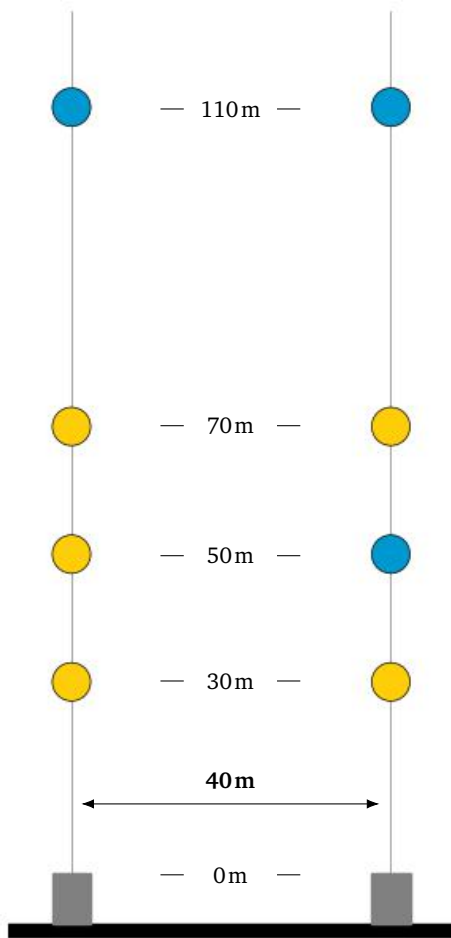


Figure 3.5: Geometry of the STRAW detector. POCAMs (blue) and sDOMs (yellow) in final positions with indicated distances.

in fig. 3.6 is the expectation of an isotropic POCAM emitting 1×10^9 photons/ 4π using LEDs with wavelengths that will be discussed in chapter 4. It achieves reasonable photon numbers at the various sDOM positions and probes a wide spectral range. While chapter 4 will show that the POCAM emission is highly isotropic and reaches intensities close to the necessary 1×10^9 photons/ 4π , the sDOM is expected to have an angular acceptance which decreases towards steep polar angles. As such, the expected number of detected photons is also significantly depending on the incident angle of the incoming light.

The fact that a symmetric detector should be constructed in combination with the availability of instruments narrowed down possible geometries. However, from a physics standpoint, the absolute positioning of the instruments and the inter-string distance remained free parameters. As such, they were used to cover the necessary distance range as well as estimate the photons arriving at each sensor using eq. (3.8).

Beyond physics, also technical limitations had to be considered. The first such was introduced by the deep-sea electrical connection cables. Since the sDOM is operated on Ethernet, its distance to the connection point on the seafloor can not be longer than 70m without risking to lose signal integrity over the used deep-sea copper cables. The same was the case for the serial connection of the POCAM where it was suggested by ONC that a maximum distance of 130m should be kept. Thus, the instruments have to be positioned below these respective distances from the seafloor. Another limitation was introduced by the operators of the remotely operated vehicle (ROV), namely that the strings could not be positioned closer than 40m relative to each other. The reason is a strict policy when it comes to deep-sea operations of ROVs and the risk of strings tangling up with the umbilical of the vehicle.

After estimations done using eq. (3.8) and iterating various geometries, eventually the design in fig. 3.5 emerged. With an inter-string distance of 40m and modules at heights of 30, 50, 70 and 110m the design covers distances between 20 – 90m. Displayed

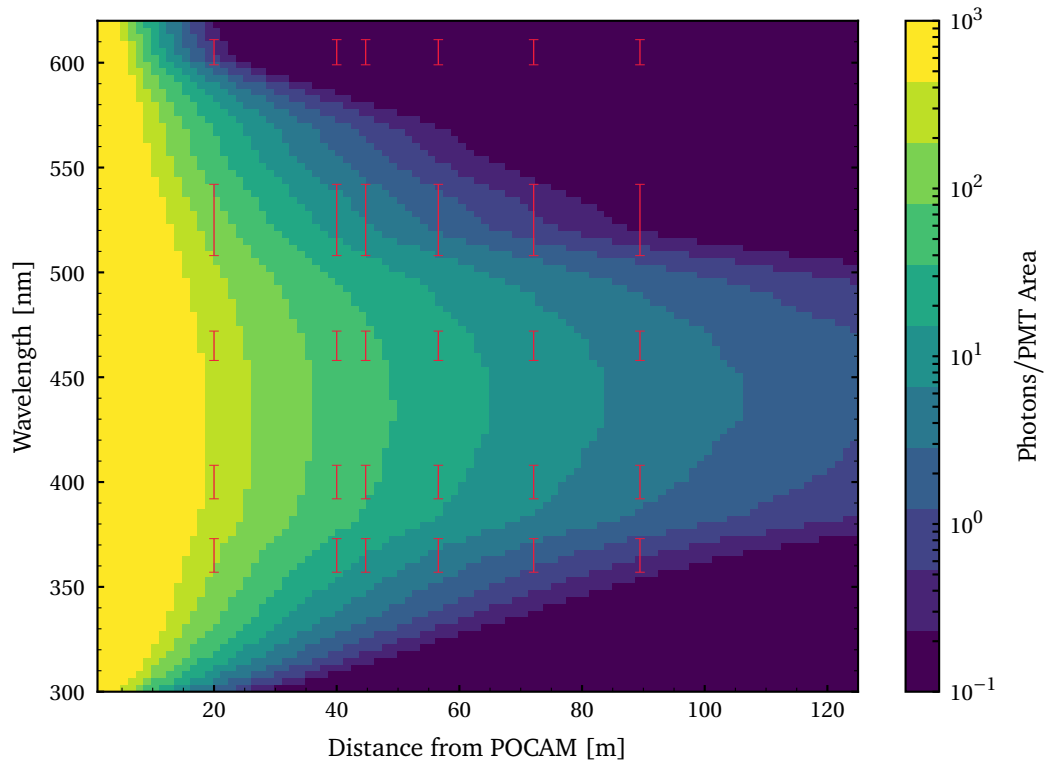


Figure 3.6: Photon number estimate of the STRAW detector geometry. The heatmap shows the number of expected photons on an sDOM PMT (color) with respect to distance (abscissa) and wavelength (ordinate). Indicated in red are the regions that will be probed by the STRAW geometry and LED configuration based on the FWHM spectral range of the LEDs that will be discussed in chapter 4. The underlying assumption is eq. (3.8) using an isotropic light emission of 1×10^9 photons/ 4π and the model of sea water by Smith and Baker [108].

4

Precision Optical Calibration Module

The *Precision Optical Calibration Module* (POCAM) was initially designed and is still intended to be used as a calibration device for the IceCube detector upgrade [14, 74]. Over the course of the last four years its functionality and design has improved and it will be used as light emitter in the STRAW array.

In this chapter, the POCAM concept, design and functionality will be discussed. After revisiting the prototype deployment in Baikal, the light emission characteristics of the POCAM will be discussed before closing with its role in STRAW.

4.1 Design

This section will outline the basic concept of the POCAM and explain the functionality and design of its components.

4.1.1 Concept

The POCAM was designed to act as a light emitting calibration device within IceCube to improve the understanding of the optical ice properties. Ideally, it would emit isotropic light flashes within the ice with known intensity. This could in turn be used to improve the calibration of local absorption and scattering properties. Furthermore, with known light intensity the individual DOM calibration and angular acceptance can be studied. This technique can in principal be used in any large scale neutrino telescope operating in an optical medium.

As such, the POCAM concept is to emit an isotropic, nanosecond light flash that is monitored and self-calibrated in-situ by integrated photosensors. The major objectives are to achieve a high level of intensity and isotropy with these flashes while keeping nanosecond timing. The former is necessary to homogeneously illuminate a large detector volume, the timing to allow differentiation between direct and scattered light. Furthermore, the internal calibration has to reach high precision in order to significantly improve systematic uncertainties of the detector. To illustrate the evolution of the POCAM design, a timeline is displayed in fig. 4.1.

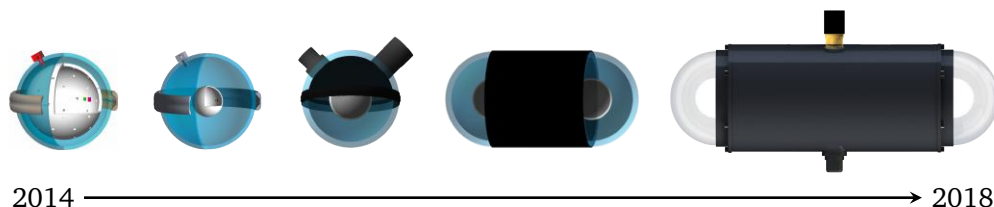


Figure 4.1: Timeline of the POCAM design evolution with the current design to the very right. The four images from the left are a courtesy of K. Holzapfel and A. Gärtner, respectively.

4.1.2 Housing

Since neutrino telescopes are usually located at great depths of water or ice, the housing of any instrument has to withstand the present pressure and ambient conditions. Most photosensor modules of such telescopes make use of glass pressure spheres in which the photosensors and electronics are encapsulated and protected.

Initially, this was also the idea for the POCAM. However, extensive simulations indicated that the POCAM light-emitting components should be small to avoid late photons caused by long path lengths [118]. Furthermore, due to necessary space for electronics, the encapsulation in a glass pressure sphere would allow undisturbed emission only from one hemisphere and would complicate the efforts necessary to achieve isotropic emission.



Figure 4.2: Current POCAM design.

A vacuum port allows for degassing and nitrogen-flushing of the instrument, which removes air and subsequently water. This greatly reduces the risk of condensation or electrical problems. The housing itself is kept at approximately 0.3 bar to also ensure sealing in low pressure water environments like test tanks. Lastly, electrical supply and control is enabled by a connector located in the center of the cylinder. According to Nautilus, this design will withstand an outer pressure of 1500 bar and temperatures down to -40°C . As will be discussed later, the housing was subjected to and passed a number of environmental tests.

4.1.3 Flasher Circuit

The flasher is the main active component of the POCAM as it is responsible for the light emission and all subsequent characteristics of the pulse. The general design of the flasher [83] originates from the one introduced by J.S. Kapustinsky in 1985 [75]. The *Kapustinsky flasher* is used for the POCAM in STRAW and its schematic is displayed in fig. 4.3.

It was in 2016 when the cylindrical POCAM was introduced. The idea was to generate much needed room for electrical and mechanical components in the cylinder and subsequently provide undisturbed emission from hemispheres located on either end. After the introduction of the idea, the designing of the first prototype started in collaboration with the deep-sea housing company *Nautilus*. After several iterations the design shown in fig. 4.2 was accepted for the prototype. The housing measures around 40 cm in length.

Due to an application in ice or the deep sea, the pressure housing has to withstand extreme ambient conditions, first and foremost high pressure and prolonged water contact. Here, the material of choice is titanium which therefore is also used for the POCAM housing. For the glass hemispheres, an optically enhanced borosilicate glass is used, namely *N-BK7* [106]. While quartz would be the material of choice for UV emission, chapter 3 has verified that BK7 is sufficiently transmissive in the relevant wavelengths of 350 – 600 nm, at greatly reduced cost. Additionally, borosilicate glasses are less prone to temperature shock damage, as they come with low thermal expansion which is beneficial for a possible application in IceCube-Gen2. The glass itself is attached to titanium flanges using deep-sea applicable epoxide resin.

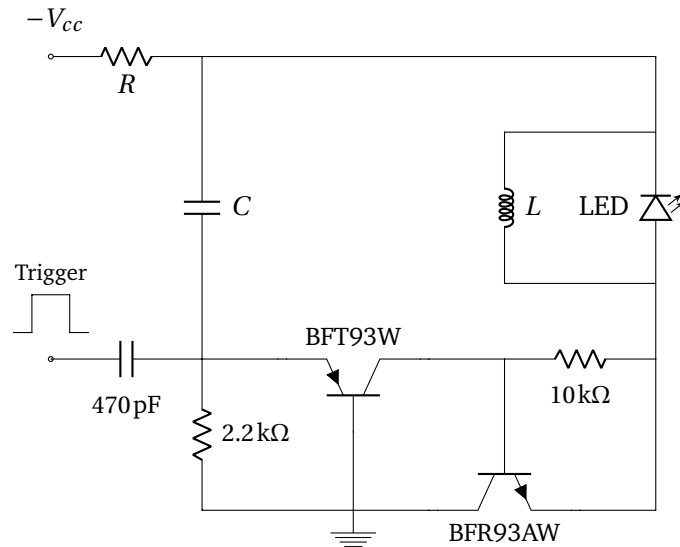


Figure 4.3: Kapustinsky flasher schematic for the POCAM in STRAW. The circuit is operated on negative bias voltage and produces a pulse when triggered with a square pulse signal. The light pulse is mainly shaped by the capacitor C and the inductance L as well as the LED itself.

The flasher circuit is operated with adjustable, negative bias voltage and produces a light pulse upon being triggered with a square pulse signal. Conceptually, once triggered, the capacitor C can charge up via V_{cc} and then discharge through the LED once the trigger opened the transistors and subsequently a low impedance path to ground. Upon current flowing through LED and inductance, the latter will counteract the current causing an oscillation that sweeps out charges from the LED. This effectively cuts the pulse and produces an intense but short light flash with a potential *full width half maximum* (FWHM) of only a few nanoseconds [83].

The exact shape and photon output of this pulse depends on the specific parameters of the capacitor C , the inductance L , the LED itself and the bias voltage. While the exact analytical behavior is complex, approximating the relevant part with an RLC circuit gives a frequency dependence of $1/\sqrt{LC}$. This means, larger inductances and capacitors should result in longer, brighter pulses which was studied and confirmed earlier in the POCAM development phase [42]. In the scope of this work, this was then used to optimize the flasher design of the POCAM in STRAW. Detailed discussions about this will follow in section 4.3.

As can be seen in fig. 4.4 for an early prototype of 2017, the current POCAM design includes six LEDs per hemisphere, four of which are driven by the Kapustinsky circuit. Two additional ones are driven by the control electronics but emit pulses of much longer width and as such only act as backup flashers. The purpose of multiple LEDs is to enable coverage of a wider range of wavelengths. However, their selection has to be studied extensively since they determine the light yield and timing characteristics of the flashes. Relevant wavelengths for current neutrino telescopes are in the range of 350 – 600 nm.



Figure 4.4: POCAM prototype LED layout.

4.1.4 Integrating Sphere

LEDs typically emit light into a cone with an angle dependent on the specific diode. As such, LEDs are disadvantageous for the precise calibration of local optical properties if their orientation is not known precisely.

To resolve this, the initial idea of the POCAM was to produce an isotropic light pulse by making use of an *integrating sphere*, that is, a sphere made from a *Lambertian* or *diffuse reflector* which integrates light within its volume and homogeneously illuminates each surface element. This technique is well known in fields like spectrophotometry, but is used to integrate spatial flux from an external light source and not to isotropize the output of an internal one.

A common integrating sphere makes use of the Lambertian reflectance of a surface. That is, incident light perpendicular to the surface will be scattered diffusely in all directions so that

$$I(\theta) = I_0 \cos(\theta) \quad (4.1)$$

For arbitrary surfaces, the flux incident on an infinitesimal surface element depends on its orientation with respect to other elements. For instance, following integrating sphere theory [72], the fraction of energy scattered off of a diffuse surface element dA_1 and arriving on a second one dA_2 is given by

$$dF_{12} = \frac{\cos(\theta_1) \cos(\theta_2)}{\pi S_1 S_2} dA_2 \quad (4.2)$$

with distance S_i and angles θ_i with respect to the surface normals.

With arguments arising from spherical symmetry, this reduces to

$$dF_{12} = \frac{1}{4\pi R^2} dA_2 \quad (4.3)$$

which is constant for every surface element independent of incident angle or distance. This means that a perfectly diffuse reflecting integrating sphere homogeneously distributes incoming light on the internal surface. However, this requires absolute and diffuse reflection and hence no absorption or transmission, a deviation of which will alter the integrating behavior.

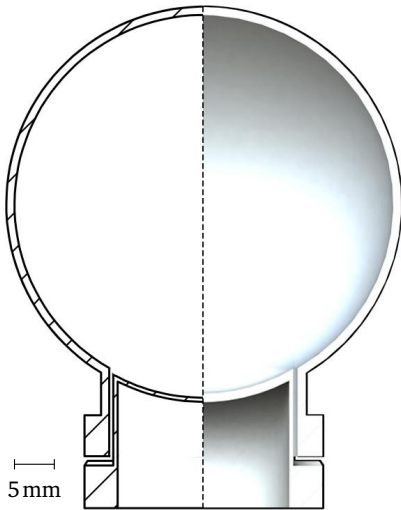


Figure 4.5: Two-component POCAM integrating sphere geometry.

The POCAM isotropy study started in 2015 with a number of extensive simulations of different sphere geometries [118]. As a result, the consensus was to pursue what is called a *semi-transparent sphere* which makes use of a diffusely reflective material that still allows a significant fraction of photons to pass and exit the sphere at each reflection. Since all internal surface elements should experience the same illumination, the spherical symmetry will ensure isotropic emission from the sphere exterior. The optical material of choice is *polytetrafluorethylene* (PTFE) which is a commonly used diffusor [55].

While the realization of the first sphere prototype took several iterations, eventually the current geometry in fig. 4.5 emerged, based on the design by K. Holzapfel, master student within the team. It consists of two PTFE parts, the main sphere and a plug. The concept of the design foresees the plug to complete the internal sphere and hence allows for homogeneous integration of light. Furthermore, the LED emission is not coupled directly into the sphere, but pre-diffused through a thin layer of teflon in the plug. This helps in losing the initial direction of the LED emission and its angular profile. Notably, the main sphere surface used for light emission is completely free from disturbances.

The initial dimensions were based on [118] and the investigation of the transmission properties of the used PTFE. A detailed study of the isotropy achieved with this geometry will follow in section 4.3.4.

4.1.5 Photosensors

As a calibration device, the main focus of the POCAM was to precisely monitor its light output internally and independently from the detector. To achieve this, in the current design each hemisphere includes two types of photosensors which ensure in-situ calibration. One type of sensor is a common *photodiode* with a large area that is linear over many orders of magnitude in incoming flux. Secondly, a *Silicon-Photomultiplier* (SiPM) is integrated which is sensitive down to single photons and was initially planned to measure low-light fluxes.

The current read-out of the sensors does not acquire the pulse shape of its response to light, instead the charge output is measured using a sensitive charge-amplifier. The response of the latter is then amplified and fed to an *analog-to-digital converter* (ADC) that digitizes the signal. The amplitude of this pulse is then used to determine the total charge from each sensor which in turn enables the extraction of the exact light output of the flash. Details on the calibration and analysis done for the POCAM in STRAW will follow in section 4.3.5.

4.1.6 Electronics

The POCAM electronics development was led by the resident electrical engineer and STRAW member. M. Boehmer, who was also in charge of designing and producing new STRAW electronics that will be discussed later.

The POCAM electronics consist of three major components: the analogue board, the digital board and the power board. The analogue board hosts the flasher circuits, the LEDs and photosensors including their amplifiers. It is responsible for the light output and valid sensor data. The digital board contains a *field programmable gate array* (FPGA), a microcontroller and storage and handles all internal processes, the data acquisition (DAQ) as well as external slow control. The power board mediates external to internal voltage and distributes the communication to each hemisphere. While only one power board is located in each POCAM, both hemispheres contain analogue and digital boards and can be operated synchronously or individually. Additionally, each hemisphere includes an accelerometer and a magnetic field sensor which in turn allow for precise determination of the POCAM orientation.

4.1.7 Internal Mounting

The last aspect of the POCAM is its assembly and the internal structure to securely mount all components. As the housing is of cylindrical shape, the electronic boards have a circular design and are stacked inside the cylinder, attached to the flanges.

Furthermore, each side contains an integrating sphere that isotropizes the LED flashes and a *shadow* which aligns the integrating sphere and takes care of providing fixed solid angles to the photosensors. Since not only the insides of the flanges but also the shadow itself are painted black with a special, low-reflective spectrometer paint, internal reflections are reduced to a minimum. The shadow also blocks possible stray light exiting from the neck of the integrating sphere. The structure of an exemplary POCAM hemisphere is shown in fig. 4.6.

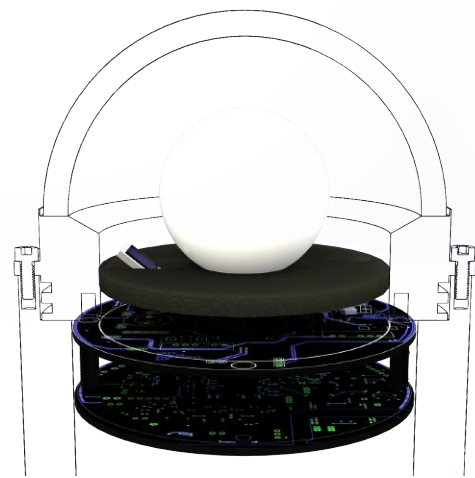


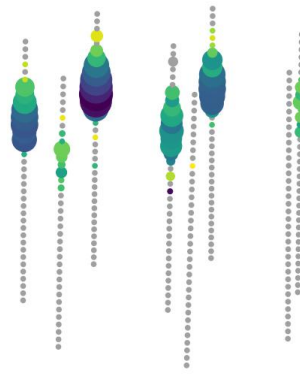
Figure 4.6: Internal mounting, shadow and photosensor layout of a POCAM hemisphere.

4.2 Prototype in Baikal

The first POCAM prototype was built in late 2016 in the scope of a possible deployment in one of the clusters of the GVD neutrino telescope in Lake Baikal. In early 2017, the POCAM was successfully deployed and installed within a GVD cluster during detector construction and outside temperatures of around -20°C . It was then lowered to a depth of approximately 1.1 km and successfully operated over the course of the remaining year.

While the detailed study of this prototype and subsequent results within the finished clusters of GVD is subject of another ongoing master's thesis, a brief overview shall be given. Furthermore, the knowledge and experience gained during characterization of the prototype flasher for Baikal were the first step towards the optimized version resulting from this work and which are now integrated in STRAW.

Figure 4.7a shows the installation of the POCAM to the string of a cluster of the GVD detector, fig. 4.7b an exemplary event view of a high-intensity POCAM flash within the cluster. A detailed study of the optical properties using the POCAM operation is currently underway, however, preliminary analyses suggest an absorption length of around 20m between 470 – 520nm, well in accordance with measurements by the Baikal collaboration [28, 40].



(a) POCAM installation on a GVD string. (b) Event view of a high-intensity POCAM flash.

Figure 4.7: (a) Z. Dzhlkibaev (GVD) and the author during the installation of the POCAM to a string within the GVD cluster, taken by J. Thompson. (b) Simple event view of a POCAM flash within the cluster. Size represents charge and color arrival time from early (purple) to late (yellow). For reference, the horizontal string spacing is 60m, the module spacing 15m. Data is a courtesy of the GVD collaboration.

The POCAM prototype design deployed and operated within GVD contained some differences with respect to the current design. Most notably, different LEDs with fewer wavelengths were used and the flasher voltage could not be adjusted. That meant, the intensity of the flashes was fixed only at medium light output. In fact, in combination with the present water properties at Lake Baikal, this caused Kapustinsky flashes to be detected only by neighboring strings. As a result, runs with the high-intensity backup flashers with much longer pulses and more photon output were carried out as well. As such, they were seen further inside the cluster, however, at the cost of losing timing resolution of the photon arrival time.

Most importantly however, the POCAM was successfully deployed and operated in extreme conditions. Furthermore, it survived the low temperature exposure during installation on Lake Baikal and remained in stable operating mode over the course of one year in a depth of 1.1 km. The success of this operation confirmed the feasibility of a possible IceCube deployment and remains unprecedented by other possible calibration devices for IceCube-Gen2 to date.

4.3 Light Emission Characteristics in STRAW

This section will treat and analyze the light emission characteristics of the POCAM for STRAW in detail. Before investigating the pulse characteristics, the flasher configuration will be discussed. Thereafter, the isotropy and the internal calibration will be analyzed.

4.3.1 Flasher Circuit Configuration

As was defined in chapter 3, the wavelength range of emission should ideally cover a wavelength range of 350 – 600nm to cover the major fraction of Cherenkov spectrum in water. However, the response of LEDs of different wavelengths usually differs significantly due to different semiconductors and production processes.

While the qualitative behavior of the circuit was understood, it became clear that the LED itself forms the main component affecting the actual output pulse, especially its timing. Hence, it was decided to first define the flasher configuration so that sufficient light yield and acceptable timing are achieved for LEDs with a wavelength of 470nm which were noticed to behave widely similar due to the used semiconductors. Afterwards, the choice of LEDs for the remaining spectral ranges should be optimized. In fig. 4.8 a selection of these measurements is visualized that eventually resulted in the final STRAW flasher configuration

$$R = 10\text{k}\Omega \quad C = 1.2\text{nF} \quad L = 22\text{nH} \quad (4.4)$$

As will be seen, this produces sufficient light characteristics in the relevant spectral region.

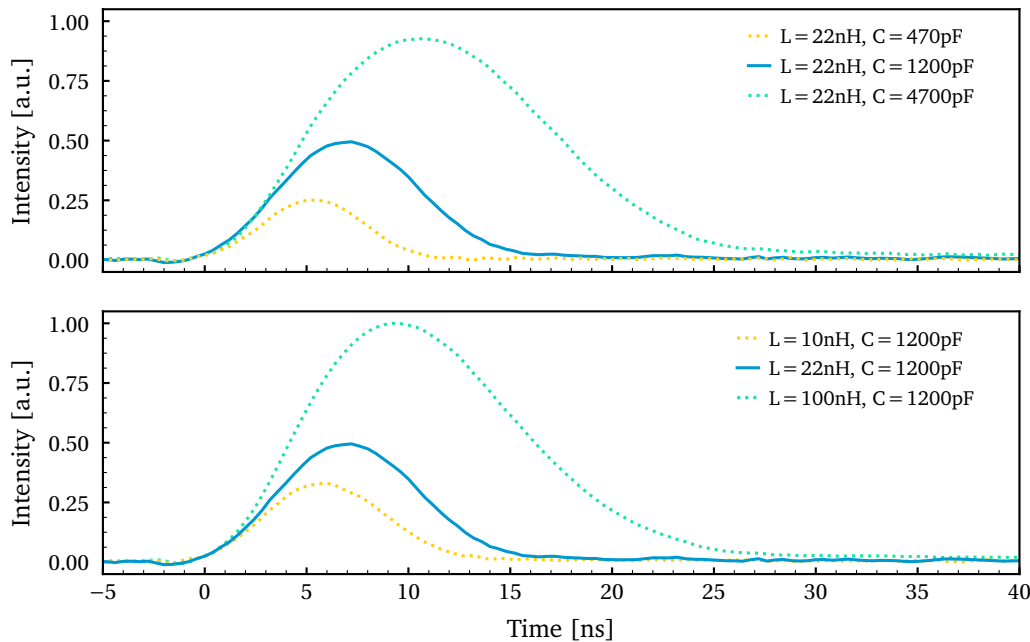


Figure 4.8: Exemplary Kapustinsky behavior for different capacities (top) and different inductances (bottom). In both cases, the respective other value was fixed. Measurements were done using a fast photodiode of < 1 ns rise time which enables approximately observing the real photon pulse shape. The LED of choice for these measurements was a fast 470nm diode. As expected, it is clearly visible that the pulse intensity and width increased for increased L and C .

In total, the light outputs and timing characteristics of over 50 LEDs have been investigated to find the ideal setup for STRAW. The process of selection and the in-depth analysis of the final pulse characteristics will be subject of the remaining section.

4.3.2 LED Selection

Since neutrino telescopes instrument very large volumes, the photon yield of a light emitting calibration device has to be significant in order to illuminate a reasonable number of photosensors. Furthermore, the pulse has to be short in time in order to differentiate between direct and scattered light. Consequently, the selection of flasher LEDs should be done carefully and precisely. For the POCAM in STRAW, these measurements will be outlined in the following.

Intensity

In order to measure the intensity of different LED pulses comparably, an integrating sphere was mounted on top of a flasher board identical to the one inside the POCAM. Then, the orientation of the flasher was mechanically fixed facing a calibrated, large-area photodiode in photovoltaic mode which linearly measured the light output using a picoammeter. Importantly, due to the integrating sphere and the fixed distance, the photodiode solid angle was identical for all LEDs independent of their opening angles. As shall be seen later, this is a very good assumption.

Using the photodiode calibration data, it was in turn possible to determine the relative, wavelength-independent light yield of all LEDs. The results of these measurements are presented for different wavelength ranges in fig. 4.9 and furthermore suggest linearity of the flash intensity over a wide supply voltage range. While most of the UV, blue and orange LEDs achieved reasonable light yield, all tested green LEDs showed very poor light yield.

Besides, it was discovered that in some cases also multiple LEDs could be operated in parallel to one inductance in the flasher circuit. In case of such a functioning LED *multiplicity*, the light output could be increased without interfering with the timing of the pulse, as will be seen shortly. However, this was limited by the form factor of the diodes and the available space on the flasher board.

Timing

To get a handle on the timing performance of all the LEDs, a photomultiplier was observing the integrating sphere through an attenuator, in parallel to the intensity measurements. Due to the defined position of the flasher, also the PMT solid angle was the same over the course of all measurements. The PMT of choice was the same model also used in the STRAW sensor module, which will be discussed in detail in chapter 5.

The PMT response pulse is a convolution of its internal charge response and the light pulse. However, the PMT was observing the pulse strongly attenuated and with a small solid angle and hence it was responding to low amounts of light over the course of all measurements. As of the latter, it is reasonable to assume that the increase of its internal charge response with larger pulse intensities is non-dominant and hence the output pulse shape is primarily determined by the light pulse itself. That means, extracting the PMT response FWHM allows to draw relative comparisons between the pulse widths of different LEDs.

Output pulses of the PMT were recorded with a gigasample oscilloscope and their FWHMs were extracted. The subsequent results for the various wavelength ranges are also visualized in fig. 4.9 and indicate first and foremost that both UV and blue LEDs achieve stable and fast FWHM responses from the PMT. At the same time, timing becomes an issue for most of the orange and all of the green LEDs. Additionally, green all green LEDs showed pulses with very long tails and as such will not be used on the Kapustinsky slots of the POCAM. After investigation this seemed related to the used semiconductor properties but was not further investigated.

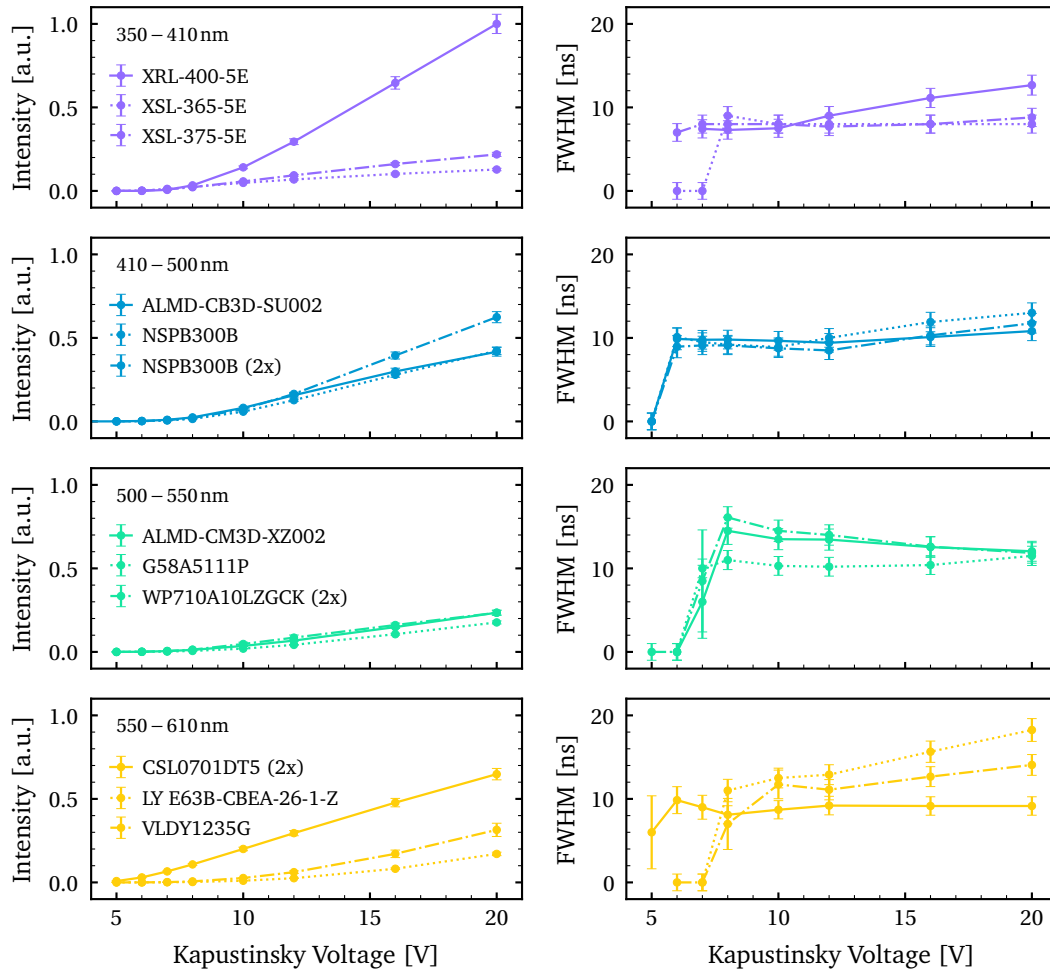


Figure 4.9: Selection of POCAM LEDs. Shown are measurements of intensity (left) and timing (right) for selected LEDs of UV, blue, green and orange wavelengths (from top to bottom). The intensity scale has been normalized and corrected for the quantum efficiency of the photodiode at different wavelengths and so is identical for all LEDs. For the timing measurements FWHMs of an observing PMT were measured. As explained in the text, this is primarily shaped by the incident light pulse. The included errors include statistical and reasonably estimated systematic uncertainties. The latter arise mainly from the precision of the orientation (5%), the photodiode calibration (3–5%) and the intrinsic time resolution of the PMT (~1 ns).

The results of the intensity and timing measurements now allowed the selection of LEDs to be used in the POCAM for STRAW. The final selection and some characteristics are visualized in table 4.1, the final LED layout in fig. 4.10. With the chosen violet LED outperforming all others, it was further decided to host UV, blue and orange LEDs on the Kapustinsky flashers, all in their best possible multiplicity configuration. As such, green LEDs were omitted for the fast flasher slots due to their generally weak performance.

However, since the green spectral region is important for the detection of Cherenkov light, green LEDs will be used on the backup flasher slot, controlled by the FPGA in the POCAM.

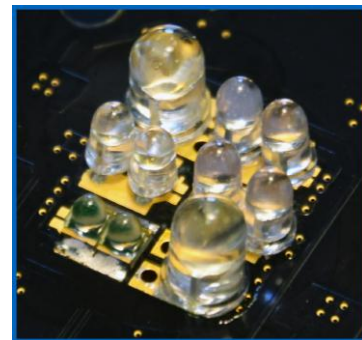


Figure 4.10: STRAW flasher LED layout with multiplicities.

The second such available slot will be occupied by a backup pair of blue LEDs. While these slots can not be used for precision timing measurements due to their long pulse lengths, it is still possible to probe the green spectral region in terms of absorption.

LED	Color	Spectral Range [nm]	Relative Intensity	Kapustinsky	FPGA
XSL-365-5E [124]	UV	365 ± 8	0.13	1x	–
XRL-400-5E [123]	Violet	405 ± 8	1.00	1x	–
NSPB300B [109]	Blue	465 ± 7	0.62	2x	2x
WP710A10LZGCK [121]	Green	525 ± 17	0.23	–	2x
CSL0701DT5 [49]	Orange	605 ± 6	0.65	2x	–

Table 4.1: Final selection of the six POCAM LEDs for STRAW. Given are the LED part names, their given FWHM spectral ranges, their calibrated, relative intensities at 20 V Kapustinsky voltage and their multiplicities on the Kapustinsky and FPGA flashers, respectively.

4.3.3 Light Pulse

In order to analyze experimental data from the STRAW detector precisely, the pulse shapes of the POCAM flashes have to be known in detail. Especially for extracting scattering properties, it has to be clear in what time interval photons are expected to arrive. This section will investigate the stability of the light pulse shape and its dependence on voltage.

In order to observe the actual photon pulse shape of different LEDs, a fast Silicon-PIN-photodiode was used which responds with a rise time of around 1 ns to an incident light pulse. Since the response of any direct light detector is the convolution of its internal response $g(t)$ and the shape of the light pulse $f(t)$, that is,

$$I_{\text{obs}}(t) = f(t) * g(t) = \int_0^t f(\tau) g(t - \tau) d\tau \quad (4.5)$$

knowing the internal detector response allows numerical deconvolution and hence extraction of the photon pulse shape. For the photodiode, the former is achieved by illuminating it with a 405 nm laser with picosecond pulses and recording the diode response, as seen in fig. 4.11.

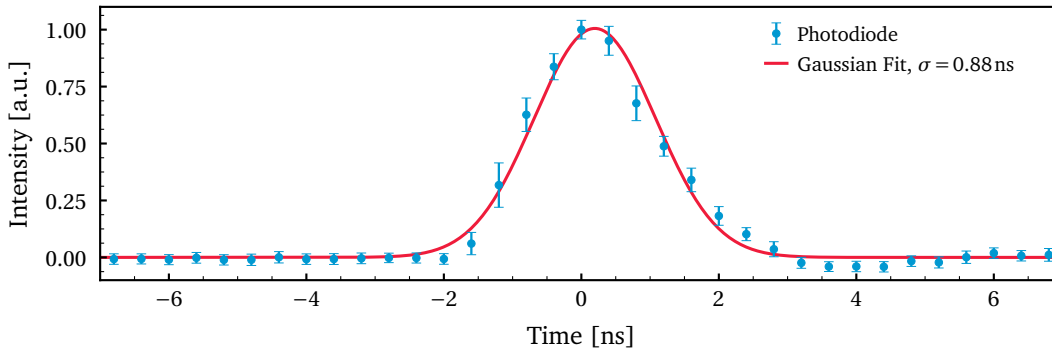


Figure 4.11: Photodiode response to a 50 ps laser pulse revealing its internal impulse response. In addition to the measured pulse, a reasonable Gaussian fit to the signal is depicted.

With the response from the photodiode confirmed to be approximately Gaussian, all pulse shapes of the selected POCAM LEDs were measured. This was done in order to extract the photon pulse shape and its variability with changing supply voltages of the flasher circuit. As can be seen in fig. 4.12, the vast majority of LED pulses observed this way can also be well approximated with a *normal* or *Gaussian distribution*, i.e.

$$G(x|\mu, \sigma) = G(\mu, \sigma) = \frac{1}{\sqrt{2\pi\sigma^2}} \exp\left(-\left(\frac{x-\mu}{\sqrt{2}\sigma}\right)^2\right) \quad (4.6)$$

However, due to being close to the flasher, effects of the Kapustinsky trigger noise affect the diode signal and hence the quality of the fit to the data in its tail regions. Nevertheless, the extracted pulse widths of the fits resemble the data well.

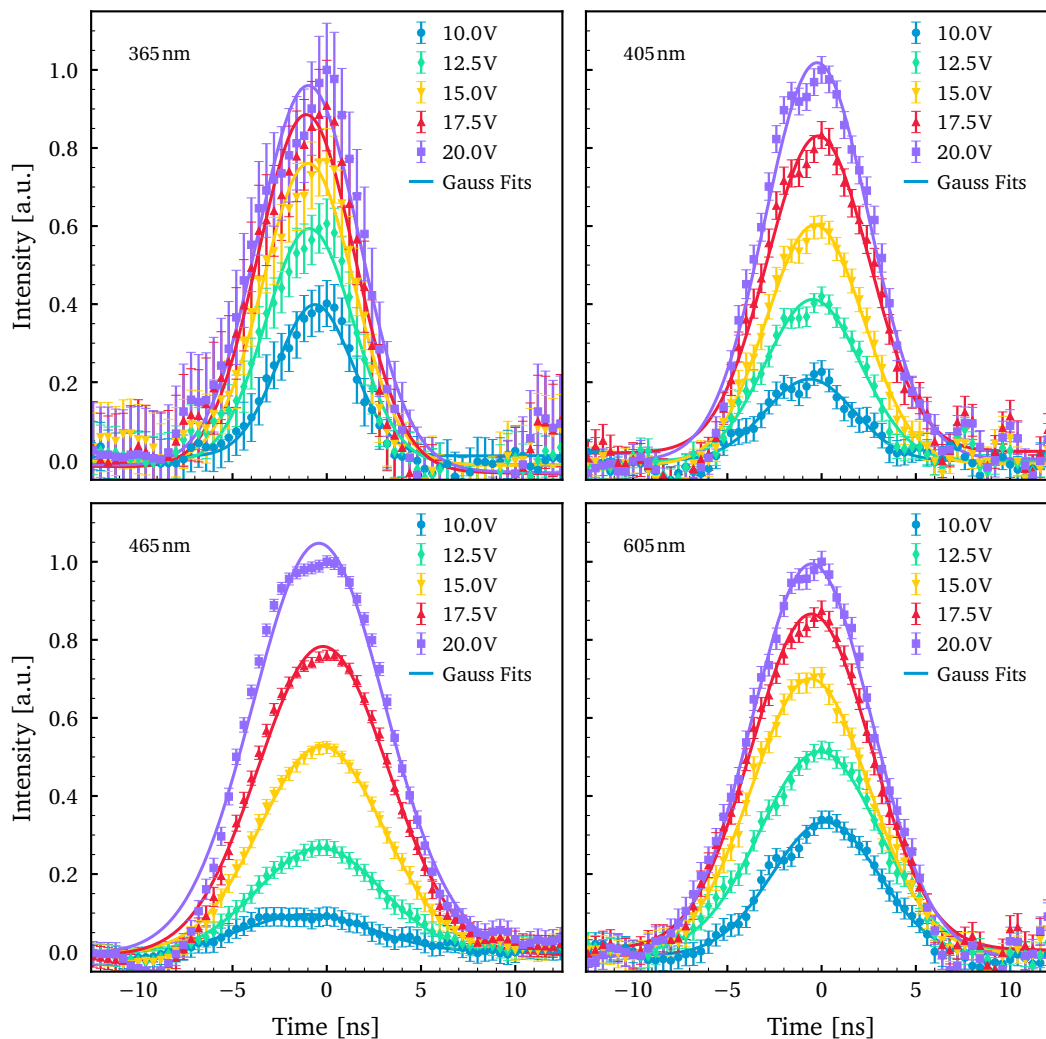


Figure 4.12: Pulse Shapes of POCAM LEDs. Shown are measured signals of a fast photodiode with incident pulses from the POCAM LEDs of 365nm (top left), 405nm (top right), 465nm (bottom left) and 605nm (bottom right) with varying Kapustinsky supply voltages. Notably, the low quantum efficiency of the diode towards small wavelengths causes weak signal-to-noise ratios in the UV and violet measurements. Additionally, Gaussian fits to the signals are indicated. Their occasional mismatch in the tail regions indicates a disturbing effect of the trigger noise on the photodiode signal induced by the flasher circuit in close proximity.

While the last step would be the deconvolution of the photodiode response, a useful mathematical relation can be used instead. Since both the diode response and the light pulse are approximately Gaussian, their convolution will be as well. Formally it is

$$G_{\text{exp}}(\mu_{\text{exp}}, \sigma_{\text{exp}}) = G_1(\mu_1, \sigma_1) * G_2(\mu_2, \sigma_2) = G\left(\mu_1 + \mu_2, \sqrt{\sigma_1^2 + \sigma_2^2}\right) \quad (4.7)$$

In turn, eq. (4.7) enables to correct for the photodiode response via

$$\sigma_{\gamma} = \sqrt{\sigma_{\text{exp}}^2 - \sigma_{\text{PD}}^2} \quad (4.8)$$

The FWHM of the pulses is then extracted by extracting the parameters of the fits to the measured pulses and making use of the relation

$$\text{FWHM}_{\gamma} = 2\sqrt{2\ln(2)} \sigma_{\gamma} \quad (4.9)$$

The results of the latter are illustrated in fig. 4.13 and show average pulse widths between 5 ns (UV) to 7.5 ns (blue). Furthermore, it suggests reasonable pulse stability with the flasher supply voltage. Except for the UV, linear fits to the measured FWHMs demonstrate a relatively weak dependence on the flasher voltage.

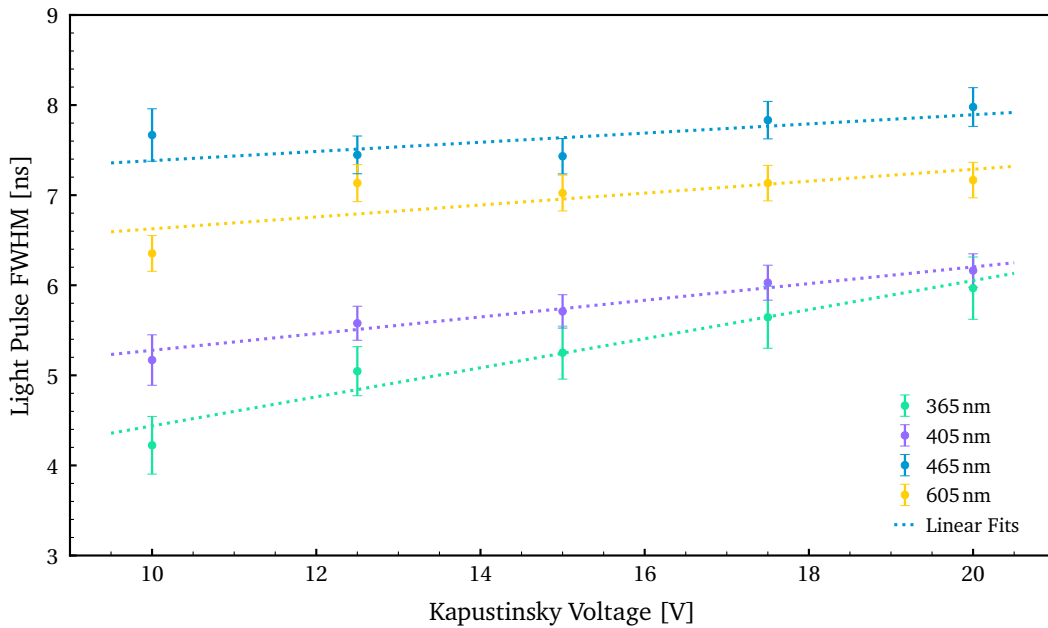


Figure 4.13: Full width half maxima of the POCAM LED flashes with respect to the flasher voltage. Illustrated are the extracted FWHMs of the LED flashes observed and corrected for a fast photodiode together with linear fits. Except for the UV LED, the voltage dependence of the pulse width is weak.

Frequency Stability

Before moving on to the study of the POCAM isotropy, the frequency stability shall be investigated. The measurement was done using the previously discussed calibrated photodiode and observing its output current at varying frequencies. Since the diode was used in photovoltaic mode, the relative light yield Q per pulse and LED is determined via

$$Q = \frac{\text{Current} - \text{Background}}{\text{Frequency}} \quad (4.10)$$

As can be seen in fig. 4.14, the critical frequency is reached for about 10 kHz. For lower frequencies, the different LEDs reveal intensity stability below 1% with the only exception being the UV diode, which drops around 9% up to 10 kHz. In general however, above this critical frequency the pulse intensity becomes unstable. It appears, the main reason is that the charge-providing capacitor C can not charge up sufficiently anymore before being triggered.

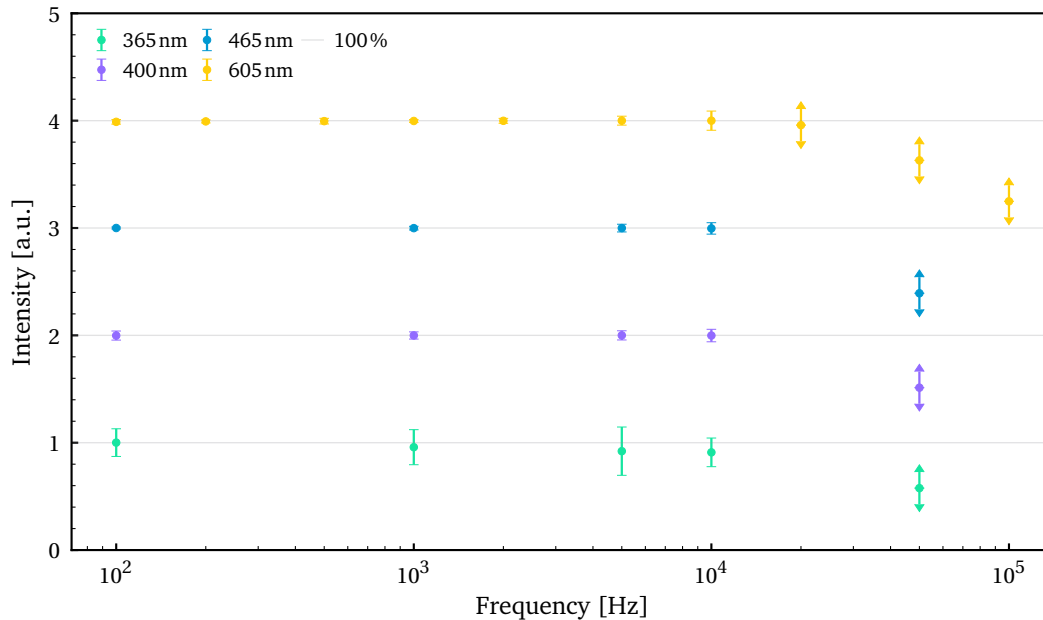


Figure 4.14: Frequency stability of the POCAM flasher. Included are the measured intensities of UV, violet, blue and orange LEDs with respect to the flasher frequency, each was iteratively offset by one for better visualization. Also indicated are the respective constant intensities with a faint grey line. Again, the low quantum efficiency of the photodiode in the UV visibly affects measurements of the 365 nm LED. The flasher voltage was fixed at 20V for all LEDs.

4.3.4 Isotropy

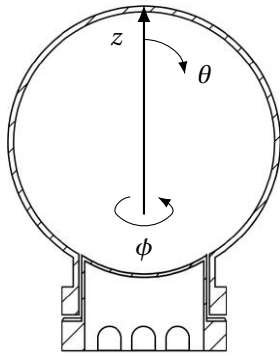
One of the main design goals of the POCAM is its isotropic emission. As such, the investigation of the angular emission profile is of major importance also for its role in STRAW since it determines the expected amount of light at different sensor positions within the detector.

This section will first treat the emission profile of the pure integrating sphere and the influence of different LED profiles. Afterwards, the theoretical and measured isotropy of a POCAM hemisphere are discussed and compared.

Integrating Sphere

As discussed in section 4.1.4, the integrating sphere is responsible for isotropic emission from the POCAM. Furthermore, it should enable similar emission profiles independent of different LED opening angles by diffusing the initial pulses through a thin layer of PTFE in its plug.

Emerging from previous design studies [118] and further tests in the scope of Bachelor theses during the POCAM prototype design phase, the current integrating sphere design foresees a diameter of 50 mm and a thickness of 1 mm. The latter also counts for the plug, i.e. the PTFE window pre-diffusing the LED pulse. The optical properties of PTFE in that regime should enable homogeneous light integration and thus uniform illumination of the sphere exterior.



For the measurement the integrating sphere emission profile, the integrating sphere, in combination with a POCAM flasher board, was placed on two optical rotation stages. In the previously defined distance, a calibrated, large-area photodiode in photovoltaic mode of was placed, aligned with the z-axis of the sphere. The rotation stages were then used to automatically scan the angular coordinates indicated in fig. 4.15. The photocurrent of the diode was then measured using a Picoammeter and wavelength correction of the quantum efficiency was performed with calibration data. The azimuthal and polar angles will from hereon be called ϕ and θ , respectively.

Figure 4.15: *Isotropy scan coordinate system.* Before conducting the isotropy scan of the sphere emission, the *inverse square law* is used to determine a proper distance at which the sphere can be reasonably well approximated as a point source. The former relates the intensity of a point light source to its distance r as

$$I(r) \propto \frac{1}{r^2} \quad (4.11)$$

and can be used to study at which distance the point source approximation of the integrating sphere holds and hence should be used for the isotropy measurements.

The results of these precursor measurements are displayed in fig. 4.16 and confirm that a distance around 75 cm gives reasonable results. To further increase the signal-to-noise ratio of the isotropy measurements and due to the relatively small deviation of the point source behavior at 50 cm, a final distance of 65 cm was defined for all subsequent measurements.

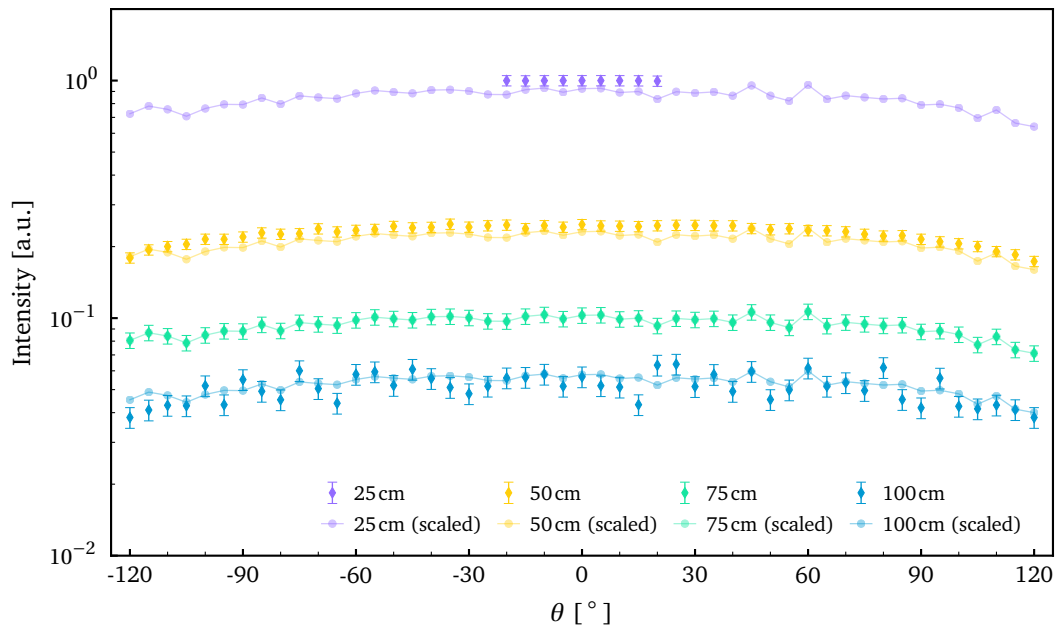


Figure 4.16: *Point source validation measurement.* Shown is the relative photodiode current at 25, 50, 75 and 100 cm distance in a polar angle range of $|\theta| \leq 120^\circ$ and fixed ϕ . Assuming point source validity at a distance of 100 cm, the reference measurement at 75 cm was scaled to other distances using eq. (4.11). While this fits the assumed point source behavior at a distance of 100 cm, the shorter distances do not match as well. The noise on the 100 cm signal is related to the weak diode current. The given errorbars include statistical and systematic uncertainties.

Now, with prerequisites of the measurement defined, the isotropy scan was carried out. As seen in fig. 4.17, the measurement itself was automatized, that is, the optical rotation stages were sweeping a defined range of angles to cover every emitting solid angle of the sphere. At each position, the photodiode current was measured using a Picoamperemeter. Data was taken for the LED switched on and off in order to eliminate possible background. In photovoltaic mode, the latter would be caused by e.g. stray light in the setup or a wrong baseline in the amperemeter, however, both would be eliminated by measuring and subtracting the background at each position.

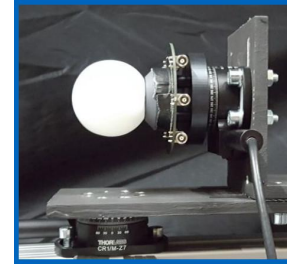


Figure 4.17: *Isotropy scan measurement setup.*

Exemplary data obtained from measurements using an integrating sphere from the POCAM prototype and one of its LEDs is shown in fig. 4.18. First of all, it is clear that the sphere emission is relatively homogeneous in the polar range of $|\theta| \leq 90^\circ$. Notably, deviations in ϕ are relatively small and suggest a good production quality of the sphere and its achieved uniformity. In fact, sphere-to-sphere deviations were not expected and have proven to be negligible ($\leq 1\%$) due to the fully automatized production process using a high-precision CNC mill. However, at the same time it is also visible that not all the initial direction of the light pulse is lost, as the peak emission is reached when directly facing the LED. The steep decrease observed for $|\theta| \geq 110^\circ$ is caused by the flasher setup disturbing and eventually blocking the light path to the diode. In general, these results are promising, not only because of the isotropy achieved from the upper hemisphere, but more importantly by providing proof of concept of the light integration.

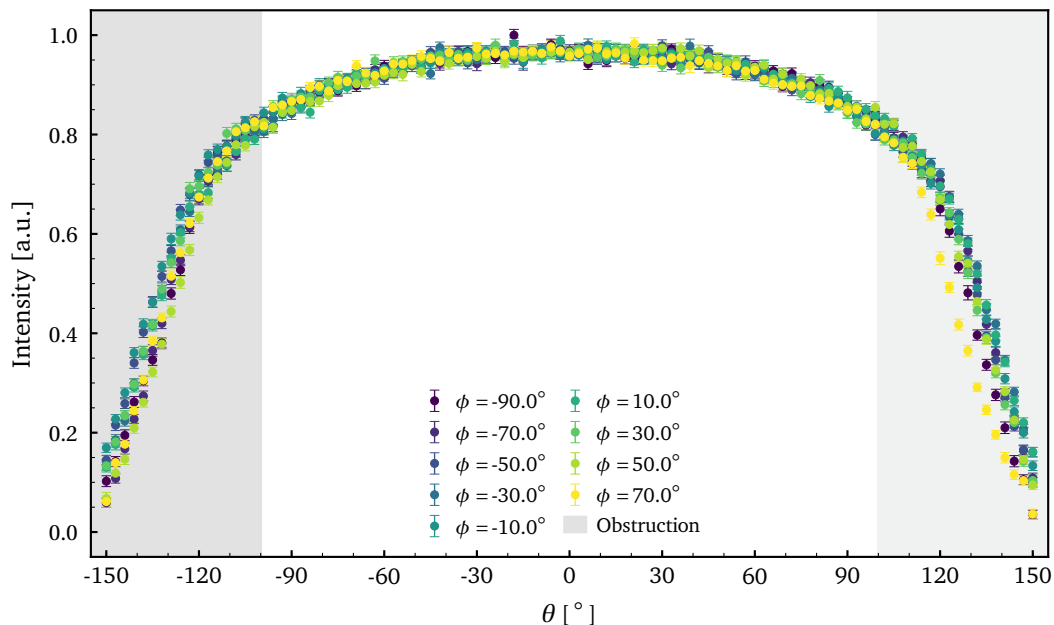


Figure 4.18: *Isotropy scan of a POCAM integrating sphere. Shown is the normalized, corrected photodiode current with respect to polar angle. The data indicates that there is deviation in ϕ , however, in the percent regime. The polar angle range of $|\theta| \leq 100^\circ$ shows only small deviations from isotropic emission. At larger polar angles the flasher setup begins to significantly disturb the field of view to the sphere. Also here, included uncertainties are statistical and systematic.*

Now, first of all it is possible to describe the spread in ϕ by averaging all measured values and as such quantify the uniformity of the sphere in azimuth. As visible in fig. 4.19, this confirms sufficient azimuthal uniformity. Accounting for sphere-to-sphere deviations, a mean spread of $\Delta I_\phi = (4.72 \pm 0.30)\%$ is achieved in a polar range of $|\theta| \leq 100^\circ$.

More importantly however, fig. 4.19 suggests that the achieved emission profile is independent of the LED viewing angle. That means, very narrowly emitting LEDs are not disfavored as would be expected on first glance. Hence, the PTFE integrating sphere does not only isotropize the light pulse but helps in losing the emission profile of the LED and in combination with the weak wavelength dependence of PTFE [55] allows it to be used with effectively any LED.

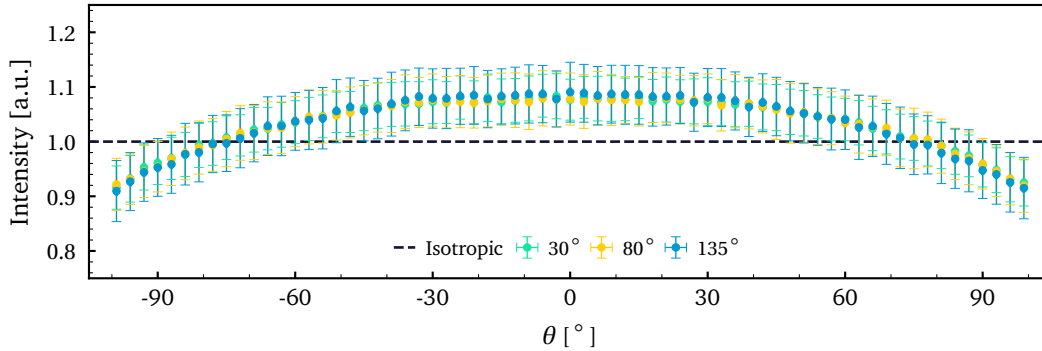


Figure 4.19: Polar isotropy of the integrating sphere covering the range $|\theta| \leq 100^\circ$ for various LED viewing angles. Shown is the normalized intensity averaged over measured ϕ angles, with respect to θ . The plot has been centered around the mean of its minimum and maximum and suggests that the LED opening angle does not influence the resulting emission profile. The errorbars take into account the spread introduced by different azimuthal angles, as well as statistical and systematic uncertainties from the measurement.

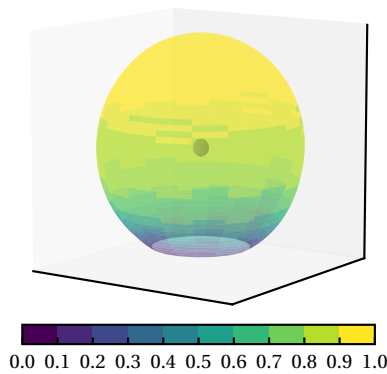


Figure 4.20: Integrating sphere (grey) and its emission visualized in 3D.

While these results are very promising, the obstruction from the measurement setup did not allow the investigation of larger angles at this time. This will be solved by a second-generation setup, currently in development and production.

POCAM

As has been discussed already in section 4.1, the POCAM design foresees two hemispheres to act complementary in achieving isotropic emission. As such, the high isotropy observed in the polar range of $|\theta| \leq 90^\circ$ already provides grounds on the preliminary assumption that reasonable isotropy can be achieved using the POCAM. While a high-precision study of the POCAM emission is still ongoing, preliminary results in air are displayed in fig. 4.21. The latter were done in order to verify the POCAM applicability in the scope of the STRAW project and to verify the theoretical background as well as simulations. As seen in the preliminary data, both is well within expectation.

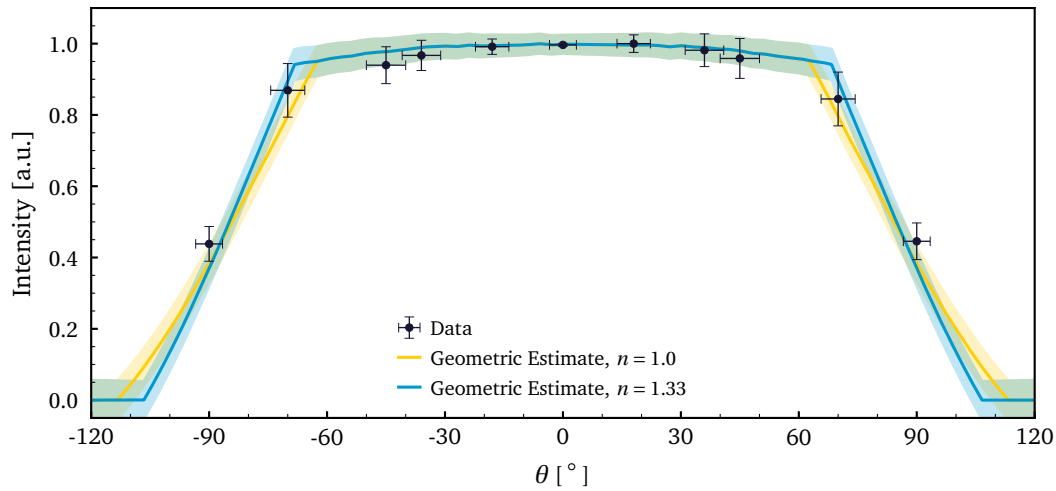


Figure 4.21: Preliminary POCAM hemisphere emission profile in air. Shown are measured and expected isotropy with respect to polar angle. The estimates and their 1σ -bands arise mainly from the POCAM geometry while assuming air (yellow) and water (blue) as outer medium with indicated refractive indices and injected integrating sphere emission.

4.3.5 In-situ Calibration

Before concluding the POCAM chapter, its internal calibration will be discussed conceptually and the calibration results for the POCAMs in STRAW will be presented. The POCAM contains four Kapustinsky flashers equipped with a total of four different LED configurations. The internal monitoring sensors are a large-area PIN-photodiode from Hamamatsu (*S3590-08*) and a $3 \times 3 \text{ mm}^2$ SiPM from Ketek (*PM3315-WB*). The charge output of each sensor is fed into a gain chain with a sensitive charge-amplifier and then sampled by a 10-bit ADC. The measured amplitude is directly proportional to the charge output of the sensors, as will be verified shortly. An exemplary output of the latter is visualized in fig. 4.22. Here, the SiPM is much less affected by internal electronic noise due to applicability of a much less sensitive charge-amplifier.

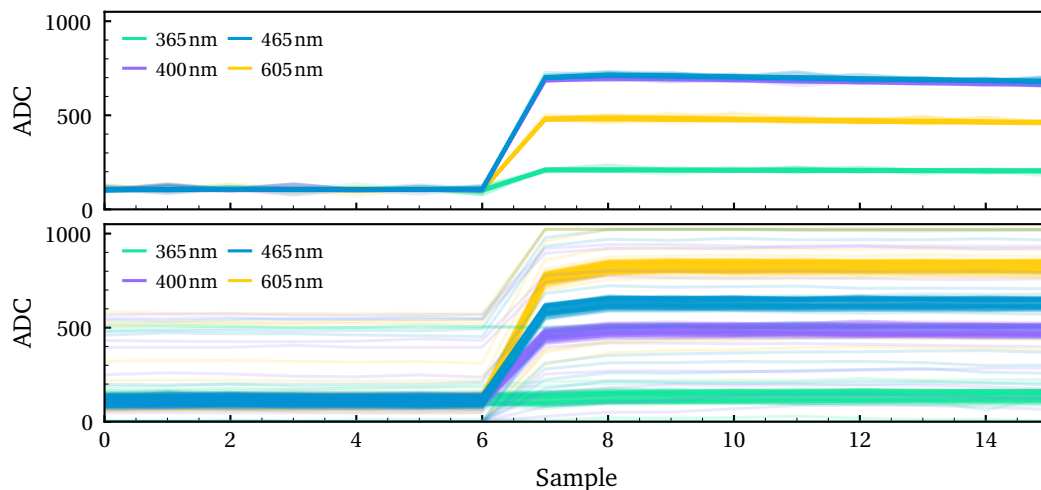


Figure 4.22: Exemplary output of the internal POCAM photosensors. Depicted is the output of the SiPM (top) and the photodiode (bottom) received by the 10-bit ADC after their gain chain. While the flasher was operated at 20V in all cases, the Photodiode was biased at 10V and the SiPM at 29V. As can be seen, the diode signal is a lot more affected by present electrical noise.

As these chains include a variety of components, an end-to-end calibration was performed. That is, a second calibrated large-area photodiode was used as a reference sensor measuring the forward emission ($\theta = 0^\circ$) of the POCAM. This then allowed extraction of the photon output knowing its emission profile and comparison to the internal sensor output. However, as can be seen in fig. 4.22, electronic noise can cause traces to exceed the dynamic range of the ADC. That happens only sporadically, as the gain was adjusted so that generous margins remain for each LED and flasher intensity, however, these traces have to be disregarded.

For the visibly clear SiPM responses, a normal distribution was fit to measured amplitudes in order to determine the mean and sigma of the achieved signals. This procedure is seen in fig. 4.23. For the noise-affected photodiode, the amplitudes were extracted on an average basis of baseline and signal. While the SiPM reaches an internal precision of down to $< 1\%$, the photodiode reveals a relatively large mean spread of $5 - 10\%$.

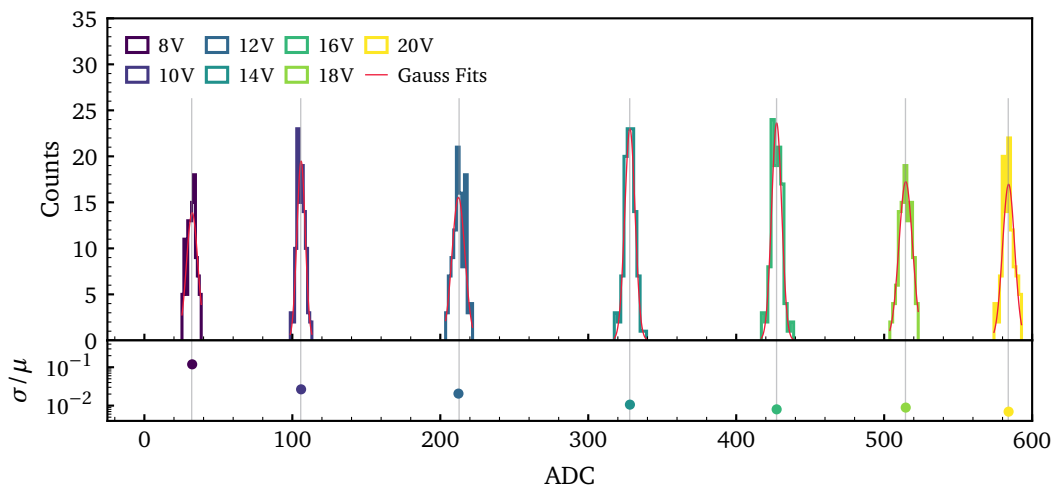


Figure 4.23: Amplitude extraction from internal SiPM signals. Visualized are histograms of observed ADC amplitudes extracted with respect to their observed baselines (top) and their resolution extracted from Gaussian fits (bottom), both is done for several flasher voltages and the 465nm LED. Additionally, the averages obtained without fit are displayed.

As the next step, the sensor responses to the light input have to be discussed. While the linear behavior of the gain chain can be validated using the photodiode [e.g. 88], the SiPM response has to be treated more extensively.

In general, a SiPM is an array of parallel *semiconductor single-photon avalanche diodes* in geiger mode that are called pixels and have sizes in the micrometer range. The SiPM is reverse-biased with a voltage greater than the breakdown voltage of the p-n junction and hence a generated charge in a pixel will initiate an avalanche that can be detected. As a result, the total gain is directly proportional to the bias voltage [47] and in turn, the total charge output to the gain and the number of pixels that were triggered or *fired*. Nevertheless, as for every photodetector, pixels can also trigger from thermal charge generation (*dark counts*) and even from a neighboring pixel firing (*Crosstalk*), however, this becomes decreasingly important for an increasing number of photons incident on the SiPM.

Being a semiconductor, each pixel only has a probability to generate charge upon being hit by a photon, this is called the *photon detection efficiency* (PDE) and means that the process of detecting an incident photon pulse with a SiPM is stochastic. As such, it is expected that the output signal will deviate quickly from linearity once the SiPM will start to saturate. The latter is a well-known fact among experimental scientists using those detectors [e.g. 66, 80].

A common response approximation that describes this behavior can be deduced from a differential equation, described in appendix A.1. If the recovery time of a pixel is much larger than the pulse length of the light pulse, this eventually results in a solution relating the number of fired pixels N_{fired} , i.e. the measured charge output, to the number of incident photons N_γ

$$N_{\text{fired}} = N_{\text{pixel}} \cdot \left[1 - \exp\left(-\frac{N_\gamma \cdot \text{PDE}}{N_{\text{pixel}}}\right) \right] \quad (4.12)$$

The SiPM used in the POCAM encompasses 38800 pixels with a size of $15 \mu\text{m}$ and a recovery time of approximately 35 ns. As the POCAM light pulses are much faster, eq. (4.12) is used for the SiPM response calibration.

Now, for all LEDs and the complete available voltage range of the Kapustinsky circuits, a calibration run was carried out. With the reference photodiode positioned in $\theta = 0^\circ$ direction, the measured amplitude in the ADC is compared to the number of detected photons at the reference. Together with the emission characteristic of the POCAM, the total light output can be deduced. For an exemplary POCAM hemisphere, the calibration output is illustrated in fig. 4.24. The calibration now relates total number of emitted photons from a single hemisphere with respect to the ADC value read-out from its internal sensors. The photon output of each LED within the POCAM in STRAW spans close to two orders of magnitude and a peak emission of $(3.65 \pm 0.21) \times 10^8$ photons/ 2π for the 605 nm LED and room temperature. This calibration has been run for all hemispheres individually and identifies the emission characteristics of every instrument. A comparison will be omitted at this point, as individual data will become relevant only in the scope of the STRAW data analysis. Notably, all POCAMs revealed similar behavior with deviations of a few percent.

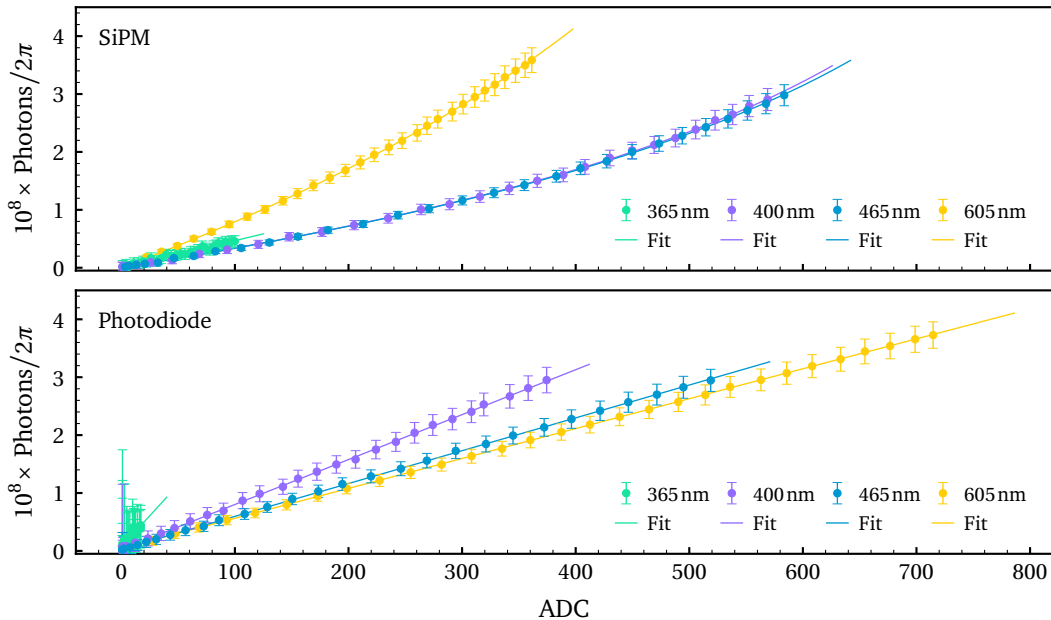


Figure 4.24: Exemplary POCAM calibration plot. Shown is the total photon emission in 2π versus the measured ADC value for the SiPM at 29V bias (top) and the photodiode (bottom), including respective fits as explained in the text. The former is deduced from a calibrated reference photodiode in $\theta = 0^\circ$ direction. The flasher voltage range covered in this plot is 6–20V in 0.5V steps. The linear photodiode response confirms the linearity of the gain chain and the flasher circuit. The sensor differences in quantum efficiency are clearly visible.

4.4 Summary

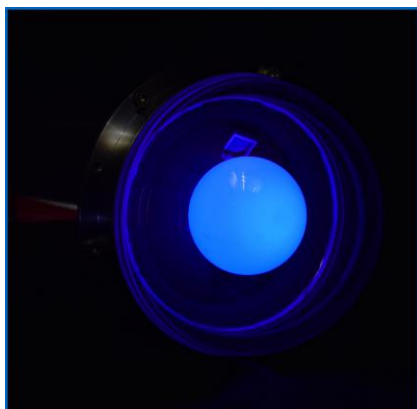


Figure 4.25: Long exposure of an illuminated POCAM hemisphere. Taken with the help of K. Holzappel.

To summarize, first the design and concept of the POCAM and all of its components was introduced. While the proof of concept for this design has already been demonstrated with successful deployment and operation within a cluster of the GVD detector, further aspects and improvement towards the current revised version for STRAW have been presented. The calibration and investigation of light emission characteristics for STRAW POCAM and the internal calibration procedure have been discussed in detail. The conclusion of which was a 4 – 8 ns pulses with a strong grade of achieved isotropy in the unobstructed field of view of each POCAM hemisphere as well as precise calibration using the internal sensors. The photon output per hemisphere is adjustable with flasher voltage and hence spans almost two orders of magnitude, peaking with $(3.65 \pm 0.21) \times 10^8$ photons/ 2π for the 605 nm LED at room temperature. With the SiPM, the internal calibration achieves a read-out resolution of $< 1\%$ and is only further affected by systematics of the reference measurement and the azimuthal symmetry of the integrating spheres. Notably, the internal photodiode was affected by the internal noise and revealed a much larger spread.

The revision of the POCAM shown in fig. 4.26 inhibits promising characteristics and justifies its application in the scope of the STRAW project. Its light emission has been precisely calibrated and can be used to homogeneously illuminate detector volumes in the deep sea. For a potential IceCube application, the objectives will be to further increase the grade of azimuthal isotropy and to perform a temperature calibration of the total light yield.



Figure 4.26: Finished POCAM module for STRAW. In addition to the instrument itself the mounting structure for the holding structure is visible.

5

STRAW Digital Optical Module

After introduction of the POCAM, the *STRAW Digital Optical Module* (sDOM) will be content of this chapter. In contrast to the existing POCAM, the sDOMs were designed specifically for the application in STRAW. After introducing their design and components, the light detection characteristics and calibration will be presented.

5.1 Design

In this section the sDOM will be explained in its core functionality and components. As it is similar in design to the POCAM, some sections will be kept brief.

5.1.1 Concept

The sDOM is a newly developed module, specifically designed to act as the light sensor in the STRAW detector. As such, it poses as the complementary instrument to the POCAM.

In the scope of STRAW, it will be used to observe POCAM flashes in a defined detector geometry and in turn determine absorption and scattering properties of the water present in the Cascadia Basin. Based on the POCAM design, it makes use of two photomultipliers to allow nearly isotropic light detection. Upon their precise calibration, they further allow to characterize the light background from radioactivity and bioluminescence.

5.1.2 Housing

The housing of the sDOM was based on the concept used for the POCAM, since the latter had already been successfully tested in deep waters. The housing itself consists again of the same type of titanium cylinder, however, significantly longer to allow enough room for two PMTs, read-out electronics, communication, internal mounting and heat dissipation. It is comprised of the main cylinder as well as two hemispheres and measures around 60cm in length. It is shown in fig. 5.1 and resembles in all its qualitative aspects the POCAM housing. According to the manufacturer, this design will withstand at least 600bar of outer pressure and the same temperature conditions as the POCAM. More importantly, it is thus rated to conditions by far exceeding those present in the Cascadia Basin and hence is applicable for deep-sea deployment. Nevertheless, as explained later, the new sDOM housing was subjected to a number of environmental tests to guarantee the latter. Also for the sDOM the same penetrator and vacuum port are used to allow power supply and slow control as well as evacuation in order to remove humidity.



Figure 5.1: *The sDOM housing design.*

5.1.3 Photosensor

Each sDOM is comprised of two PMTs, with one located in each hemisphere. These are the primary light detectors of the sDOM and are used to detect primarily POCAM flashes but also background light. The used PMTs are round-shaped, 3" models by Hamamatsu (*R12199*) and use a Bialkali photocathode with a spectral response from 300 – 650 nm. Furthermore, it shows high gain due to a 10-stage dynode system. [97]



The detection principle of a photomultiplier relies on the photoelectric effect, that is, the emission of electrons upon incident light on the photocathode. Using an applied high voltage (HV), such *photoelectrons* (PEs) are then accelerated through the dynode chain and multiplied at each stage by collision-ionization. This way, an incident electron can be amplified by $10^5 - 10^8$ in charge until arriving at the anode where the signal is measured.

As for almost every photodetector, a signal can also be caused by noise-related sources, better known as *dark counts* or *dark rate*. For one, thermionic emission of electrons causes a thermal component of signals that varies with temperature. Thermal dark counts are usually caused by single electrons and can not be distinguished from single-photon signals. Nevertheless, lower temperatures are usually beneficial for applications involving PMTs since the rate of thermionic emission depends on temperature T (and the work function of the metal W) according to Richardson's law [103]

Figure 5.2: sDOM PMT and its high-voltage base.

$$r_{\text{thermal}} \sim T^2 \exp(-W/k_B T) \quad (5.1)$$

Notably, at cryogenic temperatures, the dark rate has been observed to increase again but a physical cause remains to be found [87]. Another source of dark counts are high-energy charged particles, like cosmic rays or radioactivity, which can cause scintillation or Cherenkov radiation inside the glass as well as ionization of the cathode material or residual gases inside the photomultiplier tube. Additionally, after a signal has been produced in the PMT, electrons can scatter inelastically back to the cathode or ionize residual gas, both of which causes *afterpulses*, that come correlated but delayed to the primary signal [98].

5.1.4 Optical Gel

Since the PMT is encapsulated by the pressure housing glass, its field of view is limited by refraction and reflective losses would become non-negligible when coupled with a vacuum gap. As a result, the PMTs will be optically coupled to the glass using optical gel, that is, a curing transparent silicon gel which allows transmission of light and increases the effective area in water towards large polar angles. Additionally, it significantly reduces reflections on boundary layers. The main requirements on the gel were good transmission for wavelengths of 350 – 600 nm as well as a refractive index close to that of the pressure housing glass and that of the PMT photocathode window. The spectral range was defined based on the PMT quantum efficiency, the pressure housing glass and the expected water properties.

In the end, an optical gel by Wacker (*SilGel 612*) was used since it is also in operation in the KM3NeT optical modules with the same PMT model and comparable glass [36]. As has been discussed, it provides sufficient transmission in the relevant spectral range and furthermore matches the glass [106] as well as photocathode window [36] refractive indices of around 1.52 – 1.54 with $n_{\text{Gel}} = 1.4$ at 589 nm [119]. Thus, it provides significant reduction of reflection losses compared to vacuum.

5.1.5 Read-Out Electronics

The sDOM electronics are two-fold. For one, a single-board computer runs a custom operating system based on Linux and handles internal and external controls as well as communication. The read-out of the PMTs is handled by a *Trigger Read-out Board (TRB3sc)* and a *PaDiWa3* front-end, both manufactured by GSI in Darmstadt. While the former is based on a single FPGA and *time-to-digital-converters (TDCs)* with potentially picosecond precision [90] the latter shapes and amplifies signals for proper TDC measurements. The main line of communication to the sDOM is Ethernet, however, a backup serial connection is available. Again, all of the STRAW-side electronics have been designed by the resident electrical engineer M. Boehmer in collaboration with GSI and the help of C. Spannfellner, a Master student in the group.

For each PMT in an sDOM, the raw signals are split into four different gain channels for an increased dynamic range that still allows single photon detection. The coupling to the front-end was a high-pass filter for the single-photon channel and a low-pass filter for the remaining ones. The former enables precision timing information, the latter pulse stability. The main handle on the deposited charge, i.e. the number of detected photons, is the *time-over-threshold (ToT)* measured in each channel. Notably, a voltage threshold is defined in the TDC which triggers and sends a time-stamp once the signal edge crosses it. The ToT is the time between the rising and falling edge of the signal and is correlated to the incident charge. Using four channels and thus sampling the signal allows for charge determination as well as precision timing information. This principle is also illustrated in fig. 5.3. Absolute timing is provided by a sub-nanosecond precision synchronization pulse, as will be explained in chapter 6.

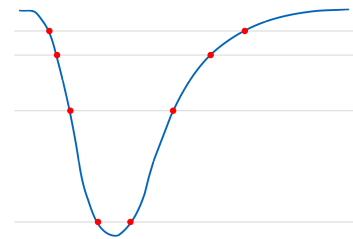


Figure 5.3: Concept of the TDC sampling a large PMT pulse.

5.1.6 Internal Mounting & Heat Dissipation

One of the challenges during the design phase of the sDOM was to design its internal mounting structure and enable heat dissipation. Since the dark rates of PMTs are highly sensitive on temperature, a good heat coupling from the inside to the outside of the module has to be achieved. The length of the sDOM resulted from the fixed size of the PMT read-out electronics and numerous other components which had to fit inside the titanium cylinder. The principle is visualized in fig. 5.4 and presents the design of C. Spannfellner. All the electronics are mounted on an aluminum plate which is fixed to PMT negative mounts of one hemisphere. For noise protection, the PMT signal processing has been isolated to one site.

As for the heat sink, time constraints forced a relatively simple design even though more advanced concepts were available. As such, a rectangular piece of aluminum pressures a heat conductive pad to the main heat source, namely the power converter, and couples it to the outside of the instrument. While in-air operation was possible, temperatures were reaching critical levels after about an hour of operation. Tests in 17°C water revealed stable temperatures hours after operation with the PMTs a few degrees above ambient water temperature and thus confirming functional and sufficient heat dissipation, especially in the deep sea.

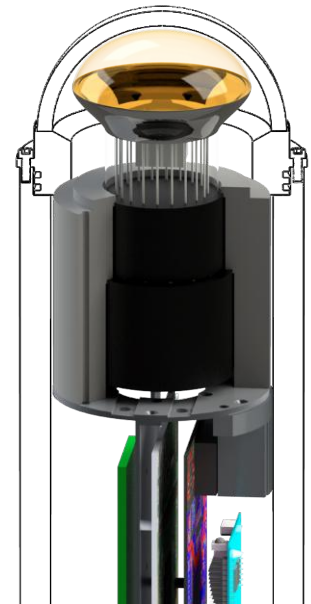


Figure 5.4: The internal sDOM mounting design. Concept by C. Spannfellner.

5.2 Light Detection Characteristics in STRAW

Equally important as light emission is the light detection in STRAW. While the detailed characterization of all sDOM PMTs is part of an ongoing doctoral thesis, this section will briefly outline its procedure.

5.2.1 PMT Characterization

In order to be able to extract precise intensities from different PMTs and allow analysis of the water properties in the Cascadia Basin, all sDOM PMTs needed characterization and calibration. The former was done by I.C. Rea as part of her doctoral thesis, the latter was done after the optical gel was poured into the glass hemispheres and the PMTs were mounted inside. After curing, the PMTs were then subjected to a temperature dependent analysis that will be presented in detail in this work. The primary goal was to calibrate the individual dark rates of each PMT and their temperature and voltage dependence.

Inherent Properties

The characterization of inherent properties was organized so that, each PMT was going through a number of measurements in order to be able to extract all of its individual characteristics. The measured quantities of each PMT include: *gain*, *linearity*, *single photoelectron (SPE) amplitude*, *quantum efficiency (QE)*, *transit time spread (TTS)* and an estimate on the behavior of the dark rate. All of the characterization measurements were done using a picosecond 405-nm laser setup that was calibrated using a reference high-precision photometer. An exemplary gain and linearity calibration is visualized in fig. 5.5. It reveals the expected behavior of increasing gain and decreasing linearity of the PMT by raising its supply voltage.

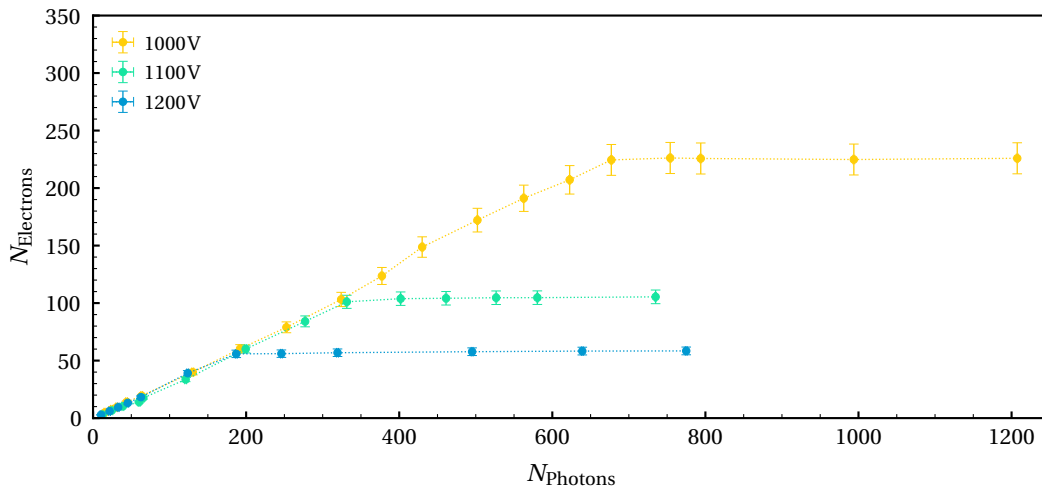


Figure 5.5: Exemplary linearity measurement of an sDOM PMT. The gain was measured to find a configuration of equal gain among all used PMTs in STRAW. Furthermore, the linearity is an important quantity for the light detection of the sDOMs. Data is a courtesy of I.C. Rea and the detailed analysis will be subject of her doctoral thesis.

The measurements revealed the expected deviations among all of the ten characterized sDOM PMTs. Most relevant for STRAW, the gain, linearity and TTS of the PMTs could be measured precisely and, in the scope of the STRAW analysis, will allow extraction of the incident light flux.

Dark Rate & Temperature Calibration

After the characterization of inherent photomultiplier properties, the PMTs were subjected to a temperature controlled and light-tight environment in order to investigate dark rate effects and its temperature dependence. This is especially important to measure background radiation, as was already discussed in chapter 3.

After discussions with ONC, the expected temperature down in deep waters of the Northern Pacific were expected around $2 - 4^{\circ}\text{C}$. In combination with the heat generation inside the instrument, a temperature range of $0 - 25^{\circ}\text{C}$ was investigated. The setup was fully automatized and controlled temperature, high voltage and read-out of the subject PMT. After a few hours on low voltage, the PMT was read-out in subsequent intervals of 200ms for 100 times and the raw data was stored. A simple peak-detection algorithm was then identifying PMT pulses over an adjustable noise threshold. For the dark rate, the amplitudes crossing the threshold were histogrammed and a Gaussian fit delivered the mean amplitude of the SPE peak. The results were in fine accordance with the previous inherent measurements. As per common practice [98], $1/3$ of this amplitude was then set as a threshold to determine pulses contributing to the dark rate. An exemplary amplitude determination is depicted in fig. 5.6.

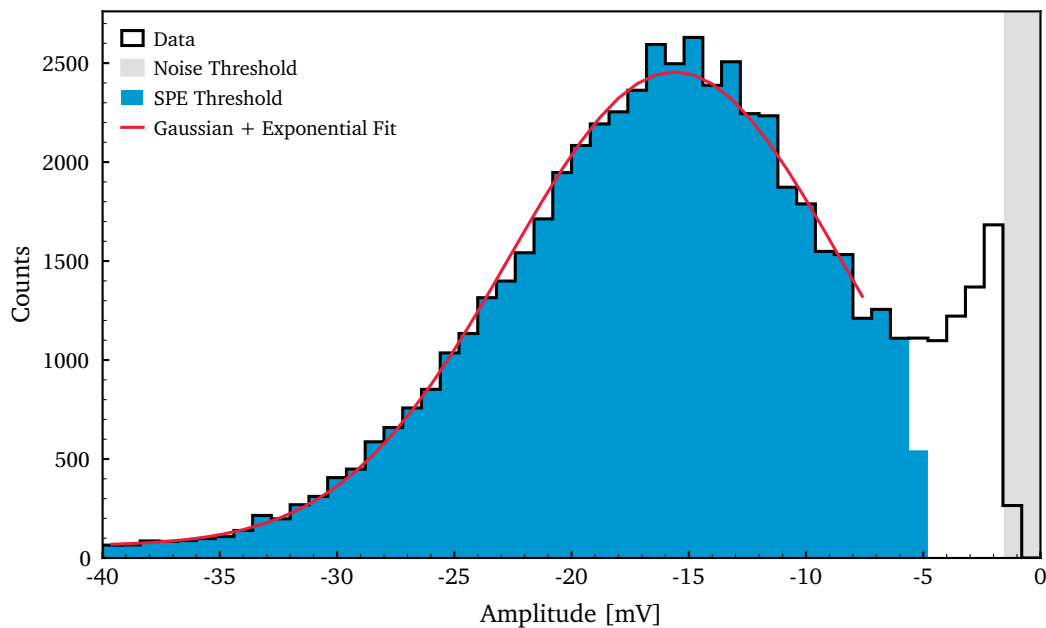


Figure 5.6: Exemplary single-photon amplitude spectrum of an *sDOM* PMT at 1200V obtained from peak-detected pulses in 100 time intervals of 200ms each. In red, a Gaussian Fit with an additional exponential matches the data well. After applying a threshold according to $1/3$ of the SPE mean, only pulses in the blue area of the histogram are left for dark rate analysis.

Now, the PMT was mounted inside the glass hemisphere flange and the optical gel around it was cured. As such, several new sources for background radiation have been introduced. While the gel usually is not the main influence on the dark rate of the PMTs at a significant level [117], the glass has been observed to increase the background noise due to its radioactive content which is believed to be mostly potassium [7]. The latter can cause scintillation and Cherenkov radiation in the glass and gel as well as ionize residual gas inside the PMT. As such, the dark rate of the PMT is not only dependent on its own characteristics but its direct environment and is usually increasing upon encapsulated with glass and optical gel. The precise knowledge of the dark rate components is necessary to enable the investigation of background radiation.

If the occurrence of dark counts in time would be completely uncorrelated, that is, independent of each other, the process would be Poissonian. In fact, it would be described by an exponential distribution dependent only on its average rate λ . To illustrate that, let the time of the last event be t_0 , then the probability to not observe a subsequent event after time t is

$$P(t > t_0) = \frac{(\lambda \cdot t)^0 \exp(-\lambda \cdot t)}{0!} = \exp(-\lambda \cdot t) \quad (5.2)$$

In turn, this can be used to deduce the *probability density function* $f(t)$ of a purely uncorrelated dark rate via the time-derivative of its *cumulative density function*

$$f(t) = \frac{d}{dt} (1 - P(t > t_0)) = \lambda \exp(-\lambda \cdot t) \quad (5.3)$$

which shows the expected proportionality to $\exp(-\lambda \cdot t)$ [117]. Furthermore, this can now be used to differentiate between uncorrelated and correlated noise events. For instance, the latter could be caused by radioactive scintillation or Cherenkov radiation in glass or gel which would emit a correlated burst of photons in a certain time interval that would deviate from the purely exponential behavior [111, 117]. This non-Poissonian noise has already been observed in the scope of IceCube, however, remains to be distinctly explained [7].

For the PMT pulses that are left after the 1/3 SPE threshold (ref. fig. 5.6), the time difference Δt distribution can be analyzed accordingly. As seen in fig. 5.7, the Poisson expectation describes the majority of medium to long time intervals well. However, similar to IceCube, the sDOM PMTs encapsulated in glass and optical gel also show a significant deviation on short time scales. Notably, this correlated noise makes up a significant fraction of the dark noise.

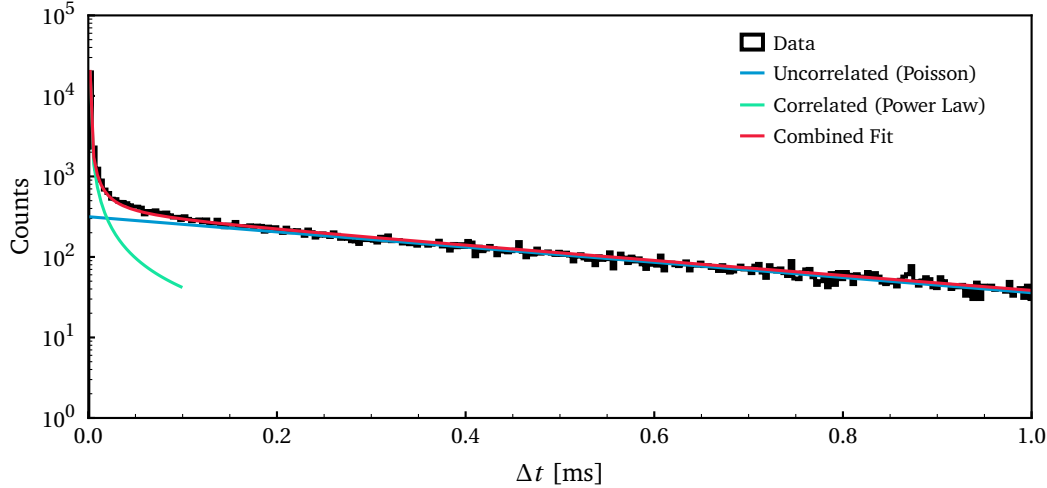


Figure 5.7: Exemplary Δt histogram of peak-detected noise pulses from an sDOM PMT at 1200V and 25°C. The Poisson expectation describes the uncorrelated noise hits well, however, the correlated part significantly deviates. Nevertheless, it can be matched with a combined fit of the uncorrelated exponential and a power law. In this case, the mean uncorrelated rate was 2.2kHz.

Furthermore, a detailed analysis of the $\log_{10}(\Delta t)$ histogram can be used to determine different components of the present noise hits. As explained in [111], shown in [7] and presented in fig. 5.8, this histogram can be matched with a multi-component model representing correlated noise (thermionic, radioactivity), afterpulses and unexplained correlated noise. In combination with measurements of a bare PMT without glass and gel, the deduction of these properties will allow determination of the housing contribution to the dark noise and subsequently the determination of the background radiation in the Cascadia Basin.

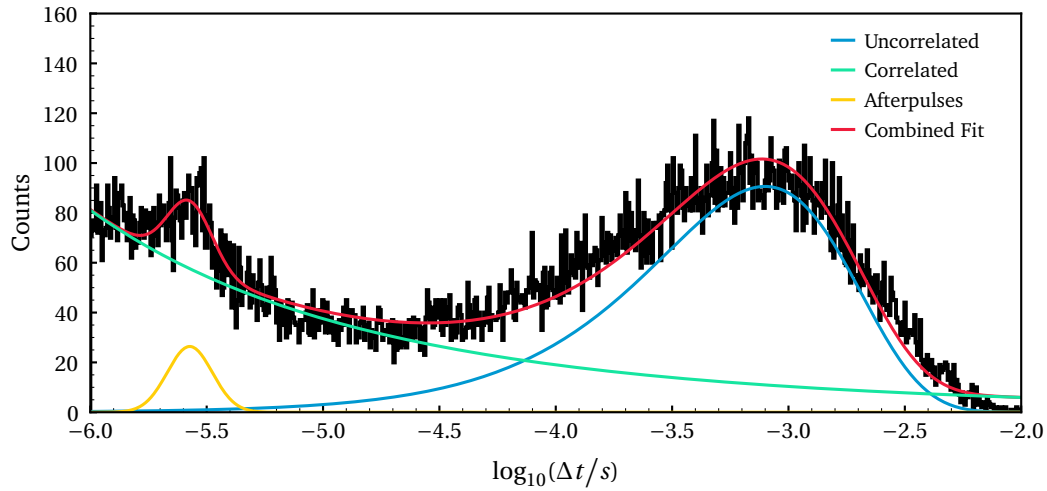


Figure 5.8: Exemplary $\log_{10}(\Delta t)$ histogram of an sDOM PMT at 25°C following the models presented in [111]. The used models are Poissonian (uncorrelated), lognormal (correlated) and Gaussian (afterpulses). While the correlated noise and afterpulses seem well understood, the correlated component still raises questions. As its physical explanation is yet to be defined, the underlying models are usually based on empirical approaches.

Both methods allow extraction of the uncorrelated dark rate. Exemplary results for the Δt -method are presented in fig. 5.9 and verify the expected increase of uncorrelated dark noise with temperature and high voltage. While these measurements are available for each sDOM PMT, a comparison will be done in combination with a detailed analysis of the STRAW data. Thus, further investigation of the dark rate will be omitted at this point.

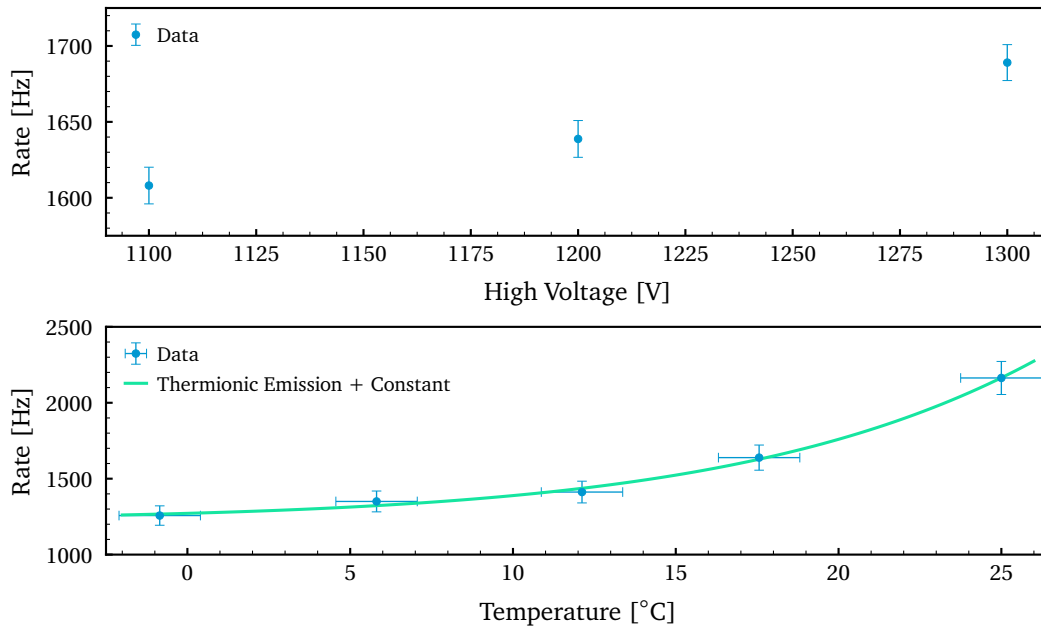


Figure 5.9: Exemplary sDOM PMT dark rate dependence on voltage (top) and temperature (bottom) obtained from the procedure in fig. 5.7. Both show the expected behavior of an increased rate when increasing the respective quantity. The data is fit with the expected thermionic emission behavior given in eq. (5.1) and a constant resembling temperature-independent noise.

5.2.2 Optical Properties

Furthermore, the optical properties of the system can be used to extract the number of incoming photons from the observed charge. That includes: QE of the PMT and transmission of the glass and gel. The convolution of all these properties defines the PDE of an sDOM hemisphere. While detailed glass data exists and was provided by the manufacturer [106], the gel was measured in a common UVVIS spectrophotometer. In the scope of STRAW, the QE can be deduced from the slope of the linearity measurement, however, only at 405 nm. For the spectral range, an average, obtained from numerous KM3NeT measurements on the same PMT [20] was used for estimates and subsequently can be compared to characterization measurements of STRAW.

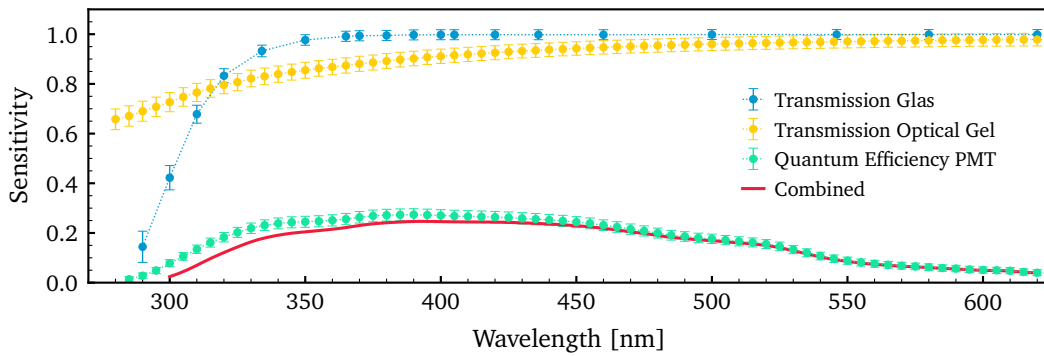


Figure 5.10: Optical properties of sDOM components including N-BK7 glass [106], two-component Wacker SilGel 612AB (mixture 1.5:1) and QE of the Hamamatsu R12199 PMT [20].

5.2.3 TDC Read-Out

Lastly, all sDOMs were calibrated in a test water tank using the POCAM as a light source to record in-situ measurements with the TDC. Both calibration measurements of intensity and angular acceptance were carried out, however, it is a matter of further analysis to extract the charge and subsequently light flux from the TDC data. In general, preliminary studies suggest that the TDC is able to record from single- up to a few hundred photons and the limiting factor is actually the PMT linearity. For illustration, preliminary read-outs are shown in fig. 5.11.

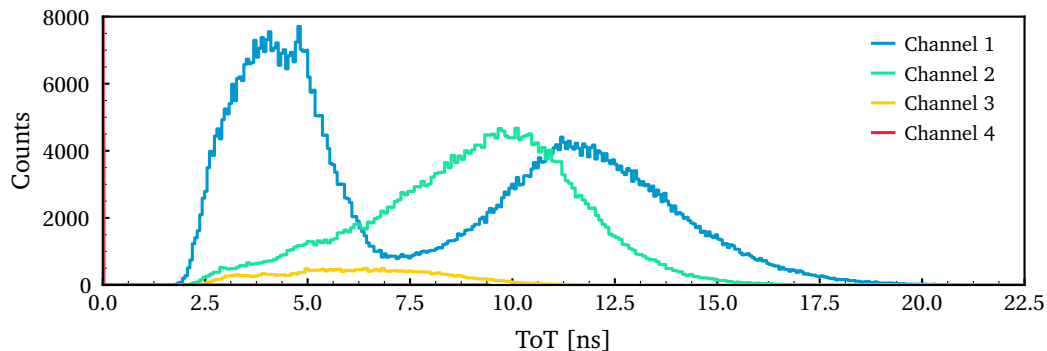


Figure 5.11: Preliminary TDC read-out of an sDOM PMT at moderate POCAM flash intensity. The data resembles the measured ToTs for channels of decreasing gain. While the SPE channel (blue) also measures dark noise (left peak), the flash intensity is too small for detection in the lowest-gain channel (red). The expected behavior of decreasing ToT with lower gain is visible and confirms the planned concept visualized in fig. 5.3.

Notably, it is a matter of further effort on the TDC data acquisition and analysis to eventually extract detected charge from timing measurements. Nevertheless, promising software approaches are already in place that, upon completion, will enable the latter.

5.3 Summary

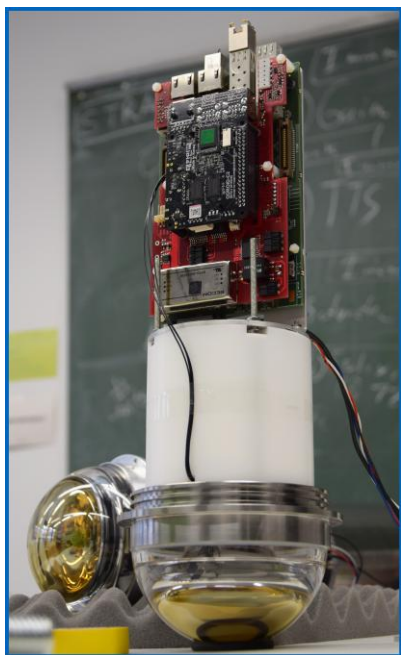


Figure 5.12: *An early sDOM hemisphere assembly prototype.*

The sDOM is a newly developed module specifically for the application in STRAW. As such, the development and characterization of its component was in focus over the course of the STRAW project. The latter justified itself by allowing the determination of PMT characteristics of every sDOM and revealed the expected large deviations among individual PMTs. While the inherent properties of the PMTs are part of an ongoing doctoral thesis, this work investigated temperature effects of the dark noise and presented procedures for further analysis in the scope of STRAW. Additionally, a full set of in-situ calibration data was recorded in a test water tank for a variety of POCAM flasher intensities.

However, to extract charge and eventually light intensity information from the TDC data will require further analysis and software understanding as it is an external system provided by GSI in Darmstadt. Nevertheless, preliminary studies suggest that the sDOM can differentiate well between light of different intensities and as such is a viable sensor module for the optical characterization of the deep sea. A prototype of the sDOM assembly is depicted in fig. 5.12 and four of the five finished modules in fig. 5.13.

A picture of an sDOM submerged in the test tank can be found in appendix C.

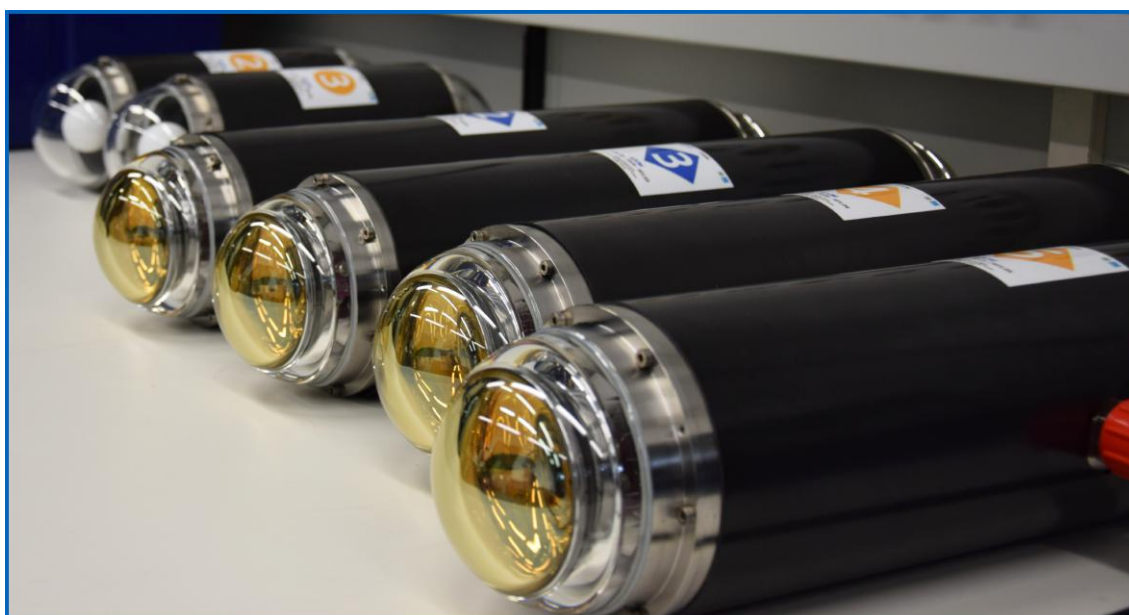


Figure 5.13: *sDOM instruments prior to shipment to Canada. One module is missing since it was finishing calibration in the test tank when this photograph was taken.*

6

The STRAW Detector

The last chapter of this thesis will present the STRAW detector that emerged based on the physical considerations and its instrumentation. After presenting the mechanical and deep-sea aspects of the detector, qualification and on-site testing in Canada will be described. The chapter will close with the detector deployment and the very first data from the operational detector.

6.1 Deep-Sea Infrastructure

Now, after definition of the STRAW geometry, an according deep-sea infrastructure had to be designed, produced and assembled. As the mechanical aspects are subject of another master thesis, it shall only be briefly presented here. During the whole project, the team was supported by K. Leissmüller, a subsea expert from the KM3NeT project

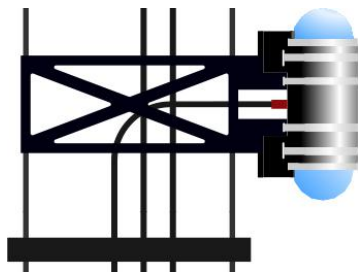


Figure 6.1: STRAW instrument on a string with spacer and VEC. Courtesy of K. Holzapfel.

Eventually, the string design was decided to be comprised from two steel mooring lines, an anchor on the bottom and a float on top. While the structure is fixed on the anchor, the float is allowed to rotate with a swivel below. This way, the float gets rid of any angular momentum build-up and the structure remains stable and upright. The anchor itself was designed so that it can temporarily be rotated by the ROV before being fixed with a pin. The former is necessary in order to orient the strings facing each other once deployed. As seen in fig. 6.1, special mountings were designed for the instruments which fit in between the two wires with instruments mounted on their side. The two-wire distance was additionally kept by metal spacers placed every 5m which should provide further mechanical support to the structure but more importantly to guide the *vertical electrical cables* (VECs) to the instruments with enough slack. To reduce reflection and scattering off the structure as much as possible, most of the components were either ordered black or later colored using deep-sea applicable dye. In order to avoid corrosion of the components, the titanium instruments were isolated from the remaining structure using rubber and *polyoxymethylene* (POM) while the string was made from mainly structural steel. For further protection, a sacrificial anode is placed on the anchor. The full string structure is depicted in appendix A in fig. C.1.

The VECs, coming from the instruments, are connected to a *mini junction box* (mJB) which provides the connection point of a string to the *node*, that is, the ONC infrastructure. As such, they provide power, slow control and data acquisition for all instruments. Furthermore, a sub-nanosecond sync pulser is included here which provides synchronization between all sDOMs on both strings. It was developed by M. Boehmer and successfully integrated into the mJB together with electrical engineers of ONC. However, as the sync has to be distributed to all instruments, both strings are *daisy-chained* which means that one string is connected to the second one which then connects to the ONC node. While this can be problematic, no other

option was feasible given that the ROV had to manage all deep-sea connections. Furthermore, each string was planned to be tested directly after connection and so, with the ROV still present, re-connections would have been possible in case of issues.



Figure 6.2: Spooling system of a STRAW string. The instruments and the engine are visible.

of such a STRAW string is shown in fig. 6.2 and shows the spool, the instruments in their dedicated slots and the transmission engine that controls reeling, unreeling and braking of the spool movement.

Finally, the shipping and deployment of the meanwhile 150m long structure was managed using a custom-made spooling system shown in fig. 6.2, which was designed by A. Gärtner and will be subject of his Master thesis. The system was constructed to fit a full string including instrumentation, steel wires, VECs and spacers. The spooling is then controlled and operated using an industrial transmission engine. With the help of the latter, the structure could be reeled and unreeling and allowed spacer-by-spacer assembly of a string and precise positioning of the instruments. Furthermore, the shipment of the structure was kept compact and deployment was planned to be managed by directly unreeling the spool from the deck of the ship. Each string was assembled and reeled up on such a spool and eventually shipped to Canada. A full assembly

6.2 Qualification & On-site Testing

In the scope of a project of this scale, the qualification of all components for the expected conditions is essential. When submerged to almost 3km depth in the sea, all components are subject not only to almost 300bar of pressure, but also low water temperatures and salinity. Furthermore, the deployment poses a great stress on the structural components, especially the steel wires, line terminations and VECs as well as vibrations and shocks for all components, including the instruments.

While all the mechanical components were produced from structural steel which is applicable for deep-sea conditions, the instruments are made from titanium and hence would cause corrosion when in direct contact with the rest of the structure. As such, the instruments have been isolated from the structure using rubber sleeves and POM parts in the mounting. This was already successfully tested during the one year deployment of the POCAM prototype in lake Baikal. For additional corrosion protection, a sacrificial anode is placed on the anchor. In order to handle the loads during deployment, the steel wires have been chosen with a safety factor of four with respect to the expected loads. The VECs were assembled so that enough slack is available once the steel wires straighten during deployment.

In terms of vibrations, the module mountings and instruments were subjected to an industrial standard vibration- and shock testing protocol which swiped a certain frequency range and shocks up to 10g. All instruments passed the tests without any visible, functional or structural damage and were seen fit for the deep sea deployment. Additionally, the sDOM was subjected to a pressure test since only the POCAM housing has been deployed so far. The test imitated several deployments with a maximum pressure of around 380bar and also here the instrument passed without any complications.

Once the structures arrived in Canada, on-site testing started. The testing protocols resulted from various iterations between the STRAW side and the ONC side and include tests that verify not only STRAW functionality but also integrity together with the mJB provided by ONC and ONC standards for deep-sea durability.

The tests included not only string power supply and slow control via the mJB but also the synchronization distribution. Furthermore, grounding faults were double checked by ONC via conductivity measurements of all instruments. At the end, the node, both mJBs and the strings were submerged in the test tank and a full system test was carried out. The result of which was successful and equipment was stored while last synchronization issues were fixed on-site. As the latter were solved, the structure was loaded on the ship, prepared for storage and waiting for deployment.



Figure 6.3: STRAW assembly being submerged in the ONC test tank using a heavy lift crane.

6.3 Deployment

The deployment of both STRAW strings was carried out by marine experts from ONC. The ship *John P Tully* left the harbor in Victoria on the 21st of June 2018 and arrived on-site in Cascadia three days later. Soon after, preparations for the STRAW deployment started.

The deployment strategy foresaw the spools being fixed to the back deck of ship and then, starting with the float, unspooling the string into the water. In addition to the STRAW float, a second one was attached so that the string would be buoyant and which was then dragged out behind the ship by a *rigid-inflatable boat* (RIB). While the structure was unspooled, the crew on the back deck guided the instruments securely over the stern of the ship. Upon completion, the load was transferred from the spool to the ship and the mJB was attached to the string together with the anchor. As seen in fig. 6.4, the anchor was then lowered on the heavy lift line of the ship and acoustic released. With the two buoys still with the RIB, the string swung in vertical orientation with the buoys keeping it afloat. Eventually, the RIB closed in onto the ship and the heavy lift line was attached to the STRAW buoy. The additional one was removed and the string was lowered to its final depth of 2654 m where the heavy lift line was also acoustic released and the string freely descended the last few meters to the seafloor. After the heavy lift line was recovered, the second string was deployed accordingly.

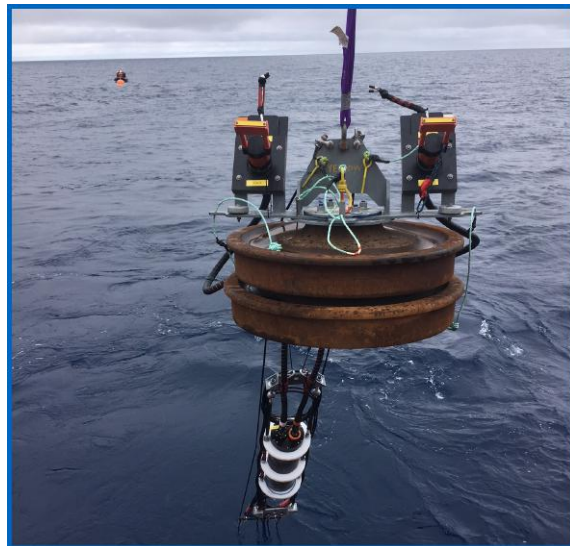


Figure 6.4: STRAW string during deployment with the anchor attached to the heavy lift line and the RIB in the background. Courtesy of P. Macoun, ONC.

Upon completion of the string deployment, the ROV was made ready to dive for inspection and connection of both strings. Once arriving in the depth, the ROV determined its precise

orientation and position using sonar before moving towards the STRAW units. The first step was inspection, that is, diving up vertically along the string and verify system integrity and in case inspect possible damages. As seen for the exemplary detail in fig. 6.5, the first string was intact, vertically aligned and without visible damage on lines, VECs or instruments. The inspection of the second string was equally successful, also here vertical alignment and no visible damages on any of the components. As for the next step, the ROV attached to one string and re-positioned it to eventually 37m horizontal distance to the other string. Afterwards, the anchors were rotated so that both module sides of the strings faced each other. The accuracy of the latter was 15° and the orientation was done using the previously defined ROV orientation. Finally, the orientation of the anchor was fixed using the included safety pin.

After connection of the first string to the node, the string was powered up with instruments remaining switched off. Afterwards, the daisy-chain connection was made, i.e. the second string to the first, and all instruments were powered up. As confirmed by the ONC systems crew, all instruments were responsive, power usage was normal and no ground faults have been identified. The STRAW strings were successfully deployed and connected but furthermore have been found to be completely functional.

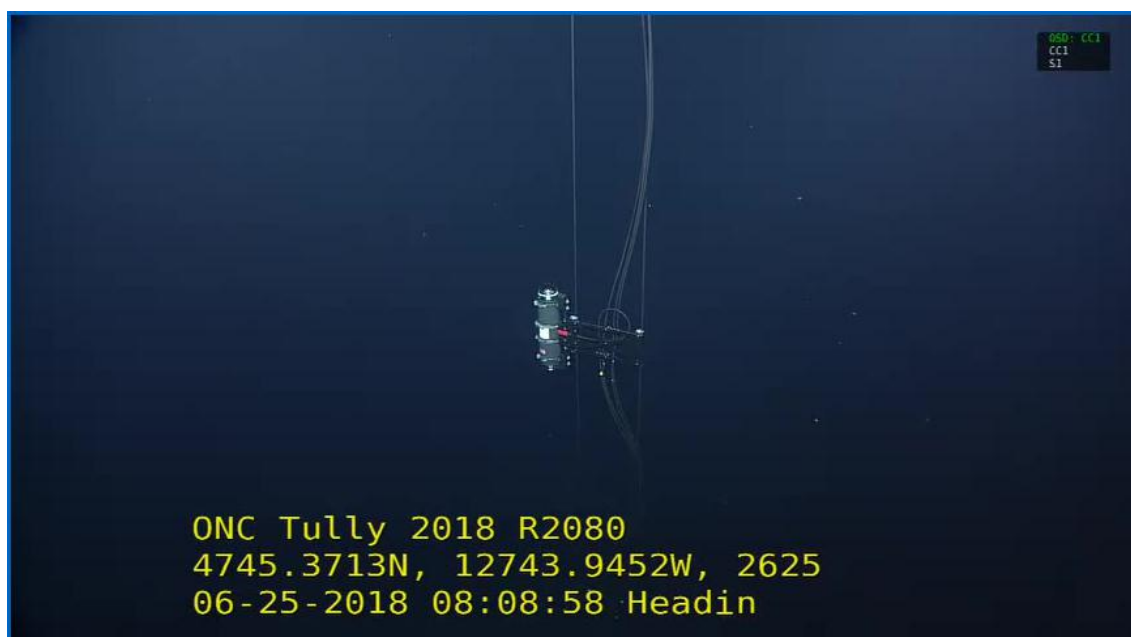


Figure 6.5: ROV view of an sDOM on a successfully deployed STRAW string in 2625m depth. Pictures are a courtesy of ONC and ROPOS, additional ones can be found in appendix A.

6.4 First Light

This chapter has presented an overview of the STRAW detector and its scientific goals together with its subsequent design and the expected performance. The STRAW detector will probe the deep sea of the Cascadia Basin in terms of optical properties in order to assess its feasibility for a future neutrino telescope. In the process, the deep-sea expertise of ONC played a key role in successfully deploying and operating the detector in extreme conditions present in great water depths. The collaboration with marine experts and the guidance of deep-sea applicable materials and structures eventually resulted in a functional STRAW detector deployed in a depth of 2.6km.

Among the last days of this thesis, on the 6th of July 2018, the *first light* of STRAW was carried out after ONC had cleared the mooring for operation. The first flashing operations were successful, verified light detection in all sDOMs and confirmed system integrity of all instruments. Furthermore, as visualized in fig. 6.6, light of the 465nm LED was seen over the full distance of 90m as expected from assumed sea water properties. These preliminary measurements were extracting the Δt histogram of the single-photon channel of the TDC and reveal the expected noise behavior (ref. chapter 5) together with a clear peak of the POCAM flash frequency. This peak was visible for 20, 40, 60 and 90m in the first preliminary runs that were carried out and verifies successful operation of the STRAW detector. The very preliminary analysis programs extracting the data (*strawman.c*) and histogramming it (*histamin.c*) were written by M. Boehmer. More advanced tools for data analysis are currently in the process of being finished and also the simulations are being worked on extensively.

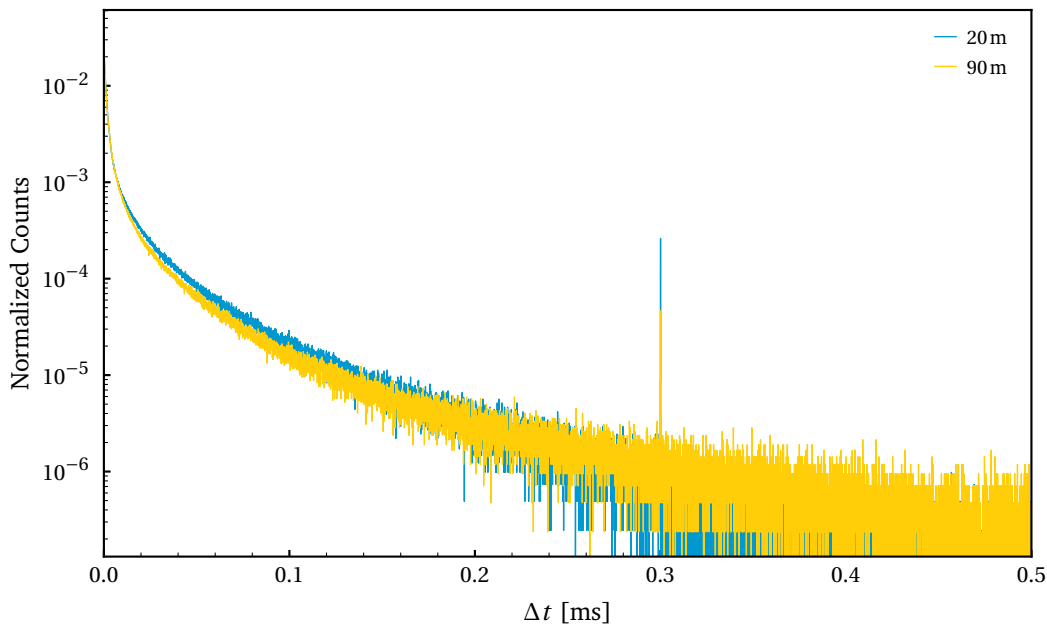


Figure 6.6: STRAW first light. Normalized Δt histogram is extracted from a deployed sDOM TDC while a POCAM 20m (blue) and 90m (yellow) away was flashing the 465nm LED at 3.33kHz. The observed noise matches to the behavior explained in chapter 5 but more importantly, a clear POCAM peak at its flash frequency emerges and verifies light detection at the sDOM.

III

Summary & Conclusions

7

Summary & Conclusions

This work has presented the design, instrumentation, expected performance, construction and eventually deployment of the deep-sea detector project STRAW on a timeline of eight months. Being deployed successfully, the main task of the detector is now the assessment of the Cascadia Basin deep sea for its feasibility to host a new large volumen neutrino telescope.

After a detailed presentation of the instrumentation of STRAW, namely POCAM and sDOM, this thesis has shown that the STRAW detector will enable an optical site characterization between 350 – 600 nm on a distance scale of 20 – 90 m. Estimates on the expected number of photons per sDOM, using a detailed empirical model on the attenuation of sea water, suggests that the instrumentation of STRAW provides feasible grounds for the probing of these scales. Furthermore, the high dynamic range of the sDOM and the adjustable intensity of the POCAM will allow optimization of the light output for all available distances and wavelengths depending on the present conditions. Notably, preliminary runs of the detector already have revealed light detection over 90 m distance at 465 nm and highest POCAM intensity.

The future prospect of STRAW will be the in-depth analysis and ultimately extraction of the optical water properties, most notably absorption and scattering lengths as well as the observation of a possibly seasonal variation of the background radiation. While the preliminary results are promising, further investigation is necessary to provide grounds for the feasibility of the Cascadia Basin site to host a new large scale neutrino telescope. Evenly important is the fact the site offers the unique possibility to work in collaboration with deep-sea experts of ONC and already provides an electrical and optical infrastructure which provided robust and successful for STRAW and could be used also for a neutrino telescope. Equally necessary to the successful development of the STRAW detector was the obtained proof of the deep-sea expertise. Without it, this project would not have been possible.

For the next few weeks and months, the team around the data analysis side of STRAW will investigate and setup the detector control and read-out as well as continue to develop and optimize data analysis tools to extract the optical properties. Then, for the next two years, the STRAW detector will remain in a depth of 2.6 km and continuously take data and as such monitor optical properties and their seasonal behavior. In parallel, the work on simulations will continue which, after determination of the transmission length measurements, will allow assessment of the absorption and scattering properties present in the Cascadia Basin.

Before finishing this thesis, one last remark shall be noted. With the extensive improvements on the POCAM and its calibration, it justified itself as a truly possible calibration device for IceCube-Gen2, the future calibration upgrade of IceCube. The main task to enable this is a further improvement of the isotropy and subsequently lower-order systematic effects which affect the absolute calibration of the photon output. Potential solutions for isotropy improvement are already being discussed and suggest promising. Their investigation and further adaptations to the IceCube standards will be part of the work in the group over the next months and potentially years.

IV

Appendix

A.1 SiPM Response

A common response approximation that describes this behavior can be quickly deduced and is also used for the calibration of the POCAM. The SiPM behavior is governed by the incident light pulse and its stochastic response and can be written in the form of a differential equation

$$dN_{\text{fired}}(t) = \frac{N_{\text{pixel}} - N_{\text{fired}}(t)}{N_{\text{pixel}}} \cdot \text{PDE} \cdot N_{\gamma} \cdot dt \quad (\text{A.1})$$

with the the number of pixels of the SiPM N_{pixel} , the number of fired pixels N_{fired} and the number of incidents photons N_{γ} . This however does not account for noise events that can trigger pixels thermally (*dark counts*) or via a triggered pixel firing a neighboring one (*crosstalk*). However, for an increasing number of pixels firing, the latter become less influential.

Solving this first order inhomogeneous differential equation is done by solving the homogeneous one and then using its solution for the inhomogeneous one. One finds for the homogeneous solution

$$N_{\text{fired}}(t) = C \exp\left(-\frac{N_{\gamma} \cdot \text{PDE}}{N_{\text{pixel}}} t\right) \quad (\text{A.2})$$

and in turn for the inhomogeneous one with the boundary conditions that $N_{\text{fired}}(t=0) = 0$

$$N_{\text{fired}}(t) = N_{\text{pixel}} \left[1 - \exp\left(-\frac{N_{\gamma} \cdot \text{PDE}}{N_{\text{pixel}}} t\right) \right] \quad (\text{A.3})$$

This approximation holds only in the case of the photon pulse being much faster than the pixel recovery time. Then, approximating the photon flux to be constant over its pulse duration

$$N_{\gamma} \approx \frac{\overline{N_{\gamma}}}{\tau_{\text{pulse}}} \cdot t \quad \text{and} \quad t \leq \tau_{\text{pulse}} \quad (\text{A.4})$$

results in the solution of eq. (A.1)

$$N_{\text{fired}} = N_{\text{pixel}} \cdot \left[1 - \exp\left(-\frac{N_{\gamma} \cdot \text{PDE}}{N_{\text{pixel}}}\right) \right] \quad (\text{A.5})$$

which can be inverted

$$N_{\gamma} = -\frac{N_{\text{pixel}}}{\text{PDE}} \cdot \ln\left(1 - \frac{N_{\text{fired}}}{N_{\text{pixel}}}\right) \quad (\text{A.6})$$

and describes the number of incident photons with respect to the fired pixels, i.e. the measured charge output of the SiPM and takes into account saturation effects.

B.1 sDOM in Test Tank

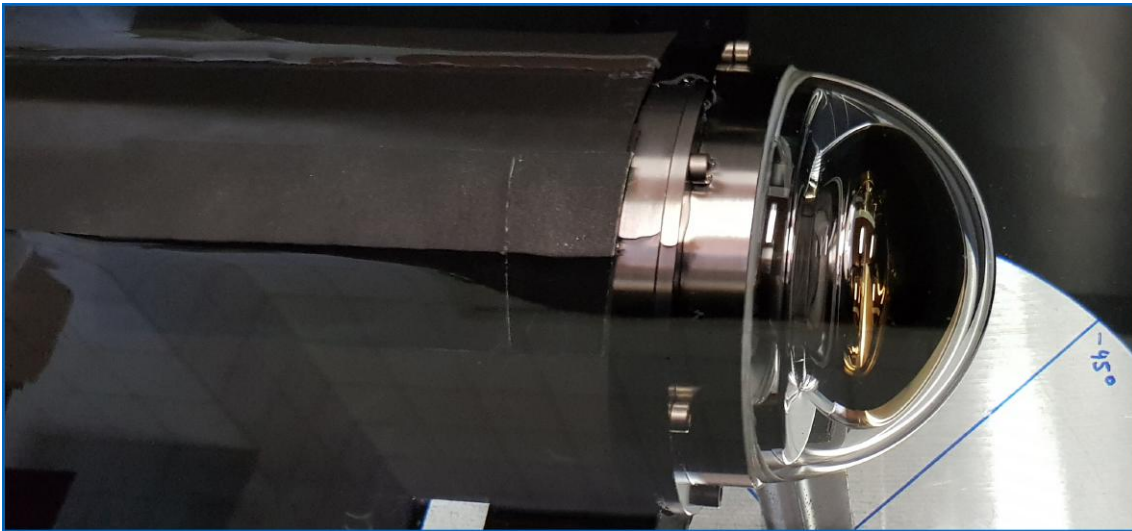


Figure B.1: *sDOM* being submerged in the test tank.

C.2 Deployment

Stills of the STRAW deployment by ONC and on-deck operations.

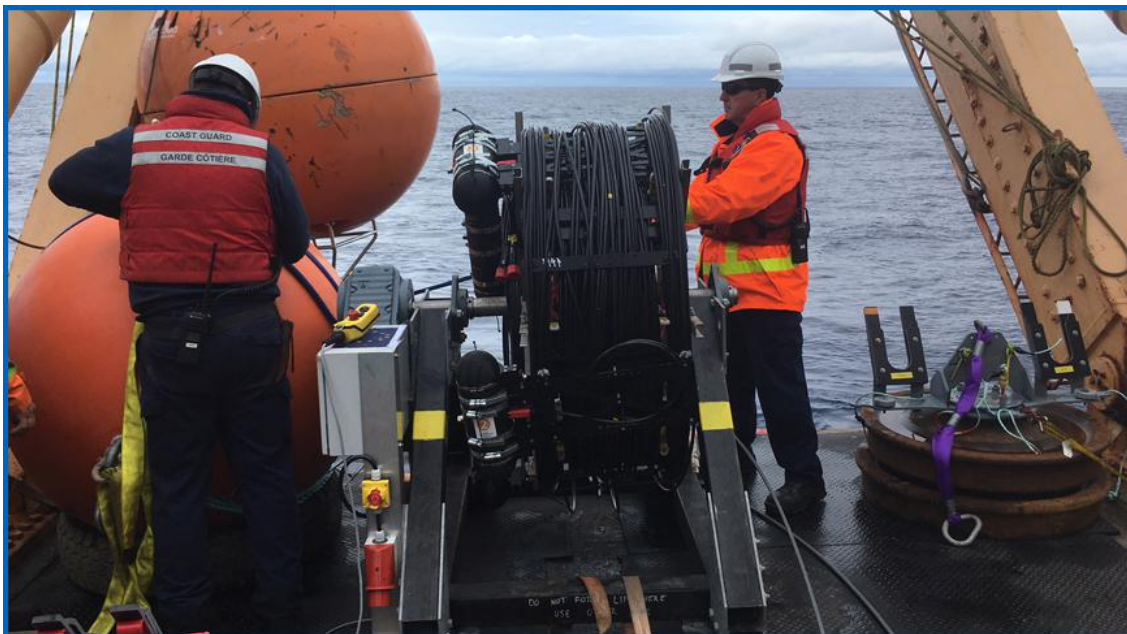


Figure C.2: On-ship unspooling of a STRAW string. Courtesy of P. Macoun, ONC.



Figure C.3: On-ship mJB mounting to a STRAW string. Courtesy of P. Macoun, ONC.

C.3 ROV Inspection

Stills of ROV cameras during inspection, orientation and connection of the STRAW strings. All pictures are a courtesy of ONC as well as ROPOS and are publicly available at <https://dmas.uvic.ca/SeaTube> via the DiveID: *NEPTUNE 2018-06 Tully - R2080*.

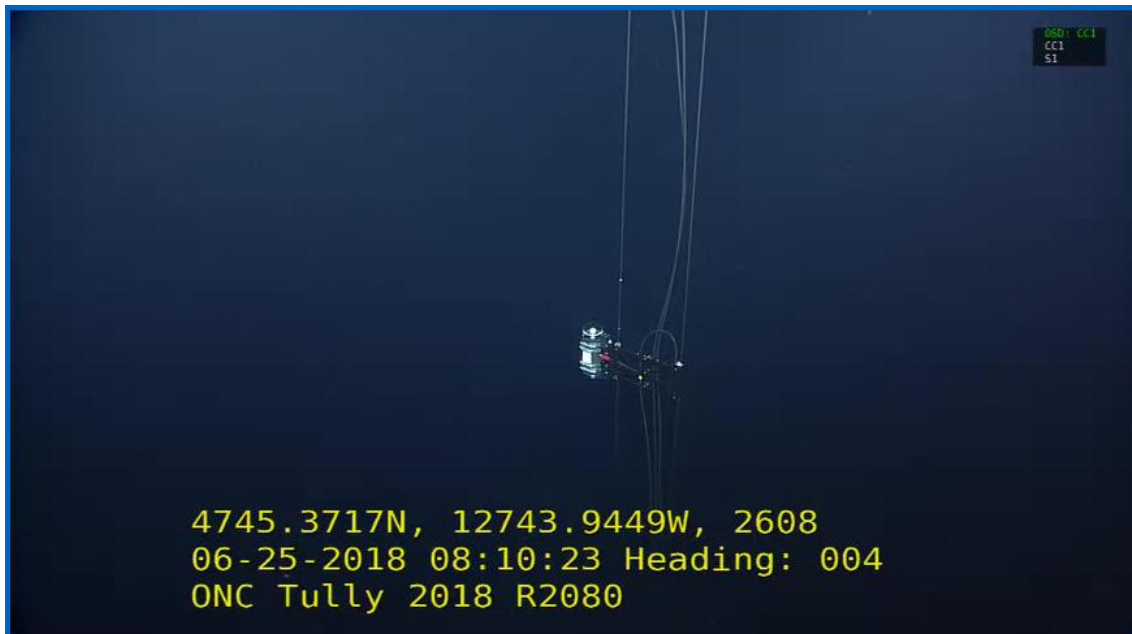


Figure C.4: ROV inspection: POCAM. Depth: 2608m.

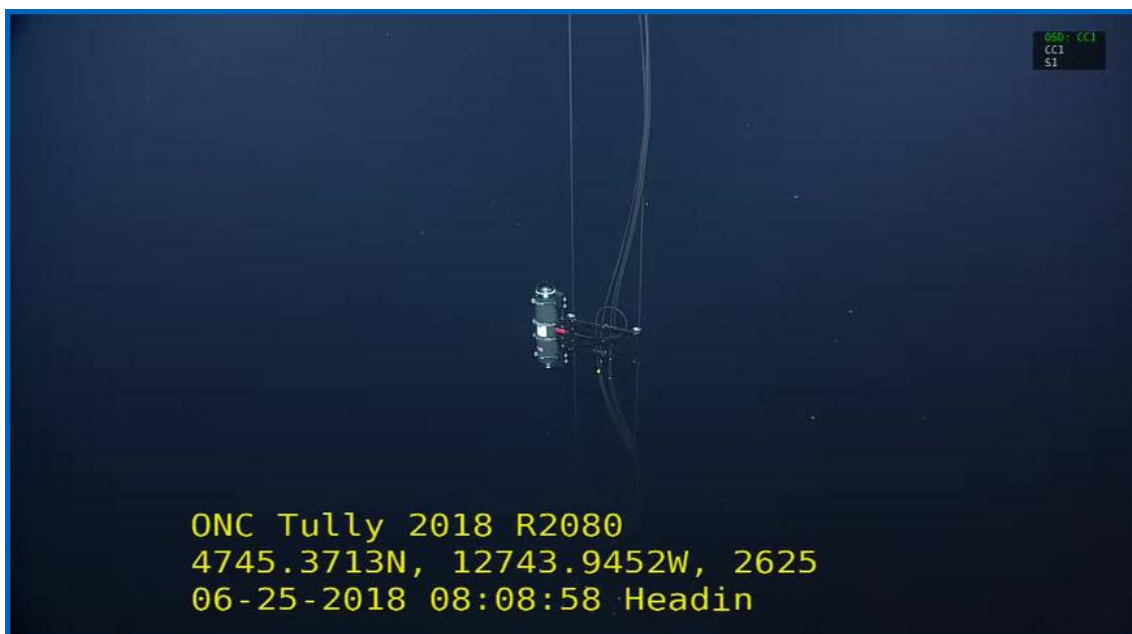


Figure C.5: ROV inspection: sDOM. Depth: 2625m.



Figure C.6: ROV inspection: mini junction box. Depth: 2656m.



Figure C.7: ROV rotating anchor. Depth: 2661m.

1. Aartsen, M. G. *et al.* Development of a General Analysis and Unfolding Scheme and its Application to Measure the Energy Spectrum of Atmospheric Neutrinos with IceCube. *Eur. Phys. J.* **C75**, 116 (2015).
2. Aartsen, M. G. *et al.* First observation of PeV-energy neutrinos with IceCube. *Phys. Rev. Lett.* **111**, 021103 (2013).
3. Aartsen, M. G. *et al.* IceCube-Gen2: A Vision for the Future of Neutrino Astronomy in Antarctica (2014).
4. Aartsen, M. G. *et al.* Letter of Intent: The Precision IceCube Next Generation Upgrade (PINGU) (2014).
5. Aartsen, M. G. *et al.* Measurement of the ν_μ energy spectrum with IceCube-79. *Eur. Phys. J.* **C77**, 692 (2017).
6. Aartsen, M. G. *et al.* Observation of High-Energy Astrophysical Neutrinos in Three Years of IceCube Data. *Phys. Rev. Lett.* **113**, 101101 (2014).
7. Aartsen, M. G. *et al.* The IceCube Neutrino Observatory: Instrumentation and Online Systems. *JINST* **12**, P03012 (2017).
8. Abbasi, R. U. *et al.* A Study of the Composition of Ultra-High-Energy Cosmic Rays Using the High-Resolution Fly's Eye. *The Astrophysical Journal* **622**, 910 (2005).
9. Abbasi, R. *et al.* The energy spectrum of atmospheric neutrinos between 2 and 200 TeV with the AMANDA-II detector. *Astroparticle Physics* **34**, 48–58 (Aug. 2010).
10. Abe, K. *et al.* Solar Neutrino Measurements in Super-Kamiokande-IV. *Phys. Rev.* **D94**, 052010 (2016).
11. Abe, S. *et al.* Precision Measurement of Neutrino Oscillation Parameters with KamLAND. *Phys. Rev. Lett.* **100**, 221803 (2008).
12. Abe, Y. *et al.* Reactor electron antineutrino disappearance in the Double Chooz experiment. *Phys. Rev.* **D86**, 052008 (2012).
13. Ackermann, M. *et al.* Optical properties of deep glacial ice at the South Pole. **111**, D13203 (July 2006).
14. Ackermann, M. *et al.* *The IceCube Neutrino Observatory in Proceedings, 35th International Cosmic Ray Conference (ICRC 2017): Bexco, Busan, Korea, July 12-20, 2017* (2017).
15. Adrian-Martinez, S. *et al.* Letter of intent for KM3NeT 2.0. *J. Phys.* **G43**, 084001 (2016).
16. Ageron, M. *et al.* ANTARES: The first undersea neutrino telescope. *Nuclear Instruments and Methods in Physics Research Section A: Accelerators, Spectrometers, Detectors and Associated Equipment* **656**, 11–38 (2011).
17. Aguilar, J. A. *et al.* Transmission of light in deep sea water at the site of the ANTARES Neutrino Telescope. *Astropart. Phys.* **23**, 131–155 (2005).
18. Ahlers, M. *et al.* GZK Neutrinos after the Fermi-LAT Diffuse Photon Flux Measurement. *Astropart. Phys.* **34**, 106–115 (2010).

19. Ahmad, Q. R. *et al.* Measurement of the rate of $\nu_e + d \rightarrow p + p + e^-$ interactions produced by ^8B solar neutrinos at the Sudbury Neutrino Observatory. *Phys. Rev. Lett.* **87**, 071301 (2001).
20. Aiello, S. *et al.* Characterisation of the Hamamatsu photomultipliers for the KM3NeT Neutrino Telescope. *Journal of Instrumentation* **13**, P05035 (2018).
21. Akhmedov, E. K. *Neutrino physics in Proceedings, Summer School in Particle Physics: Trieste, Italy, June 21-July 9, 1999* (1999), 103–164.
22. Akhmedov, E. K. Parametric resonance of neutrino oscillations and passage of solar and atmospheric neutrinos through the earth. *Nucl. Phys.* **B538**, 25–51 (1999).
23. Aloisio, R. *et al.* Cosmogenic neutrinos and ultra-high energy cosmic ray models. *JCAP* **1510**, 006 (2015).
24. An, F. P. *et al.* Observation of electron-antineutrino disappearance at Daya Bay. *Phys. Rev. Lett.* **108**, 171803 (2012).
25. Anassontzis, E. *et al.* NESTOR: A neutrino particle astrophysics underwater laboratory for the Mediterranean. *Nuclear Physics B - Proceedings Supplements* **35**, 294–300 (1994).
26. Andres, E. *et al.* The AMANDA neutrino telescope: principle of operation and first results. *Astroparticle Physics* **13**, 1–20 (2000).
27. ANTARES Collaboration, T., Adrián-Martínez, S., *et al.* Measurement of the atmospheric ν_μ energy spectrum from 100 GeV to 200 TeV with the ANTARES telescope. **73** (Aug. 2013).
28. Antipin, K. *et al.* The Baikal Neutrino Telescope: Status and plans (Nov. 2007).
29. Antonelli, V., Miramonti, L., Pena Garay, C. & Serenelli, A. Solar Neutrinos. *Adv. High Energy Phys.* **2013**, 351926 (2013).
30. Ashie, Y. *et al.* Evidence for an oscillatory signature in atmospheric neutrino oscillation. *Phys. Rev. Lett.* **93**, 101801 (2004).
31. Askebjerg, P. *et al.* Optical properties of deep ice at the South Pole: Absorption. **36**, 4168–80 (July 1997).
32. Aslanides, E. *et al.* A deep sea telescope for high-energy neutrinos (1999).
33. Avrorin, A. *et al.* Baikal-GVD. **136**, 04007 (Jan. 2017).
34. Aynutdinov, V. The prototype string for the km³-scale Baikal neutrino telescope. *Nucl. Instrum. Meth.* **A602**, 227–234 (2009).
35. Babson, J. *et al.* Cosmic-ray muons in the deep ocean. *Phys. Rev. D* **42**, 3613–3620 (11 Dec. 1990).
36. Bagley, P. *et al.* KM3NeT: Technical Design Report for a Deep-Sea Research Infrastructure in the Mediterranean Sea Incorporating a Very Large Volume Neutrino Telescope (2009).
37. Bahcall, J. N. Gallium solar neutrino experiments: Absorption cross-sections, neutrino spectra, and predicted event rates. *Phys. Rev.* **C56**, 3391–3409 (1997).
38. Bahcall, J. N. *et al.* Standard neutrino spectrum from B-8 decay. *Phys. Rev.* **C54**, 411–422 (1996).
39. Bahcall, J. N. & Ulrich, R. K. Solar models, neutrino experiments, and helioseismology. *Rev. Mod. Phys.* **60**, 297–372 (2 Apr. 1988).

40. Balkanov, V. *et al.* Simultaneous measurements of water optical properties by AC9 transmissometer and ASP-15 Inherent Optical Properties Meter in Lake Baikal. *Nucl. Instrum. Meth. A* **298**, 231–239 (2003).
41. *Beamline* 3rd ed. (Stanford Linear Accelerator Center, 2001).
42. Becerra Esteban, A. *Design of the LED Driver for the Precision Optical Calibration Module* Master's Thesis (Technical University Munich, 2017).
43. Belolaptikov, I. *et al.* The Baikal underwater neutrino telescope: Design, performance, and first results. *Astroparticle Physics* **7**, 263–282 (1997).
44. Berezinskiĭ, V. S. & Zatsepin, G. T. Possible experiments with very high energy cosmic neutrinos: the Dumand project. *Soviet Physics Uspekhi* **20**, 361 (1977).
45. Bugaev, E. V. *et al.* Atmospheric muon flux at sea level, underground and underwater. *Phys. Rev. D* **58**, 054001 (1998).
46. Caldwell, D. O. *Current Aspects of Neutrino Physics* 1st ed. (Springer, 2001).
47. Chmill, V. *et al.* Study of the breakdown voltage of SiPMs. *Nucl. Instrum. Meth. A* **845**, 56–59 (2017).
48. Conrad, J. M. & Shaevitz, M. H. Sterile Neutrinos: An Introduction to Experiments. *Adv. Ser. Direct. High Energy Phys.* **28**, 391–442 (2018).
49. *CSL0701x Series* CSL0701DT5. Rev. 6. ROHM Semiconductor (Nov. 2017).
50. Daum, K. *et al.* Determination of the atmospheric neutrino spectra with the Fréjus detector. *Zeitschrift für Physik C Particles and Fields* **66**, 417–428 (Sept. 1995).
51. Davis, R. Solar Neutrinos. II. Experimental. *Phys. Rev. Lett.* **12**, 303–305 (11 Mar. 1964).
52. De Naurois, M. & Mazin, D. Ground-based detectors in very-high-energy gamma-ray astronomy. *Comptes Rendus Physique* **16**, 610–627 (2015).
53. Dova, M. T. *Ultra-High Energy Cosmic Rays in Proceedings, 7th CERN–Latin-American School of High-Energy Physics (CLASHEP2013): Arequipa, Peru, March 6-19, 2013* (2015), 169–190.
54. Fedynitch, A. *et al.* Calculation of conventional and prompt lepton fluxes at very high energy. *EPJ Web Conf.* **99**, 08001 (2015).
55. *For use over the UV, VIS and NIR spectral regions* Zenith Polymer Diffuse Reflectance Standards, Targets and Materials (2016).
56. Fukuda, S. *et al.* Determination of solar neutrino oscillation parameters using 1496 days of Super-Kamiokande I data. *Phys. Lett. B* **539**, 179–187 (2002).
57. Gagnon, P. *The Standard Model: a beautiful but flawed theory* <https://www.quantumdiaries.org/2014/03/14/the-standard-model-a-beautiful-but-flawed-theory/>. [Online; accessed 19th of March, 2018].
58. Gaisser, T. K., Engel, R. and Resconi, E. *Cosmic Rays and Particle Physics* 2nd ed. (Cambridge University Press, 2016).
59. Gaisser, T. K. Spectrum of cosmic-ray nucleons, kaon production, and the atmospheric muon charge ratio. *Astropart. Phys.* **35**, 801–806 (2012).
60. Gaisser, T. K., Halzen, F. & Stanev, T. Particle astrophysics with high-energy neutrinos. *Phys. Rept.* **258**. [Erratum: *Phys. Rept.* 271,355(1996)], 173–236 (1995).
61. Gialis, D. & Pelletier, G. Cosmic rays and neutrinos from GRBs: Predictions versus acceleration modeling. *Astropart. Phys.* **20**, 323–333 (2003).

62. Giunti, C. & Kim, C. W. *Fundamentals of Neutrino Physics and Astrophysics* (Oxford University Press, UK, 2007).
63. Gonzalez-Garcia, M. C. & Nir, Y. Neutrino masses and mixing: Evidence and implications. *Rev. Mod. Phys.* **75**, 345–402 (2003).
64. *Google Maps* <https://www.google.de/maps>. [Online; accessed 3rd of June, 2018].
65. Greisen, K. End to the Cosmic-Ray Spectrum? *Phys. Rev. Lett.* **16**, 748–750 (17 Apr. 1966).
66. Gruber, L. *et al.* Over saturation behavior of SiPMs at high photon exposure. *Nucl. Instrum. Meth.* **A737**, 11–18 (2014).
67. Guépin, C. *et al.* Ultra-High Energy Cosmic Rays and Neutrinos from Tidal Disruptions by Massive Black Holes (2017).
68. Haddock, S. *et al.* Bioluminescence in the Sea. **2**, 443–93 (Jan. 2010).
69. Haddock, S. *et al.* *The Bioluminescence Web Page* <http://biolum.eemb.ucsb.edu/>. (created 1997; updated 2011) [Online; accessed 30th of June, 2018].
70. Horoi, M. On the MSW neutrino mixing effects in atomic weak interactions and double beta decays (2018).
71. IceCube-Masterclass. *IceCube and Neutrinos* <https://masterclass.icecube.wisc.edu/de/learn-ger/neutrionachweis-mit-icecube>. [Online; accessed 31st of May, 2018].
72. *Integrating Sphere Theory and Applications* tech. rep. (Labsphere, 2017).
73. Janka, H. T. Neutrino Emission from Supernovae (2017).
74. Jurkovič, M. *et al.* A Precision Optical Calibration Module (POCAM) for IceCube-Gen2. *EPJ Web Conf.* **116**, 06001 (2016).
75. Kapustinsky, J. *et al.* A fast timing light pulser for scintillation detectors. *Nuclear Instruments and Methods in Physics Research Section A: Accelerators, Spectrometers, Detectors and Associated Equipment* **241**, 612–613 (1985).
76. Karle, A. IceCube: Construction Status and First Results. *Nucl. Instrum. Meth.* **A604**, S46–S52 (2009).
77. Katz, U. F. & Spiering, C. High-Energy Neutrino Astrophysics: Status and Perspectives. *Prog. Part. Nucl. Phys.* **67**, 651–704 (2012).
78. Klein, J. R. Solar neutrino results from the Sudbury Neutrino Observatory. *Int. J. Mod. Phys.* **A17**. [,470(2001)], 3378–3392 (2002).
79. Kodama, K. *et al.* Observation of tau neutrino interactions. *Phys. Lett.* **B504**, 218–224 (2001).
80. Kotera, K., Choi, W. & Takeshita, T. Describing the response of saturated SiPMs (2015).
81. Kresse, D. *Stellar collapse diversity and the diffuse supernova neutrino background* (work in progress). Master's Thesis (Max Planck Institute for Astrophysics, presumably 2018).
82. Lattanzi, M. Planck 2015 constraints on neutrino physics. *Journal of Physics: Conference Series* **718**, 032008 (2016).
83. Lubsandorzhev, B. K. & Vyatchin, Y. E. Studies of 'Kapustinsky's' light pulser timing characteristics. *JINST* **1**, T06001 (2006).
84. Maki, Z., Nakagawa, M. & Sakata, S. Remarks on the Unified Model of Elementary Particles. *Progress of Theoretical Physics* **28**, 870–880 (Nov. 1962).

85. Margiotta, A. The KM3NeT deep-sea neutrino telescope. *Nucl. Instrum. Meth.* **A766**, 83–87 (2014).
86. Martini, S. & Haddock, S. H. D. Quantification of bioluminescence from the surface to the deep sea demonstrates its predominance as an ecological trait. *Scientific Reports* **7**, 45750 EP - (Apr. 2017).
87. Meyer, H. O. Dark Rate of a Photomultiplier at Cryogenic Temperatures (2008).
88. Migdall, A. L. & Winnewisser, C. Linearity of a Silicon Photodiode at 30 MHz and Its Effect on Heterodyne Measurements. *J Res Natl Inst Stand Technol* **96**, 143–146 (1991).
89. Mondal, S. Physics of Neutrino Oscillation. *ArXiv e-prints* (Nov. 2015).
90. Neiser, A. *et al.* TRB3: a 264 channel high precision TDC platform and its applications. *JINST* **8**, C12043 (2013).
91. *Ocean Networks Canada* <http://www.oceannetworks.ca/>. [Online; accessed 3rd of June, 2018].
92. Otten, E. W. & Weinheimer, C. Neutrino mass limit from tritium beta decay. *Rept. Prog. Phys.* **71**, 086201 (2008).
93. Padovani, P. *et al.* Dissecting the region around IceCube-170922A: the blazar TXS 0506+056 as the first cosmic neutrino source. *Monthly Notices of the Royal Astronomical Society* (2018).
94. Patrignani, C. *et al.* Review of Particle Physics. *Chin. Phys.* **C40**, 100001 (2016).
95. Perl, M. *et al.* Evidence for Anomalous Lepton Production in e^+e^- Annihilation*. **35**, 1489–1492 (Jan. 1975).
96. Peskin, M. E. *Lectures on the Theory of the Weak Interaction in Proceedings, 2016 European School of High-Energy Physics (ESHEP2016): Skeikampen, Norway, June 15-28 2016* (2017), 1–70.
97. *Photomultiplier Tube R12199 TPMH1356E01*. Hamamatsu Photonics K.K. (July 2015).
98. *Photomultiplier Tubes Basics and Applications*. Rev. 3a. Hamamatsu Photonics K.K. (Aug. 2007).
99. Pich, A. *The Standard model of electroweak interactions in 2004 European School of High-Energy Physics, Sant Feliu de Guixols, Spain, 30 May - 12 June 2004* (2005), 1–48.
100. Pontecorvo, B. Mesonium and anti-mesonium. *Sov. Phys. JETP* **6**, 429 (1957).
101. Raby, S. *Grand Unified Theories in 2nd World Summit: Physics Beyond the Standard Model Galapagos, Islands, Ecuador, June 22-25, 2006* (2006).
102. Riccobene, G. & Capone, A. Deep seawater inherent optical properties in the Southern Ionian Sea. *Astropart. Phys.* **27**, 1–9 (2007).
103. Richardson, O. W. *On the Negative Radiation from Hot Platinum in Proceedings of the Cambridge Philosophical Society* **11** (1902), 286–295.
104. Rongen, M. *Measuring the optical properties of IceCube drill holes in European Physical Journal Web of Conferences* **116** (Apr. 2016), 06011.
105. Sapienza, P. *Status of the NEMO Project in Proceedings, 20th European Cosmic Ray Symposium (ECRS 2006): Lisbon, Portugal, September 5-8, 2006* (2006), S5–41.
106. *Schott N-BK7 517642.251*. Schott (Jan. 2014).
107. Smirnov, A. Yu. *The MSW effect and solar neutrinos in Neutrino telescopes. Proceedings, 10th International Workshop, Venice, Italy, March 11-14, 2003*. Vol. 1+2 (2003), 23–43.

108. Smith, R. C. & Baker, K. S. Optical properties of the clearest natural waters (200–800 nm). *Appl. Opt.* **20**, 177–184 (Jan. 1981).
109. *Specifications for blue LED NSPB300B*. Nichia Corporation (Mar. 2012).
110. Spiering, C. *High-Energy Neutrino Astronomy: where do we stand, where do we go?* in (2017).
111. Stanisha, N. *Characterization of Low-dt Non-Poissonian Noise in the IceCube Neutrino Detector* Bachelor's Thesis (Pennsylvania State University, 2014).
112. The IceCube Collaboration. Multimessenger observations of a flaring blazar coincident with high-energy neutrino IceCube-170922A. *Science* **361** (eds Aartsen, M. *et al.*) (2018).
113. The IceCube Collaboration. Neutrino emission from the direction of the blazar TXS 0506+056 prior to the IceCube-170922A alert. *Science* **361** (eds Aartsen, M. *et al.*) 147–151 (2018).
114. The Pierre Auger Collaboration *et al.* Studies of Cosmic Ray Composition and Air Shower Structure with the Pierre Auger Observatory. *ArXiv e-prints* (June 2009).
115. Tipler, P. A. & Llewellyn, R. *Modern Physics* 5th ed. (W. H. Freeman, 2008).
116. Troitsky, S. Unsolved problems in particle physics. *Phys. Usp.* **55**, 72–95 (2012).
117. Unland Elorrieta, M. A. *Studies on dark rates induced by radioactive decays of the multi-PMT digital optical module for future IceCube extensions* Master's Thesis (University of Münster, 2017).
118. Veenkamp, J. *A Precision Optical Calibration Module for IceCube-Gen2* Master's Thesis (Technical University Munich, 2016).
119. *Wacker SilGel 612 A/B* Rev. 1.2. Wacker Chemie AG (Nov. 2014).
120. Watson, A. A. High-energy cosmic rays and the Greisen–Zatsepin–Kuz'min effect. *Rept. Prog. Phys.* **77**, 036901 (2014).
121. *WP710A10LZGCK* Rev. 3B. Kingbright (July 2017).
122. Wu, C. S. & others. Experimental Test of Parity Conservation in Beta Decay. *Phys. Rev.* **105**, 1413–1415 (4 Feb. 1957).
123. *XRL-400-5E* Roithner LaserTechnik GmbH (Sept. 2010).
124. *XSL-365-5E* Roithner LaserTechnik GmbH (July 2010).
125. Yacobi, L., Guetta, D. & Behar, E. Implication of the Non-detection of gzk Neutrinos. *Astrophys. J.* **823**, 89 (2016).
126. Zatsepin, G. T. & Kuzmin, V. A. Upper limit of the spectrum of cosmic rays. *JETP Lett.* **4**, 78–80 (1966).